Numerical Magnetohydrodynamic Investigation of Jets in the Solar Atmosphere

Fionnlagh Iain Mackenzie Dover

Professor Róbert Erdélyi

The University Of Sheffield.

University of Sheffield

School of Mathematics and Statistics

A thesis submitted in partial fulfilment of the requirements for the degree of

Doctor of Philosophy

April 2021

In loving memory of Ewen MacLeod MacKenzie and Colin Alexander Stoddart who both passed away during the course of this PhD. They are very much missed.

Acknowledgements

This thesis would not have been possible without the many amazing people that I have had the good fortune of meeting in my life. I would first like to thank my supervisor Prof. Robertus Erdélyi for his time, guidance and for allowing me to undertake this PhD. I would like to thank Mr Findlay for his excellent maths teaching at Leith Academy, and Prof. James McLaughlin for supervising my B.Sc. thesis at Northumbria University, first igniting my interest in solar physics.

To all my friends in H23 (Farhad, Rahul, Noémi, Rachael, Tamás, Norby and Freddie), I want to thank you for our numerous conversations science and non-science related. I have particularly enjoyed our dungeon and dragons group (Ellie, Drew, Hope, Mihai and Ben), which has kept me sane and entertained during the process of this PhD. My fellow PhD cohort Matt, I could not have asked for a better person to share the whole experience of starting and finishing a PhD with. You have increased my knowledge of solar physics and made me think about many philosophical issues that have changed my worldview. I will miss the interesting conversations only being a desk away.

I am grateful to my parents and brothers (Coinneach, Eoghann and Tim), no words can truly express how important you have all been in my life, and for getting me to this point. I want to thank my partner Lauren for sticking by me throughout my PhD, you have been nothing but caring and supportive and I would not have been able to complete this without you. I know moving from Edinburgh to live in Sheffield has been difficult for you at times, but I have enjoyed living with you in the same place after 4 years of a long distance relationship. I have enjoyed exploring a new location with you and I hope we get to explore many more places together. I love you very much.

Finally, I would like to thank my Grandpa Ewan MacKenzie who passed away 2 weeks before his 90th birthday in December 2018. I remember our many conversations growing up about religion, the origins of the universe, and at what point would a single drop of water cause a dam to burst. I do not doubt that these conversations stoked my interest in science and a desire to try and gain some understanding of the complexities that occur in nature.

Declaration of Authorship

I hereby declare that except where specific reference is made to the work of others, the contents of this dissertation are original and have not been submitted in whole or in part for consideration for any other degree or qualification in this, or any other university. This dissertation is my own work and contains nothing which is the outcome of work done in collaboration with others, except as specified in the text and Acknowledgements. This dissertation contains fewer than 80,000 words including appendices, bibliography, footnotes, tables and equations.

Fionnlagh Iain Mackenzie Dover
April 2021

Abstract

This thesis aims to increase our understanding of solar spicular jets. We carry out a series of numerical studies using MPI-AMRVAC to simulate jets in an idealised stratified solar atmosphere with a vertical uniform magnetic field. The jets are initiated by driving them with a momentum pulse. The relevance of multiple key parameters are investigated by varying the initial driver (amplitude, period, inclination with respect to magnetic field) and magnetic field conditions, to examine the parameter influence over the jet morphology and kinematics. We show the dynamics and morphology of simulated jets are sensitive to the key parameters.

The simulated jets captured key observed spicule characteristics including maximum heights, field-aligned and non-field aligned mass motions/trajectories, and cross-sectional width deformations. The simulations mimic both the observed horizontal and transverse boundary deformation of the jet, which are under-reported in numerical studies. This may be due to the need for a very high spatial resolution to study this phenomenon. With the next generation of solar telescopes around the corner, more research will come to pass on the cross-sectional evolution of small-scale solar jets. Furthermore, the series simulations carried out and presented highlight the presence of not yet observed internal knot substructures generated by shock waves reflected within the jet beam. We show that these fine structures may not yet be observable, but they could be identified with new telescopes such as the Daniel K. Inoyue Solar Telescope (DKIST). If confirmed, these sub-structures will enable a new window through which observers could investigate the physics of spicular jets. This thesis embarks on highlighting the dynamics that may be observable with future facilities.

List of Publications

This Thesis is based on the following publications:

- Mackenzie Dover, F., Sharma, R., Korsós, M. B., Erdélyi, R. (2020); Signatures of Cross-sectional Width Modulation in Solar Spicules due to Field-aligned Flows, *Astrophys. J.*, Volume 905, Issue 1, https://doi.org/10.3847/1538-4357/abc349
- Mackenzie Dover, F., Sharma, R., Erdélyi, R.; Magnetohydrodynamic Simulations of Spicular Jet Propagation Applied to Lower Solar Atmosphere Model, *Astrophys. J.*, Volume 913, Issue 1, https://doi.org/10.3847/1538-4357/abefd1.

The following publication is not included in this Thesis:

- Mumford, S., et al. (2020); SunPy: A Python package for Solar Physics, The Journal of Open Source Software, Volume 5, Issue 46, https://doi.org/10.21105/joss.01832

Contents

List of Figures

List of Symbols

Below is a list of the notation used throughout the text unless stated otherwise:

$\rho \rightarrow$ Density.
$p \rightarrow$ Pressure.
$\boldsymbol{v} = (v_x, v_y, v_z) \rightarrow$ Velocity.
$\boldsymbol{B} = (B_x, B_y, B_z) \rightarrow$ Magnetic field strength.
$\mu_0 \rightarrow$ Magnetic permeability.
$\boldsymbol{g} = (0, 0, -g_z) \rightarrow$ Gravitational acceleration.
$\gamma = 5/3 \rightarrow$ Ratio of specific heat.
$\eta \rightarrow$ Magnetic diffusivity of the plasma.
$\widetilde{\mu} \rightarrow$ Mean atomic weight (the average mass per particle in the units of the proton mass).
$\mathcal{R} \rightarrow$ Gas constant.
$\boldsymbol{j} = (1/\mu_0)(\nabla \times \boldsymbol{B}) \rightarrow$ Current density.
$H(z) = \dfrac{RT(z)}{\widetilde{\mu} g} \rightarrow$ Scale height.
$G \rightarrow$ Gravitational constant.
$M_\odot \rightarrow$ Solar mass.
$R_\odot \rightarrow$ Solar radius.
$p_{mag} = \dfrac{B^2}{2\mu_0} \rightarrow$ Magnetic pressure.
$p_{tot} = p + p_{mag} \rightarrow$ Total pressure.
$m = \rho \boldsymbol{v} \rightarrow$ Momentum density.
$e \rightarrow$ Total energy density.
$C_s^2 = \gamma \dfrac{p}{\rho} \rightarrow$ Sound speed squared.
$V_A^2 = \dfrac{B^2}{\mu_0 \rho} \rightarrow$ Alfvén speed squared.
$\beta = \dfrac{p}{p_{mag}} \rightarrow$ Plasma beta

CHAPTER 1

Introduction

> "And it's not just a heap of salt!! There's fire water! And ice ground! And fields of sand! The outside world must be ten times bigger than inside the wall! Eren! Someday I hope we get to explore the outside world!"
>
> — *Armin Arlert*, Hajime Isayama, Vol. 1 Attack on Titan

1.1 The Sun

The Sun is often referred to as a mundane star by the larger astrophysical community, as it is a common main sequence star (G-type), particularly when it is compared with the zoo of exotic astrophysical objects such as stars in binary systems, neutron stars, red giants, white dwarfs, cepheids, Wolf-Rayet stars, among others. However, one of the most fascinating aspects of the Sun is its magnetic field and our ability to resolve the Sun compared to other astrophysical objects. To quote physicist Robert Leighton, "If the Sun had no magnetic field, it would be as uninteresting as most astronomers think it is". The magnetic field makes the Sun a truly dynamic star as it moulds and shapes its atmosphere environment, for example with coronal loops, prominences, rosettes, fibrils, helmet streamers, etc., as well as storing energy which can be released in dramatic fashion, e.g. through coronal mass ejections, spicules, and EUV jets. Due to high resolution observations we can obtain fantastic images of these dynamics with both ground and space based instruments such as Solar and Heliospheric Observatory (SOHO) (Domingo et al., 1995), Transition Region and Coronal Explorer (TRACE) (Tarbell et al., 1994), Hinode (Tsuneta et al.,

2008; Suematsu et al., 2008; Ichimoto et al., 2008), Solar Dynamic Observatory (SDO) (Lemen et al., 2012), the Interface Region Imaging Spectrograph (IRIS) (De Pontieu et al., 2013), Daniel K. Inouye Solar Telescope (DKIST) (Rast et al., 2020; Rimmele et al., 2020), the Swedish Solar Telescope (SST) (Scharmer et al., 2003a), and the Solar Orbiter (Müller and St. Cyr, 2013). The combination of the Sun's magnetic field and it being the only star we can fully resolve gives us a marvellous space laboratory on our astronomical doorstep, from which the physics of other stars can be understood. An overview of the basic properties of the Sun taken from Priest (2014):

- Age: 4.6×10^9 years.
- Mass: $M_\odot = 1.99 \times 10^{30}$ kg.
- Radius: $R_\odot = 6.96 \times 10^5$ km.
- Surface temperature: 5785 K.
- Mean density: 1.4×10^3 kg m^{-3}.
- Mean distance from Earth: 1 AU $= 1.5 \times 10^8$ km.
- Surface gravity: $g_0 = 274$ m s$^-2$.
- Equatorial Rotation Period: 26 days.
- Composition: 90% H, 10% He, 0.1% other elements.

The Sun has multiple concentric layers as seen in Fig. 1.1, and is powered in its core where nuclear reactions consume hydrogen to form helium. From these reactions, energy is released which ultimately leaves the surface as visible light. The next layer which surrounds the core is the radiative zone, where energy generated by the nuclear fusion in the core moves outwards as electromagnetic radiation. The next significant region is the convective zone, where the method of energy transportation changes from radiative to convective. This occurs because with increased distance from the heat source that is the core, the temperature drops, as described by the second law of thermodynamics. The temperature is eventually sufficiently low for heavier ions (e.g. carbon, nitrogen, oxygen, calcium and iron) to retain a collection of their electrons, which increases the opacity. This makes radiation transport less efficient and consequently traps heat, which in turn creates hot rising gas bubbles which

cools when they reach the surface and begin to drop to the bottom of the convection zone, where they are then reheated, thus repeating the process. The next layer of the Sun is the photosphere, which is the observable surface.

An interesting aspect of stars is that they are all "ringing" as they are a host of multiple standing waves. Just as earthquakes have been studied to probe the interior properties of our planet thereby discovering the Earth has a liquid outer core and solid inner core (Lehmann, 1936), the principle is the same with stars. When ignoring the effect of rotation and magnetism, these starquakes for the Sun have two main restoring forces; buoyancy (gravity) and pressure (Appourchaux et al., 2010).

Those pulsation modes which are dominantly restored by buoyancy are referred to as gravity or g-modes. These g-modes are mostly constrained to the core but propagate through the radiative zone. Hence, studying these waves could theoretically give us crucial information about the structure and dynamics of the deepest parts of the Sun that we are otherwise unable to directly measure. These waves are damped in the convective zone. This makes g-modes very challenging to detect in the Sun. Claims of their observation (García et al., 2007; Fossat et al., 2017; Fossat and Schmider, 2018), have been met with skepticism (Appourchaux et al., 2010; Schunker et al., 2018; Appourchaux and Corbard, 2019; Scherrer and Gough, 2019).

Pulsation modes, where pressure is the restoring force, are known as pressure or p-modes. The p-modes on the Sun was first discovered by Leighton et al. (1962), who found undulations on the Sun with periods near 5 minutes, referred to in many studies as the "5-minute oscillation". The depth at which p-modes penetrate depends on the frequency of the wave, where low frequencies propagate deep into the interior of the Sun and high frequencies are trapped closer to the surface. There are approximately 10^6 resonant p-modes on the Sun, with periods ranging from minutes to hours (Demarque and Guenther, 1999). As they are pressure waves, they freely travel through the convection zone. However, when p-modes are propagating through the solar interior they encounter a temperature gradient and hence a sound speed gradient. The deeper the wave probes, the faster the sound speed is, which means it is refracted back to the surface. The sudden jump in conditions at the solar surface acts as a solid boundary that the wave is unable to escape,

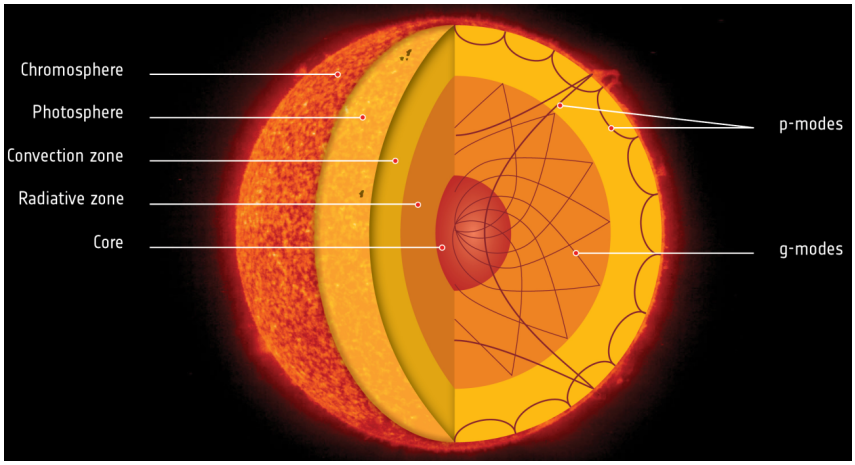

Figure 1.1: Overview of the layers of the Sun. Source: ESA: https://www.esa.int/About_Us/ESAC/Gravity_waves_detected_in_Sun_s_interior_reveal_rapidly_rotating_core.

and it is reflected inwards. However, there are regions (e.g. intergranular lanes) where it is thought p-mode wave leakage occurs, which means they are propagated upwards into the solar atmosphere and are drivers of solar features (Suematsu, 1990; De Pontieu et al., 2004, 2005; Heggland et al., 2007; De Pontieu et al., 2004).

1.2 The Solar Atmosphere

The Sun's atmosphere is truly a complex and fascinating environment. It can be broadly split into three main regions from the top down; the corona, transition region (TR), and chromosphere. Two main factors which separate these regions are their measured temperature (see Fig. 1.2) and plasma beta, the ratio of gas and magnetic pressure (see Fig. 1.4).

1.2.1 Corona

The corona is the Sun's upper atmosphere which continually extends, reaching approximately tens of millions of kilometres into space. It follows the Sun's open magnetic field lines which eventually they feed into the solar wind. It is possible to observe the corona with the naked eye during eclipses, as seen in Fig. 1.3. Otherwise to observe the corona a coronagraph is needed, which is a disk-shaped instrument placed on telescopes that can produce an artificial eclipse by blocking the light from the photosphere. The high temperature of the corona is evidenced by the presence of ions with many electrons removed

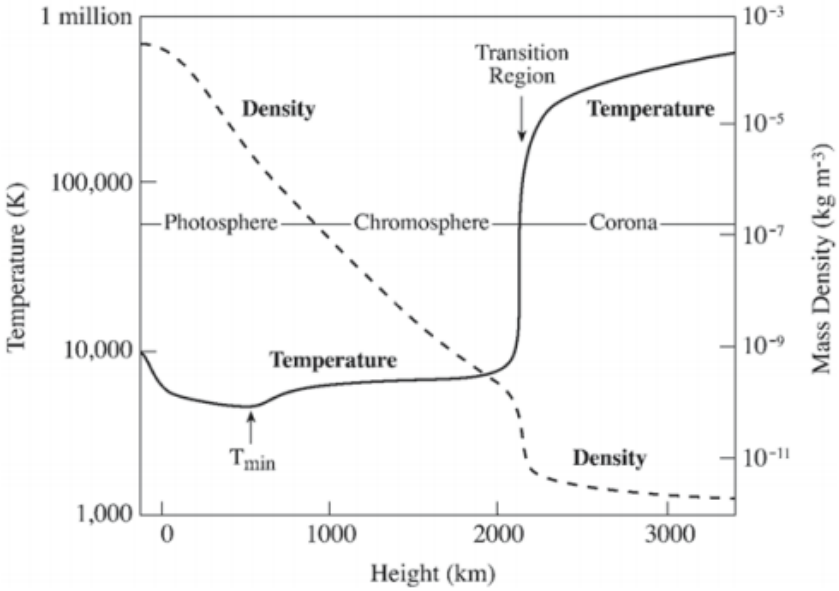

Figure 1.2: A plot of the temperature and density from the photosphere to the corona. Plot taken from Lang (2006).

from the atom. This is evident by atoms such as iron which is $9 - 13$ times ionised in the corona, which indicate temperatures of 1.3 MK and 2.3 MK, respectively (Grotrian, 1939; Edlén, 1943). Despite its high temperature, it has a low amount of heat as it is very rarefied, with densities in the order of 10^{-12} kg m^{-3} (Priest, 2014). This in turn means that the energy density of the corona is much lower than that of the lower layers of the solar atmosphere, such as the photosphere, where the temperature is approximately 5000 K. Despite this, the quiet Sun needs to have a constant energy input of $1.1 - 1.6$ erg cm^{-2} s^{-1} to maintain observed coronal temperatures (Sakurai, 2017).

One startling fact is the extreme coronal temperatures, which are higher than lower regions of the atmosphere (approx. 10^4 K) and photosphere (approx. $5,000$ K). Intuitively, the temperature profile shown in Fig. 1.2 does not make sense, as the temperature is increasing with increased distances from the Sun's heat source (the core), breaking the second law of thermodynamics. This is known as the "coronal heating problem", which was discovered by Grotrian (1939) and Edlén (1943). The coronal heating problem encompasses many open questions, such as: Why is the corona hot?; How does it maintain this heat?; Is the corona heated everywhere, or is heat produced in separate, localised events?; Is it heated in multiple different ways? Many theories have

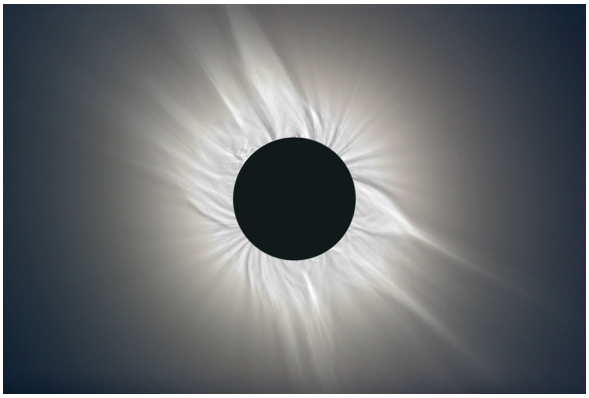

Figure 1.3: Image of the Corona from a total eclipse that occurred on the 29th of March, 2006. Source: https://apod.nasa.gov/apod/ap090726.html.

been put forward that can be reduced down to either wave based; e.g. acoustic shocks and MHD waves (Alfvén, 1947; Uchida and Kaburaki, 1974; Wentzel, 1974; Priest et al., 1998; Hollweg, 1982a; Antolin et al., 2008; Escande et al., 2019), or reconnection; e.g. nanoflares (Parker, 1988; Cargill, 1993; Parnell and Jupp, 2000; Klimchuk and Cargill, 2001; Cargill and Klimchuk, 2004; Antolin et al., 2021). Due to the highly dynamic nature of the atmosphere, in reality both types of heating probably occur (Zirker, 1993; Parnell and De Moortel, 2012).

The heating process can be broken into three main phases: (1) the generation of a carrier of energy (i.e. photospheric driving motions); (2) the transport of energy into the solar atmosphere; (3) the dissipation of this energy in various structures of the atmosphere (Wentzel, 1974; Erdélyi, 2004). For (1-3) there are a plethora of choices, but the main challenge lies in (3). There is agreement in the field that the Sun's magnetic field plays a key role (Parnell and De Moortel, 2012; Arregui, 2015), but the exact physical process that transports the energy from the photosphere upwards and dissipates the magnetic energy into heat, remains elusive. Another key obstacle is resolving (3), as for wave heating the dampening time of the waves is roughly proportional to the magnetic Reynolds number. The magnetic Reynolds number is approximately 10^{14} under solar conditions, as it is dependent on the typical length scales of plasma flow, which are large on the Sun. Therefore, in the solar environment, the challenge is finding mechanisms that generate small length scales (e.g. resonant absorption, phase mixing, plasma inhomogeneities), otherwise, the wave energy will not be converted into heat quickly enough compared to the coronal

cooling timescales (Van Doorsselaere et al., 2020). There is a lack of definitive observation of reconnection/nano-flare heating by a series of small-scale reconnection events (Hudson, 1991; Parnell and De Moortel, 2012). It is possible that small scale solar jets, such as spicules, play an important role in coronal heating due to their ubiquity and dynamic nature, which is discussed later.

1.2.2 Transition region

The transition region (TR) is a thin region of approximately $5,000$ km (Athay, 1981) that sharply links the "cool" chromosphere (10^5 K) to the hot corona (1 MK) at around 2 Mm above the solar surface (Lang, 2006). The TR is dynamically important to the Sun's atmosphere. Due to the sharp change at the TR, waves propagating through the chromosphere can suddenly steepen into shock waves that propagate both upwards into the corona, as well being reflected back into the chromosphere (De Pontieu et al., 2004; Hansteen, 2007; Yuan et al., 2016; Hou et al., 2018). These shock waves can lead to jet-like events (De Pontieu et al., 2004, 2007a; Heggland et al., 2007; Kuźma et al., 2017a), as well as the oscillation of the TR interface itself, e.g. referred to as transition region quakes (TRQ), that may transfer energy to surrounding magnetic structures (Scullion et al., 2011). A key aspect to note is that all energy that heats the corona and drives the solar wind must make its journey through this sudden change in environment (Mariska, 1992).

1.2.3 Chromosphere

The chromosphere spans from above the photosphere up to 2 Mm (Lang, 2006). In ancient times the chromosphere was only faintly seen as a reddy-pink glow around the boundaries of a solar eclipse. This rosy colour originates from the Balmer series of transitions for hydrogen emission (Hα). The atmospheric conditions of the chromosphere are sufficient to cause a quantum transition between the $N = 3$ and 2 energy levels of hydrogen. In the modern age, we can study the chromosphere in great detail thanks to excellent ground and space based telescopes (See Fig. 1.5). The chromosphere is typically observed in the Hα, CaII H, and CaII H and K lines (Ayres, 2019). Observations in these spectral lines shed light on the reason that the chromosphere can be described as the "magnetic complexity zone" (Ayres et al., 2009), due to numerous complex dynamics and structures it hosts as displayed in Fig. 1.5.

Together the TR and chromosphere make up the so-called interface region,

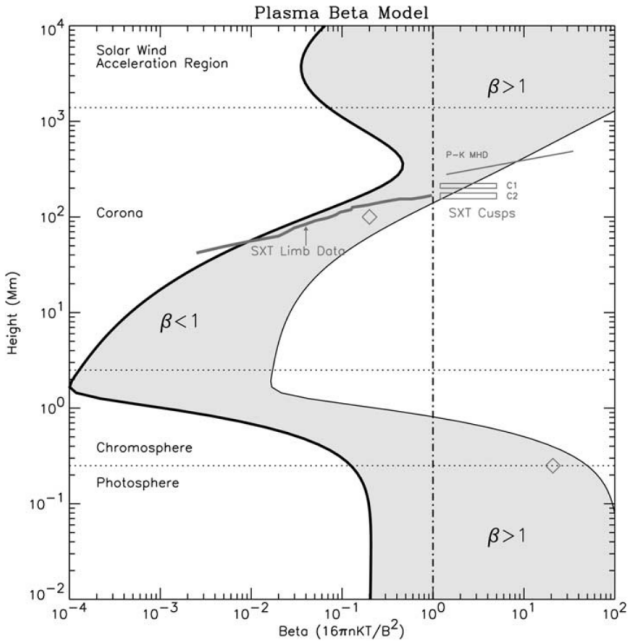

Figure 1.4: A model of the plasma β (ratio between gas and magnetic pressure) over an active region on the Sun, taken from Gary (2001). A high (low) β corresponds to gas (magnetic) pressure being the dominant force. The grey shaded region shows plasma beta at different heights.

which encapsulates an area of complex plasma and magnetic fields, which transports matter and energy between the photosphere and the corona. To understand the dynamics and topography of the magnetic field lines, it is important to establish whether gas or magnetic pressure is dominant. This is represented by plasma beta (β), and its value in the atmosphere is shown by the grey shaded region in Fig. 1.4. In the photosphere where gas pressure is dominant ($\beta > 1$) the magnetic field gets dragged by granular flows, being pinched together as they emanate between granular lanes. At the boundary of supergranular lanes, the magnetic field lines form a larger network and the field lines stem out as magnetic flux tubes (MFT) as shown in Fig. 1.6. These MFT expand further up in the atmosphere due to dropping gas pressure, where magnetic pressure becomes dominant and the field lines become frozen into the plasma (Ayres et al., 2009). An interesting region in the chromosphere is where $\beta = 1$. In this region the sound speed and the Alfvén speed are equal, dividing the solar atmosphere into magnetic and non-magnetic regions (Tsiropoula et al., 2012). This region can lead to the formation of shocks, as it allows for the mode-coupling of purely magnetic waves (Alfvén waves) with magnetoacoustic waves (Hollweg et al., 1982; Rosenthal et al., 2002; Bogdan et al.,

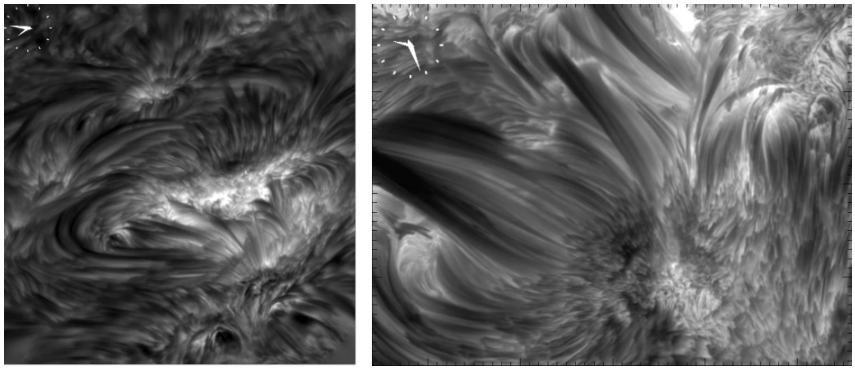

Figure 1.5: Two snapshots are taken from Hα observations using the SST (Swedish Solar Telescope). The panel to the left (right) shows observations of chromosphere above a sunspot in AR998 (chromospheric filaments). These snapshots were taken from the SST movie gallery and can be found here: https://ttt.astro.su.se/isf/gallery/movies/2008/halpha_10Jun2008_AR998_mu043.mov, https://ttt.astro.su.se/isf/gallery/movies/2005/halpha_set1_04Oct2005_region_dt5s.mov

2003; Cally and Goossens, 2008; Wang and Yokoyama, 2020) and has a chaotic topology which forms the canopy observed in Hα lines (see Fig. 1.5 and canopy domain in Fig. 1.6). The magnetic field in the chromosphere is highly twisted and entangled as a consequence of these transitions of the β.

In recent years the correctness of the phrase "coronal heating problem" has been called into question, and even labelled as a "paradoxical misnomer" by Aschwanden et al. (2007). This is because there is no direct evidence of local heating in the corona, and researchers should shift their focus towards solving the "chromospheric heating problem" (Aschwanden et al., 2007). It is not clear how the transport and heating occurs between the interface region and corona. The answer may lie in the multiple jet features such as spicules, mottles, and dynamics fibrils, that are prevalent in the interface region, that energetically advance through the atmosphere (Tsiropoula et al., 2012). In particular, spicules are hypothesised to be a strong candidate for transport mechanisms to heat the atmosphere (Kudoh and Shibata, 1999; De Pontieu et al., 2007b; Kudoh, 2008; Martínez-Sykora et al., 2017; Moore et al., 2011; De Pontieu et al., 2017a; Samanta et al., 2019; Zuo et al., 2019; Bale et al., 2019).

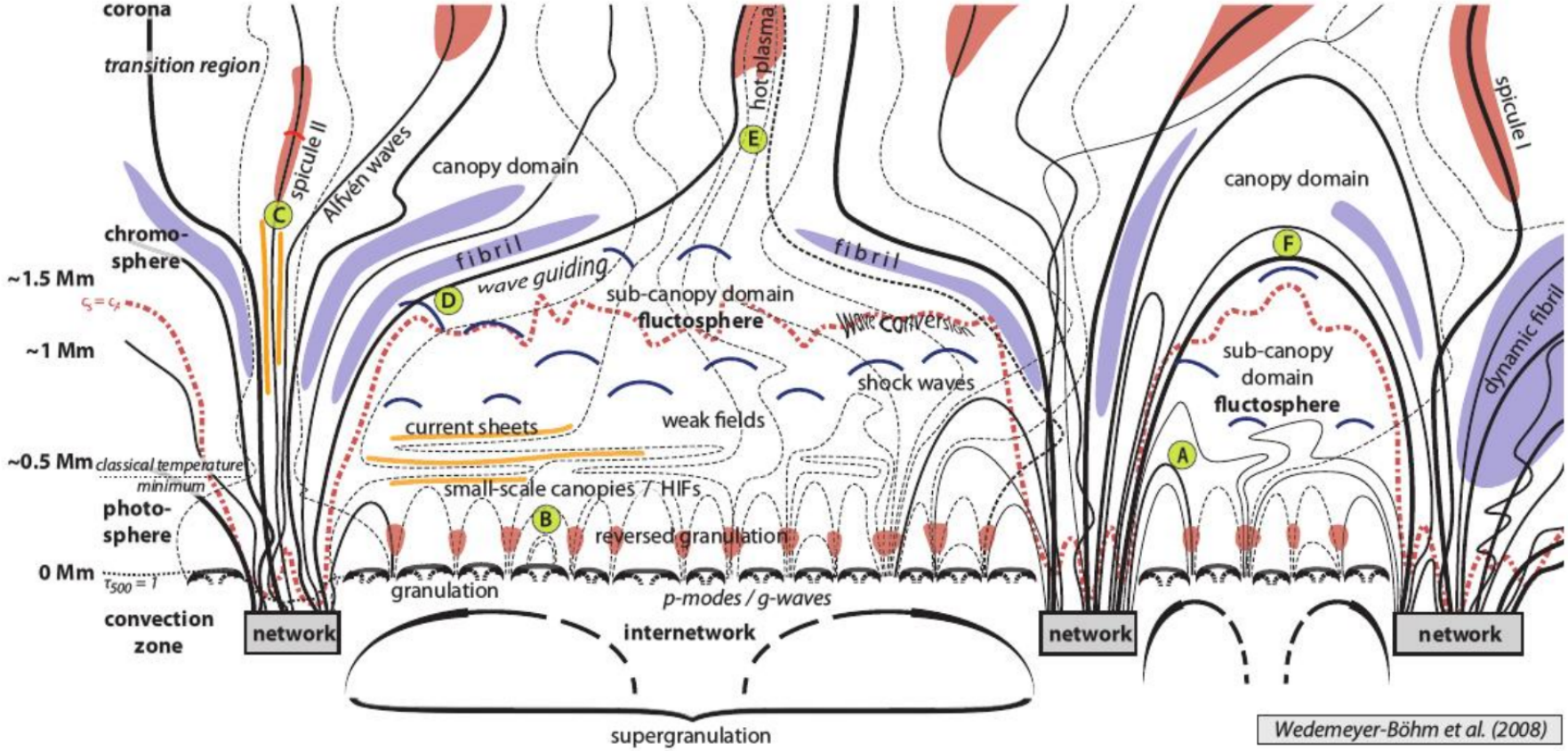

Figure 1.6: Cartoon representation of the complexity of the lower atmosphere taken from Wedemeyer-Böhm et al. (2009). The solid black lines show the magnetic field lines stemming from the intergranular lanes. A and B highlight the small-scale loop features and D-F shows the condition for wave and magnetic canopy interaction.

1.3 Jets in the Solar Atmosphere

The study of jets on the Sun is over 150 years old, starting when Father Angelo Secchi first observed jets in the chromosphere in the 1870s in the Observatory of the Roman Collegium, and described them as "burning fields" (see example in Fig. 1.7). It took nearly 100 years after Secchi's discovery of spicules for researchers to realise the sheer variety of jets that exist in the solar atmosphere (Raouafi et al., 2016). This started with modern observations in the 1970s, with the discovery of coronal transients in Fe XIV, macrospicules and explosive events (Demastus et al., 1973; Bohlin et al., 1975; Withbroe et al., 1976; Brueckner, 1980). This active decade resulted from the launching of the space station Skylab and its capability of carrying out EUV observations. More types of jets were discovered in the 1990s, due to observations with space based Yohkoh soft x-ray telescopes. Shibata et al. (1992) and Strong et al. (1992) discovered solar x-ray jets which are the largest and most energetic of the coronal jets, and new jets have even been discovered recently (Cho et al., 2019).

As a result of many excellent observations, it is clear that solar jets are omnipresent at all times on the Sun regardless of the phase of the solar cycle and there is a vast variety of types of jets, occurring across a whole range of scales. Nowhere is this more true than the chromosphere, which is dominated by spicular jets, which are thin, small-scaled, short lived jet structures, rapidly evolving with time and height. These spicular jets occur everywhere from quiet Sun (QS) (De Pontieu et al., 2007d; Rouppe van der Voort et al., 2007; Pereira et al., 2012, 2014), around active regions (ARs) (De Pontieu et al., 2007d; Pereira et al., 2012; Rouppe van der Voort and de la Cruz Rodríguez, 2013; Gafeira et al., 2017b), and coronal holes (CHs) (Yamauchi et al., 2005; Moreno-Insertis et al., 2008; Pereira et al., 2012; Young, 2015). These transient events could make significant contributions to the coronal heating and solar wind acceleration, which to this day are partially unexplained (Martínez-Sykora et al., 2017; De Pontieu et al., 2017a; Samanta et al., 2019; Zuo et al., 2019; Bale et al., 2019).

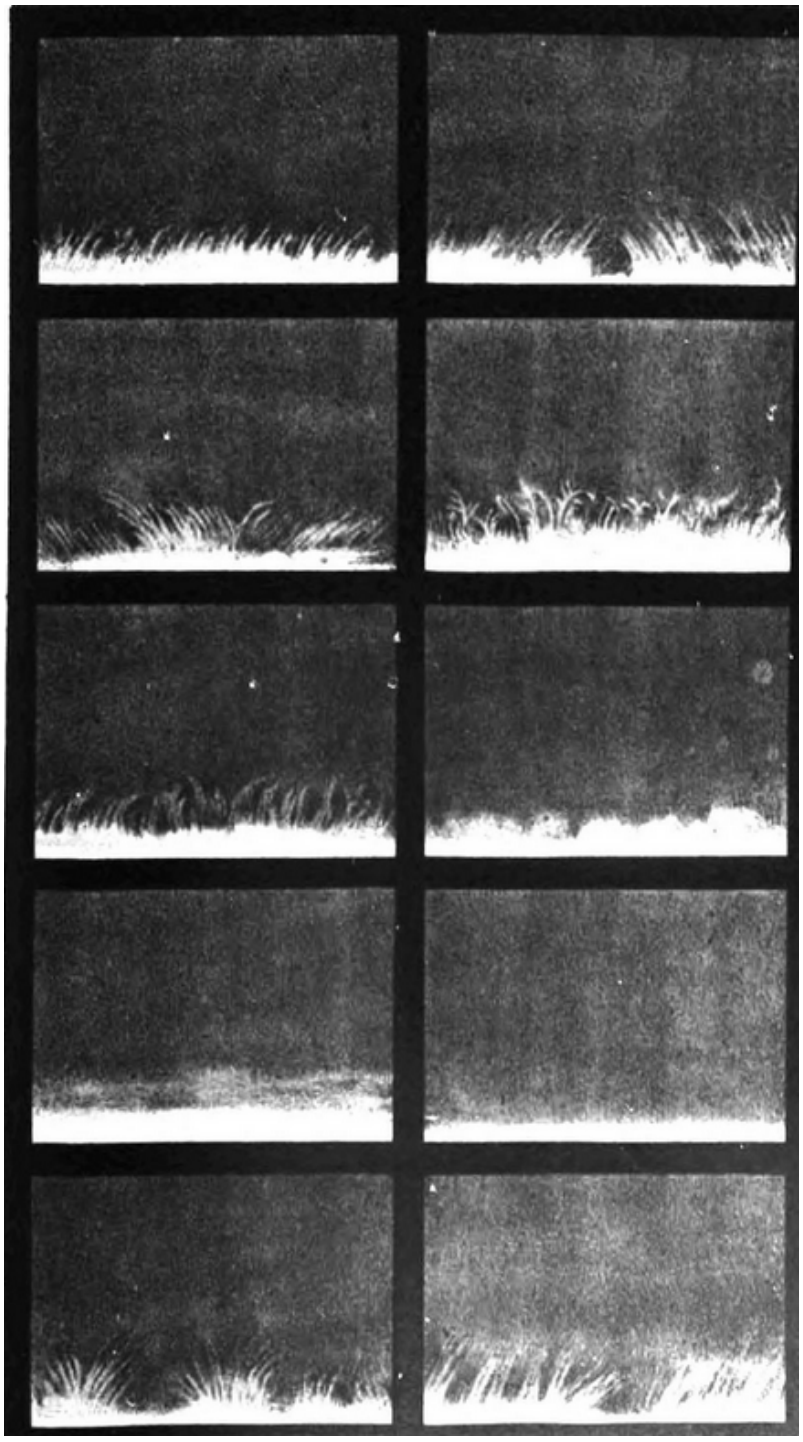

Figure 1.7: Example of early observations of the evolution of spicules taken by Father Angelo Secchi which he describe as flames that are so small they resemble grass in gardens. Images are taken from Secchi (1877).

1.3.1 Spicules

Spicules are thin plasma flows that are omnipresent on the surface of the Sun, and there are approximately 2×10^7 Ca II spicules on the Sun at any time (Judge and Carlsson, 2010). Spicules are best observed in strong chromospheric and transition region (TR) lines such as Hα, Ca II H & K, Mg II H & K, C II and Si IV lines. They were first observed by Secchi (1877) and were named by Roberts (1945), who stated "I was amazed at the extremely brief lifetimes and the great frequency of occurrence which visual observations of these spicules indicated". The lifetime he reported ranged from approximately 2-11 minutes which fits in the range of current estimates for spicules lifetimes. These short lifetimes, along with temporal and spatial (spicules diameters are a few hundred kilometres) resolution limits, historically made observing individual spicules difficult (Sterling, 2000). Also, the dynamic nature of the spicules poses a challenge as they are typically mobbed by other spicules shielding one another, they have bi-directional flows, kinking, twisting, and torsional motions. Other effects such as distortions due to the projection effect and spicule inclination add even more complexity, as these effects can give a misleading picture of spicule dimension and behaviour (Porfir'eva and Yakunina, 2016).

Despite these challenges in observations, there has been much effort as there is a substantial amount of observational data on spicules available, giving us an understanding of their basic properties (mass density, temperature, velocity and magnetic field) (see reviews: Beckers, 1968, 1972), possible driving mechanisms (see review: Sterling, 2000), and the waves and oscillations spicules can host (see review: Zaqarashvili and Erdélyi, 2009). The main interest in spicules lies in the potential to solve outstanding problems in solar physics, such as providing mass and energy into the solar atmosphere and wind, heating the chromosphere/corona, and driving the solar wind (De Pontieu et al., 2011; Moore et al., 2011; Henriques et al., 2016; Samanta et al., 2019). The mass flux taken by the spicule to the corona exceeds that of the solar wind by two orders of magnitude (Thomas and Athay, 1961), so if even 1% of the spicule mass flux escapes the Sun, this would be sufficient to supply the solar wind mass (Pneuman and Kopp, 1977, 1978; Tian et al., 2014; Samanta et al., 2015). Spicules have been estimated to have an energy flux of around 5×10^9 erg cm^{-2} s^{-1}, therefore if even 1% of spicule energy is dissipated in the corona then it could power the upper atmosphere (Zaqarashvili and Erdélyi, 2009). Another important factor, due to the ubiquity of spicules, is that it is

imperative that we can accurately model and describe spicules for us to understand the Sun's chromosphere. The combination of improved spatial and temporal resolution achieved with telescopes, such as Hinode, TRACE, IRIS and SST, over the last two decades, and improved computational models, have led to a "renaissance" in spicule research (Aschwanden, 2019). A major factor in this renewed interest was the rediscovery that the spicules contain two distinct types, labelled as Type I (TI) and Type II (TII) spicules (De Pontieu et al., 2007b). This categorisation is based on their lifetimes, speed, and trajectory, and is not to be confused with the concept of Type I and Type II spicules originally introduced by Beckers (1968), who separates spicules based on significant differences in their line width.

1.3.1.1 Classical/Type I Spicule

To be clear with our terminology of "spicule" we will adopt the definition "classical spicule" as used in Sterling et al. (2010a), Pereira et al. (2013), and Sterling et al. (2020) to refer to limb spicule features observed pre-Hinode i.e. 2006. Classical spicules are observed at the solar limb, typically observed in Hα as thin, finger-like features, that rapidly elongate upwards with an average velocity of around $15 - 40$ km s^{-1} (De Pontieu et al., 2007b) and are grouped together with other spicules, emanating across the boundaries of supergranular cells (see Spicule I stemming from the rightmost network in Fig. 1.6). This group behaviour was first described as "porcupine" and "wheat field" patterns by Lippincott (1957). Properties of classical spicules are outlined by these early reviews Beckers (1968, 1972), where these thin jet-like structures are reported to reach heights of $6.5 - 9.5$ Mm during their 5 minute lifetime, and rise with apparent velocities of 25 km s^{-1}. These values are in agreement with more recent Hα observations of 40 spicules with lifetimes 7.1 ± 2.3 mins, heights of 7.2 ± 2 Mm, and velocities of 27 ± 18.1 km s^{-1}. These spicules are proposed to be initiated by p-mode leakage between granular cells (De Pontieu et al., 2004).

The launching of Hinode/SOT (Solar Optical Telescope) in combination with better ground-based telescopes, such as SST, and improved image processing techniques, was a game-changer as it allowed for the study of jets in unprecedented detail both spatially and temporally (Aschwanden, 2010). De Pontieu et al. (2007b) used observational Ca II H line data collected by Hinode and employed a slit to temporally track the evolution of spicules. They found that, in general, spicules follow a non-ballistic parabolic path or rise up and rapidly

fade out in space-time diagrams. They identified that classical spicules can be split into two distinct populations of spicules based on their velocities, lifetimes, and trajectories. The physical properties of TI spicules are akin to those of classical spicules, as they are defined as long lived (in comparison to TII) structures with lifetimes of $\sim 180 - 420$ s, with bidirectional up flows of mass (which rise from the limb and then fall) following a non-ballistic parabolic path, and have an upward velocity of ranging around $15 - 40$ km s^{-1} (De Pontieu et al., 2007b). These values are in agreement with a more recent study by Pereira et al. (2012) who report average (standard deviations) values of lifetimes as 262 s (80 s), upward velocities of 30 km s^{-1} (9 km s^{-1}), and reach heights of 6.02 Mm (1.21 Mm).

The heights of spicules are typically measured from their footpoints in the photospheric limb, up to the point at which the spicule becomes no longer visible. However, measuring the heights of spicules can be tricky as photospheric roots can be difficult to identify due to their grouping behaviour; it is not obvious whether the footpoints are in front or behind the limb, and the top of the spicule does not have a clearly defined boundary. Other observational factors add to this difficulty, such as exposure time and seeing conditions. Spicules have historically been mostly observed in the Hα line, which is difficult to trace down due to the opacity of the chromosphere. Despite these difficulties, there is general agreement on the reported heights of spicules (Tsiropoula et al., 2012). Using data from Hα observations, Beckers (1968, 1972) estimated the average heights between $6.5 - 9.5$ Mm. Pasachoff et al. (2009) used both Hα observations and TRACE data in the 16,000 Å channel, to obtain heights in the range $4.2 - 12.2$ Mm with a mean of 7.2 ± 2 Mm. Pasachoff et al. (2009) observed heights in TRACE UV and found them to be ~ 2.8 Mm taller than in Hα. De Pontieu et al. (2007b) measure heights in Ca II H using Hinode/SOT which vary from a few hundred km to 10 Mm, with most below 5 Mm. Pereira et al. (2012) report maximum heights of $4 - 8$ Mm using Ca II H data from Hinode/SOT. Numerous studies report that the lifetime of classical spicules is between $120 - 720$ s with an average around 300 s (Roberts, 1945; Rush and Roberts, 1954; Lippincott, 1957; Alissandrakis and Macris, 1971; Cook et al., 1984; Georgakilas et al., 1999). More recently, Pasachoff et al. (2009), who studied the spicules in Hα, found lifetimes between 180 and 720 s with a mean value of 426 ± 138 s. In the past spicules widths ($200 - 1,000$ km) have been very close to the resolution limits of observations and hence most impacted

by observation conditions such as seeing and/or overlapping effects, making it challenging to separate into single spicules (De Pontieu, 2007; Tsiropoula et al., 2012). In addition, spicule widths and heights are impacted by the line which is used for observations. For example, Pasachoff et al. (2009) used Hα data collected with SST and measured widths of $300 - 1,100$ km, with a mean diameter of 660 km, and found that the widths are greater by a factor of 1.5 with ranges of $700 - 2,500$ km when measuring with 1600 Å TRACE. However, this discrepancy in widths could be attributed to TRACE resolution being approximately four times lower than SST. In general, for the classical spicule, widths were measured using Hα and Ca II H and K lines, and spicules are measured as having diameters between 400 and $2,500$ km (Dunn et al., 1960; Beckers, 1968, 1972; Lynch et al., 1973). Modern studies find spicule widths ranging from around $220 - 420$ km with a mean (standard deviation) of 384 km (81 km) Pereira et al. (2012).

An important aspect is that spicules are typically observed to be inclined from the vertical with studies reporting an average inclination of spicules in the range of $19 - 35°$ (Beckers, 1968; Mosher and Pope, 1977; Heristchi and Mouradian, 1992; Pasachoff et al., 2009). Where the most recent of those studies measure an average incline of 23.4° with a range of $0 - 55°$ (Pasachoff et al., 2009). Classical spicules' temperatures range from $5,000 - 15,000$ K and they have densities of approximately 3×10^{-13} g cm^{-3} (Sterling, 2000).

As with the classic spicule, TI spicules are hypothesised to be driven by p-mode leakage between granular cells, that steepen into magnetoacoustic shocks due to decreasing density of the atmosphere as they move upwards through the chromosphere (De Pontieu et al., 2004, 2007b; Martínez-Sykora et al., 2009). Numerical models have predicted that shock-based drivers create non-ballistic trajectories and predict a linear correlation between deceleration of the jet and its maximum velocity (Heggland et al., 2007). Interestingly, this correlation is not only seen in TI spicules (Pereira et al., 2012), but also mottles (Rouppe van der Voort et al., 2007), dynamic fibrils (De Pontieu et al., 2007a), and macrospicules (Loboda and Bogachev, 2019), alluding to the likelihood that all these phenomena are linked to common driving mechanisms.

1.3.1.2 Type II Spicules

The categorisation of spicules into TI and TII was outlined by De Pontieu et al. (2007b), who used slits to construct distance-time diagrams. In these distance-time diagrams, they identified spicules that follow a non-ballistic parabolic trajectory (TI) and spicules that follow a linear trajectory as they rise up in Ca II then fade out (TII). In addition, each type was found to occur over different time scales. The TII spicules are fast, with velocities ranging between $30 - 110$ km s^{-1}, and are short lived, reaching their apexes of > 5 Mm in roughly $50 - 150$ s in contrast to TI spicules. TII spicules form rapidly (~ 10 s), are very thin (≤ 200 km wide) and seem to be rapidly heated to at least TR temperatures, sending material through the chromosphere. Due to their high speeds and rapid formation they were thought to be driven by magnetic reconnection (De Pontieu et al., 2007b). The existence of TII spicules was called into question by Zhang et al. (2012) who revisited the same observational data. Zhang et al. (2012) questioned the use of slits by De Pontieu et al. (2007b), as any spicule that evolves at an angle to the slit will create errors in measurements of spicule heights and lifetimes. Zhang et al. (2012) demonstrated that using filtergram data may be more appropriate as it better captures the 3D motion of spicules, and they found no evidence of TII spicules. However, this was later refuted by Pereira et al. (2012) where again the same data used by De Pontieu et al. (2007b) were revisited, but they use a semi-automated procedure that individually tracks spicule evolution and clearly recaptures the TI and TII spicule populations. There have been numerous reports claiming observations of TII spicules, and the existence of two different spicule types is generally accepted (Rouppe van der Voort et al., 2009, 2015; Shetye et al., 2016; Rutten et al., 2019; Yurchyshyn et al., 2020; Chintzoglou et al., 2021).

Interestingly, Pereira et al. (2012) not only recovered the sub-populations of spicules, but they also found that TII spicules were the most populous. This raises the question, if TII spicules are the most common then why are classical spicules' properties most akin to TI spicules? Pereira et al. (2013) showed that if Hinode data is degraded to have a lower spatio-temporal resolution, the classical spicule properties are regained. They propose that for low spatio-temporal resolution a rapidly disappearing TII spicule may fade out and be replaced by another spicule, resulting in one longer lived structure, therefore introducing an observational bias for longer lifetimes and introducing errors in velocity measurements. This highlights the importance of spatial-temporal

resolution for these small and rapidly evolving structures.

When observing TII spicules in Ca II they appear to rise linearly until their maximum length and then dissipate quickly over their whole length. It has been suggested that TII spicules are being heated out of the Ca II passband (De Pontieu et al., 2007b; Pereira et al., 2012; Skogsrud et al., 2015; Chintzoglou et al., 2018, 2021). Pereira et al. (2014) reported the first spicule observation with IRIS, which added more evidence for the existence of TII spicules. They find that the TII spicules show parabolic space-time diagrams in the IRIS and AIA filters. Although this contradicts their earlier classification of TII spicule i.e. linear spicule (Pereira et al., 2012), there are clearly two spicule types as their defining properties (lifetimes, velocities, and heights) fall into two distinct groups. In multi-thermal studies of TII spicules, heights are reported to have a range of $8 - 20$ Mm with an average of 12.5 Mm (Pereira et al., 2014; Skogsrud et al., 2015). The study of TII spicules is important because they have a larger potential to be able to transfer energy and mass from the photosphere to the interface region and corona. It has been previously thought that spicules could not contribute to coronal heating due to a lack of a coronal counterpart (Withbroe, 1983).

1.3.2 Mottles

Mottles are rapidly changing hair-like short jets observed on disk in the QS regions that are an omnipresent chromospheric structure. They are organised in a complex geometric pattern over the solar disk following the boundaries of the chromospheric network and observed on disk, typically in Hα and Ca II lines. Mottles are typically categorised into two groups (Beckers, 1963):

1. Chains: a small group of mottles that extrude between the boundary of supergranular cells. The mottles are oriented in the same direction and when observed near the limb, they emanate outwards in the same direction, forming what Cragg et al. (1963) called bushes.

2. Rosettes: a larger group of mottles in a circular collection, which is stretching out radially around a common centre, like the stems of a drooping bouquet. They form around the common boundary area of three or more supergranular cells and have a central bright core and are surrounded by both dark and bright mottles (Tsiropoula et al., 2012).

The combination of (1) and (2) form a chromosphere network. The main properties of mottles are that they have heights of roughly $2-10$ Mm and have lifetimes of $2-15$ minutes, which is similar to spicules (Suematsu et al., 1995). They seem to be generated several hundred kilometres above the photosphere and undergo real mass motions of $10-30$ km s^{-1}. Mottles are very dynamic structures that can vary in appearance as they are curved, straight, thin, thick and have transverse motions (De Pontieu et al., 2007a). Most mottles have an ascending and descending phase that follows a parabolic trajectory. The largest Doppler signal appears at the beginning of the ascending phase and the end of the descending phase. The velocity profiles of mottles are symmetrical around zero. The deceleration seen in mottles is too small to be purely the result of solar gravity (i.e. they don't display perfect ballistic flight). Rouppe van der Voort et al. (2007) found that there is a linear correlation between deceleration and maximum velocity of QS dark mottles and this relation has been observed in dynamic fibrils. They propose that these jets are driven with the same mechanism, which is by MHD shock waves, and this viewpoint is further evidenced by numerical simulations (Hansteen et al., 2006; De Pontieu et al., 2007a).

An open question is whether mottles and spicules are the on-disk/limb counterparts to one another (Tsiropoula et al., 1993). There is an observational inconsistency between interpreting spicules and mottles as counterparts. One main issue is that the velocities of spicules (calculated from proper motions) is much greater than those measured in mottles (derived from spectroscopic observations) (Grossmann-Doerth and Schmidt, 1992; Christopoulou et al., 2001). The discrepancy in the velocities is large, with up to an order of magnitude difference (Grossmann-Doerth and von Uexküll, 1973). Spicules and mottles both exhibit different velocity distributions; mottles have symmetrical bi-directional flow whereas spicules' velocity distributions are asymmetric, with the rising phase being most dominant. These differences in the observations can not be attributed merely to the angular distributions of spicules and mottles (Grossmann-Doerth and Schmidt, 1992) and have led researchers to believe that mottles and spicules are separate features (Christopoulou et al., 2001). Christopoulou et al. (2001) propose two possible reasons for this discrepancy, (I) the fact that the values derived from spectroscopic observations represent averages of $1-2''$. Therefore, as the matter moves with greater velocities it is confined to structures below this resolution limit, then the velocity

signal is affected by seeing. (II) For high-velocity spicules, they are near vertical, high altitude structures that occur amidst a sea of mottles that have a low velocity and are highly inclined structures. Therefore, due to the geometrical effect when observing at the limb, spicules will dominate, whereas on disk the mottles would dominate (Grossmann-Doerth and Schmidt, 1992).

When linking spicules and mottles there are two avenues to consider, indirect and direct observational evidence. The indirect evidence that supports this link are: dark mottles (absorbing features in Hα and Ca II lines) and spicules have their optimum visibility at the same wavelength in the wings of Hα (Tsiropoula et al., 1993), follow a parabolic trajectory akin to TI spicules (Rouppe van der Voort et al., 2007) and have similar important physical properties such as lifetime and height. The most convincing observational evidence would be to track a spicule or mottle journey as it crosses the solar limb. This is challenging as when tracing the spicules back on disk, one does not know on what side of the limb the observed feature is located, and it's expected that most spicules will be rooted close to the solar limb so that they would not transform into a clearly identified disk structure (Beckers, 1968). Christopoulou et al. (2001) found multiple examples of individual mottles crossing the solar limb and gives more support to the link between mottles and spicules. In light of the observational evidence both indirect and direct, one can reasonably conclude that spicules and mottles are counterparts to one another.

1.3.3 Dynamic Fibrils

Dynamic fibrils are thin elongated jet-like structures, that typically are seen around AR plages (Hansteen et al., 2006; De Pontieu et al., 2007a). These are on-disk structures, that when observed in Hα line they appear similar to mottles in the QS regions, as they tend to show grouping behaviour akin to rosettes. Foukal (1971b) hypothesised that spicular structures observed in AR and QS environments are similar phenomena. (Foukal, 1971a) evidenced this further by comparing observations of fibrils and classical spicules, where he found similar physical parameters, e.g. length (fibrils tend to be longer), lifetimes, velocities, density and temperatures. One main difference is the magnetic field strength tends to be higher in fibrils. Hansteen et al. (2006) and De Pontieu et al. (2007a) extensively studied dynamics fibrils with sample sizes of 257 each, they both used Hα observations captured by SST; they found average length 1.25 Mm with ranges varying from $0.4 - 5.2$ Mm, with lifetimes

of $120 - 650$ s, average widths of 340 km, and average velocities of 18 km s^{-1} with ranges of $8 - 35$ km s^{-1}. In general dynamic fibrils ascend with a typical velocity of $10 - 30$ km s^{-1} and follow a non-ballistic parabolic path as they rise and fall. This flight path is expected if it is driven with chromospheric shock waves that occur when convective flows and p-modes leak into the chromosphere (Hansteen et al., 2006; De Pontieu et al., 2007a; Langangen et al., 2008b).

Due to more reliable observations of these jet structures, thanks to developments in observational techniques, such as bigger telescopes combined with real-time wavefront corrections by adaptive optics systems, e.g. Scharmer et al. (2003b) and Rimmele (2000), and postprocessing methods, e.g. van Noort et al. (2005) and von der Luehe (1993), it has been possible to study how dynamic fibrils form. Through a combination of observational data from SST and numerical experiments using the Bifrost 3D radiative code, Hansteen et al. (2006) showed that jets in AR are a natural consequence of upwardly propagating slow-mode magneto-acoustic shocks. These shocks are generated by convective flows and p-mode oscillations in the lower photosphere, and leaking upward into the magnetized chromosphere along inclined flux tubes. This viewpoint is also supported in other works (Heggland et al., 2007; De Pontieu et al., 2007a, 2004; Suematsu, 1990), and this driving mechanism for dynamics fibrils is akin to mottles and TI spicules. Given that the physical properties, dynamics, morphology and driver of dynamic fibrils are all similar to mottles and TI spicules, this strongly suggests that these jets are a similar phenomenon, only located in regions of different magnetic activity, and that dynamics fibrils are AR counterparts to QS mottles (Rouppe van der Voort et al., 2007).

1.3.4 RREs/RBEs

Rapid red-shifted and blue-shifted excursions (RRE and RBEs) are short-lived and rapidly moving absorption features in the strong chromospheric Hα and Ca II spectral lines. They appear as sudden shifts in the Doppler estimates at the wing-position of the line of the profile. They are located at the edges of rosettes where there are no dominating shocks compared to the network and internetwork. RBEs were first reported by Langangen et al. (2008a) while searching for on disk counterparts of TII spicules. They reported lengths in the range of $0.5-1.5$ Mm with average 1.2 Mm, and widths in range of $300-600$ km

with average of 500 km. They showed these are short lived features with lifetimes of 45 ± 13 s and velocities in the order of $15 - 20$ km s^{-1}. Rouppe van der Voort et al. (2009) studied RBEs in Ca II and Hα data using the CRISP instrument at SST. They reported similar properties with lengths of approximately 3 Mm, lifetimes of approximately 45 s and Doppler velocities around 20 km s^{-1}. Sekse et al. (2013b,a) investigated RREs in the red wing of the Ca II and Hα lines, finding average length approximately 3 Mm, with widths of approximately 250 km and Doppler velocities of around $15 - 20$ km s^{-1}, which are similar to those found with RBEs. More recently, Kuridze et al. (2015) showed that RREs and RBEs have near-identical lifetimes, widths and lengths. They reported that both have lifetimes have a range of about $20 - 120$ s, with a majority living around 40 s, lengths are in the range of $2 - 9$ Mm with a typical value of around 3 Mm, widths have a range of $200 - 500$ km with the majority around 250 km, and the velocities found were estimated to be in the range of $50 - 150$ km s^{-1}, where the upper limit is super-Alfvénic in the chromosphere.

Finding an on disk counterpart to TII spicules is important as it gives an alternative path to explore to solve outstanding problems presented by these jets. Having a top view of these features means that we will have a view that is not affected by line of sight superposition issues that occur at the limb. These RBEs give an insight into the possible mechanism for jet formation. In Langangen et al. (2008a) the length of RBE is shorter than TII spicules, but this could be caused by an intrinsic difference in the visibility. The magnitude of the mass motion in RBEs is lower than the apparent motion observed in TII spicules. It is thought the driver for TII spicules is magnetic reconnection. If this reconnection is taking place at different heights in the atmosphere, and if the amount of energy is similar for each event, then we would expect the density and velocity of the jet to be dependent on height; i.e. (1) lower heights would give high density jet with low velocity, and (2) higher heights give a low density jet with high velocity. This inverse relationship between density and velocity nicely accounts for the discrepancy between on disk mass motion and the limb apparent motion. For situation (1) this would show enough absorption to be visible on disk, but would be missed on limb observations due to the fibrilar mess at lower heights. For scenario (2) these events on disk would be difficult to observe due to their low opacity, but on the limb, they rise past the mess of the lower chromosphere and can be clearly visible. This means that the difference seen in mass motion could be due to observation biases that are

dependent on the locales of the jet. Langangen et al. (2008a) suggest that Ca II RBEs are linked to Hinode Ca II H spicules observed at limb De Pontieu et al. (2007b). This reasoning is based on the matching physical properties, such as lifetimes, location near network, fading, spatial extent, and the fact that they only show blueshift which corresponds to upward motion. Rouppe van der Voort et al. (2009) add more fuel to the fire by reporting more similarities of lifetimes, locations, temporal evolution, velocities, acceleration, and occurrence rate, between RBEs and TII spicules. In addition, they report that RBEs undergo significant transverse motions (approx. 8 km s^{-1}) during their life, similar to those observed in TII spicules (approx. 12 km s^{-1}) (De Pontieu et al., 2007c). Overall these reported parameters of RBEs agree well with what is observed in TII spicules on the limb.

1.3.4.1 Macrospicules

Macrospicules, as their name suggests, are like a spicule but on a larger scale. As with all spicular features their investigation is important because it is linked to the potential to help resolve the nature of the source of the solar wind generation, and how the corona is heated and maintained. Macrospicules extend further into the solar atmosphere and they are longer lived than classical spicules, but macrospicules are sparsely seen and are typically visible in TR lines e.g. He II 304 Å, N IV 765 Å, and O V 630 Å, formed at temperatures approximately 8×10^4, 1.4×10^5 and 2.5×10^5 K, respectively. Macrospicules have proved a challenge to identify as they are similar to other large jet-like phenomena, due to their properties having a large range. Macrospicules were first defined around 46 years ago when Bohlin et al. (1975) described these features at polar coronal holes using SkyLab's EUV slitless spectrograph. Bohlin et al. (1975) identified 25 macrospicules with lengths of $5.8 - 18.1$ Mm with a lifetime of around $8 - 45$ minutes. They reported that macrospicules were only visible in He II 304 Å, but not in Ne VII465 Å (TR line) or Mg IX 368 Å (coronal line).

Due to the difficulty of identifying macrospicules, older studies tended to be limited to case studies or small groups, such as Kjeldseth Moe et al. (1975), Bohlin et al. (1975), Labonte (1979), Pike and Harrison (1997); Pike and Mason (1998), and Parenti et al. (2002). As the most recent of these studies, Parenti et al. (2002) studied a single macrospicule which extended to 60 Mm, reaching a maximum velocity of $\sim$ 80 km s^{-1}, average falling speed of 26 km s^{-1},

estimated temperature of around 2×10^5 K, and density of 10^{-10} cm^{-3}. While these studies still hold value, they do not give a strong statistical representation of the behaviour of these features. This has been rectified in more recent studies such as Bennett and Erdélyi (2015), Kiss et al. (2017), and Loboda and Bogachev (2019), who all leverage within the range of $2.5 - 5$ years of data collected by SDO/AIA with samples of 101, 301 and 330 macrospicules, respectively. These studies agreed with Wang (1998) that macrospicules are seen in different regions of magnetic environments although they are less numerous, with Loboda and Bogachev (2019) reporting 63.3% found in CH and 36.7% in QS regions. In general they show that macrospicules range in height from $7 - 70$ Mm, in width from $3 - 16$ Mm, and have maximum velocities of $10 - 150$ km s^{-1} and lifetimes $3 - 45$ minutes (Bohlin et al., 1975; Withbroe et al., 1976; Karovska and Habbal, 1994; Parenti et al., 2002; Bennett and Erdélyi, 2015; Kiss et al., 2017; Loboda and Bogachev, 2019).

Their widths and heights put them among the smallest categories of jets observed in the EUV. Their rising velocities and lifetimes make them plausible candidates for being the EUV counterpart of TII spicules. As with many of the jets discussed here, they have been observed to have parabolic paths that are non-ballistic. Curiously, just as was found with mottles and dynamic fibrils, there is a correlation between the initial velocities and decelerations of the jets, which indicates that macrospicules are driven by magnetoacoustic shocks, but unlike mottles and dynamic fibrils ($1 - 2$ minutes for chromospheric jets), the shock would require a longer period of 10 ± 2 minutes (Loboda and Bogachev, 2019). This ultimately suggests that macrospicules have a different set of formation conditions than their chromospheric cousins.

1.3.5 Summary of Spicular Jets

We have collected together the basic properties of spicular jets stated through this sections in Table 1.1. This is to serve as quick reference when comparing the simulated jets with the observational properties.

Table 1.1: Values based on cited papers throughout Section 1.3

Feature	**Obs.**	**Life-time (s)**	**Velocity** (km s^{-1})	**Height (Mm)**	**Possible Driver**
Spicule TI	limb	$180 - 720$	$20 - 40$	$4 - 12$	shock
Spicule TII	limb	$10 - 150$	$50 - 150$	$5 - 20$	reconnection
Dynamic fibrils	disk	$120 - 650$	$10 - 30$	$0.4 - 5.2$	shock
Mottles	disk	$120 - 900$	$10 - 30$	$2 - 10$	shock
Macrospicule	limb	$180 - 2700$	$10 - 150$	$7 - 70$	shock
RREs/RBEs	disk	$20 - 120$	$10 - 50$	$1 - 4.5$	reconnection

1.4 Magnetohydrodynamic Equations

One useful method for modelling plasma flows (i.e. a magnetic fluid) is by using a combination of the Navier–Stokes equations of fluid dynamics with Maxwell's equations of electromagnetism, which are the foundation of the magnetohydrodynamic (MHD) equations. An interesting property of the MHD equations is they are scale-independent, hence they are equally suitable for describing laboratory plasma for example in tokamaks (~ 20 m), and for astrophysical plasmas such as accretion disk of an active galactic nucleus ($\sim 10^{21}$ m) (Goedbloed and Poedts, 2004). MHD theory holds if the typical time (length) scale is greater than the ion gyroperiod (gyroradius) and mean free path time (length), and the plasma velocities are not relativistic (Priest, 2014). The MHD equations shown will be ideal form. This is when we assume that the plasma is perfectly conducting, non-resistive, non-viscous, no radiation and we also utilise the ideal gas law ($p = \rho\mathcal{R}T/\tilde{\mu}$), where p is the gas pressure, ρ is the density, $\mathcal{R} = 8.3 \times 10^3$ J K^{-1} kg^{-1} is the gas constant, and $\tilde{\mu} = 1$ is the mean atomic weight for a neutral plasma.

1.4.1 Continuity Equation

The mass continuity equation that physically represents that matter cannot be created or destroyed is given by,

$$\frac{\partial \rho}{\partial t} = -\boldsymbol{\nabla} \cdot (\rho \boldsymbol{v}), \tag{1.1}$$

where $\boldsymbol{v} = (v_x, v_y, v_z)$ is the plasma velocity and t is time.

1.4.2 Momentum Equation

The momentum equation describes the balance between acceleration and pressure/tension forces, as well as any other forces acting in the system, such as gravity, as shown by,

$$\rho \frac{d\boldsymbol{v}}{dt} = -\nabla p + \frac{1}{\mu_0}(\boldsymbol{\nabla} \times \boldsymbol{B}) \times \boldsymbol{B} + \rho \boldsymbol{g}, \tag{1.2}$$

where $\boldsymbol{B} = (B_x, B_y, B_z)$ is the magnetic field strength, $\mu_0 = 4\pi \times 10^{-7}$ Hm^{-1} is the magnetic permeability of a vacuum, and $\boldsymbol{g} = (0, 0, g_z)$ is the gravitational acceleration. The Lorentz force is a perpendicular force to the magnetic field lines that is a combination of two forces that are created by the magnetic field,

$$\frac{1}{\mu_0}(\boldsymbol{\nabla} \times \boldsymbol{B}) \times \boldsymbol{B} = \frac{1}{\mu_0}(\boldsymbol{B} \cdot \boldsymbol{\nabla})\boldsymbol{B} - \nabla \left(\frac{\boldsymbol{B}^2}{2\mu_0} \right). \tag{1.3}$$

The two forces on the right hand side of Eq. (1.3) are the magnetic tension and magnetic pressure. The magnetic tension acts to straighten out curved magnetic fields lines, and the magnetic pressure acts to push magnetic fields apart.

1.4.3 Energy Equation

The energy equation is given by,

$$\frac{D}{Dt}\left(\frac{p}{\rho^{\gamma}}\right) = 0, \tag{1.4}$$

where $\gamma = 5/3$ is the ratio of specific heats and $D/Dt = \partial/\partial t + \boldsymbol{\nabla}\cdot$ is the material derivative, which gives the rate of change when the frame of reference is moving with the fluid flow.

1.4.4 Induction Equation

The induction equation describes the temporal evolution of the magnetic field, with respect to the advection and dissipation of the magnetic field,

$$\frac{\partial \boldsymbol{B}}{\partial t} = \boldsymbol{\nabla} \times (\boldsymbol{v} \times \boldsymbol{B}) - \frac{1}{\mu_0}\nabla \times (\eta \boldsymbol{\nabla} \times \boldsymbol{B}). \tag{1.5}$$

where $\eta = \mu_0 \sigma_c$ is the magnetic diffusivity and σ_c is the electrical conductivity. The coupled behaviour of the magnetic field and plasma is determined by the ratio of the two terms on the right hand side, defined as the magnetic Renolds number,

$$R_m = \frac{\boldsymbol{\nabla} \times (\boldsymbol{v} \times \boldsymbol{B})}{\eta \nabla \boldsymbol{B}} = \frac{l_0 V_0}{\eta}, \tag{1.6}$$

where l_0 (v_0) are typical length (velocity) scales. For structures on the Sun, the typical length scales tend to be large in comparison to the magnetic diffusivity, which results in a large magnetic Reynolds number. This has important implications on coronal heating, as it impedes the dissipation of waves in the corona. For plasma in the corona and in some parts of the chromosphere, the ideal limit is applicable and we can assume that we have a perfectly conducting plasma ($R_m \to \infty$) which modifies the induction equation to

$$\frac{\partial \boldsymbol{B}}{\partial t} = \boldsymbol{\nabla} \times (\boldsymbol{v} \times \boldsymbol{B}). \tag{1.7}$$

This large R_m has important implications for the motion of the plasma and the magnetic field lines. This is because Alfvén's Frozen Flux Theorem shows

that the magnetic field moves with the plasma (Priest, 2014). The magnetic flux through the surface S bounded by simple connected curve C is given by,

$$\psi = \iint_s \boldsymbol{B} \cdot d\boldsymbol{S}. \tag{1.8}$$

The magnetic flux can change in two ways, it can vary temporally with S held fixed or can change by the advection of the plasma bounded by C. These changes are mathematically represented by,

$$\frac{d\psi}{dt} = \iint \frac{\partial \boldsymbol{B}}{\partial t} \cdot d\boldsymbol{S} + \oint_c \boldsymbol{B} \cdot \boldsymbol{v} \times d\boldsymbol{l}, \tag{1.9}$$

where $d\boldsymbol{l}$ is a line element parallel to curve C. By using Stokes theorem, one obtains

$$\frac{d}{dt} \iint_S \boldsymbol{B} \cdot d\boldsymbol{S} = \iint_S \left(\frac{\partial \boldsymbol{B}}{\partial t} - \boldsymbol{\nabla} \times (\boldsymbol{v} \times \boldsymbol{B}) \right) \cdot d\boldsymbol{S} = 0, \tag{1.10}$$

which is zero due to (1.7). This implies that no matter what the plasma does, it is moving around with the same number of field lines going through the surface which encompass the same number of plasma particles. The magnetic field lines are frozen into the plasma, therefore if the plasma moves the magnetic field lines have to move with it, e.g. if the plasma expands so too will the field lines.

1.4.5 Solenoidal Constraint

The solenoidal constraint implies that there are no magnetic monopoles or sinks of the magnetic field,

$$\nabla \cdot \boldsymbol{B} = 0. \tag{1.11}$$

1.4.6 Overview of MHD Waves

Spicules are thought to be able to act as waveguides in the solar atmosphere, and the dynamics that we encounter later in this thesis may have wave-based origins. To understand the basic wave behaviour of an ideal plasma, we first consider a homogeneous plasma with no gravity, with a uniform vertical magnetic field $\boldsymbol{B} = (0, 0, B_0)$, in pressure equilibrium, with no initial flow. To study the waves in this medium, we first linearise the ideal MHD equations to study small perturbations (subscript 1) from the plasma equilibrium (subscript 0),

$$\boldsymbol{B} = \boldsymbol{B}_0 + \boldsymbol{B}_1(\boldsymbol{r}, t), \quad \boldsymbol{v}_1 = \boldsymbol{v}_1(\boldsymbol{r}, t), \quad \rho = \rho_0 + \rho_1(\boldsymbol{r}, t), \quad p = p_0 + p_1(\boldsymbol{r}, t), \tag{1.12}$$

where $\boldsymbol{r} = (x, y, z)$ is the position vector. Applying these perturbations to the ideal MHD equations and neglecting terms for quadratic order and higher, the perturbations yield,

$$\frac{\partial \rho_1}{\partial t} = \rho_0(\boldsymbol{\nabla} \cdot \boldsymbol{v}_1), \tag{1.13}$$

$$\rho_0 \frac{\partial \boldsymbol{v}_1}{\partial t} = -\nabla p_1 + \frac{1}{\mu_0}(\nabla \times \boldsymbol{B}_1) \times \boldsymbol{B}_0, \tag{1.14}$$

$$\frac{\partial p_1}{\partial t} = c_{s0}^2 \frac{\partial \rho_1}{\partial t}, \tag{1.15}$$

$$\frac{\partial \boldsymbol{B}_1}{\partial t} = \nabla \times (\boldsymbol{v}_1 \times \boldsymbol{B}_0), \tag{1.16}$$

$$\nabla \cdot \boldsymbol{B}_0 = \nabla \cdot \boldsymbol{B}_1 = 0, \tag{1.17}$$

where $c_{s0} = \sqrt{\gamma p_0/\rho_0}$ is the equilibrium sound speed. A general wave equation can be obtained by combining the linearised ideal MHD equations, namely,

$$\frac{\partial^2 \boldsymbol{v}_1}{\partial t^2} = c_{s0}^2 \boldsymbol{\nabla}(\boldsymbol{\nabla} \cdot \boldsymbol{v}) + \frac{1}{\mu\rho_0}(\boldsymbol{\nabla} \times (\boldsymbol{\nabla} \times (\boldsymbol{v} \times \boldsymbol{B_0}))) \times \boldsymbol{B_0}. \tag{1.18}$$

As we are looking for a wave-like solution, we assume a solution will have the form,

$$\boldsymbol{f}(\boldsymbol{r}, t) = \hat{f} e^{i(\boldsymbol{k}\cdot\boldsymbol{r} - \omega t)}, \tag{1.19}$$

where f is a placeholder of any perturbed quantity (in this case $\boldsymbol{v}$), $\hat{f}$ is the amplitude of each perturbation, $\boldsymbol{k} = (k_x, 0, k_z)$ is the wave vector ($k_y = 0$ for simplicity), and ω is the angular frequency. Applying Eq. (1.19) to the wave equation Eq. (1.18), one can obtain a dispersion relation,

$$(\omega^2 - k_z^2 V_{A0}^2)(\omega^4 - \omega^2 k^2 (c_{s0} + V_{A0}) + k^2 k_z^2 c_{s0}^2 V_{A0}^2) = 0, \tag{1.20}$$

where $V_{A0} = B_0/\sqrt{\mu\rho_0}$ is the equilibrium Alfvén speed. This dispersion relation contains solutions for three distinct wave modes. The first solution is obtained from the first term, $\omega = \pm k_z V_{A0}$, which is the forward and backward propagating Alfvén waves. Alfvén waves are purely transverse magnetic waves that propagate along the magnetic field lines. The second and third set of solutions are,

$$\omega^2 = \frac{1}{2} k^2 c_{s0}^2 + V_{A0}^2 \left(1 \pm \sqrt{1 - 4c_T^2 \frac{k_z^2}{k^2}}\right), \tag{1.21}$$

where,

$$c_{T0} = \frac{c_{s0} V_{A0}}{\sqrt{c_{s0}^2 + V_{A0}^2}}, \tag{1.22}$$

is the tube speed. If we do not consider any special cases then each solution for (1.21) gives the forward and backwards fast (taking the + of the last term) and

slow (taking the $-$ of the last term) magnetoacoustic (MA) waves. Hence, these wave modes are a combination of magnetic and sound waves, and therefore the restoring forces are a combination of both pressure and Lorentz force. The mixed properties of these waves illustrate that the wave behaviour is heavily affected by β. If we consider a special case of $\beta \gg 1$, and can hence omit any magnetic terms, i.e. $V_{A0} = 0$, then one obtains the forward and backward propagating sound waves from Eq. (1.21), $\omega = \pm k c_{s0}$. The sound waves are only possible if the fluid is compressible and they are longitudinal waves. If the environment is uniform in temperature then they will propagate isotropically. While these systems of equations give a description of a homogeneous medium, these waves cause different behaviours when confined inside a waveguide.

1.4.7 MHD waves in a Slab

The simulation carried out in this thesis is 2D. Therefore the synthetic spicular structures initiated may host boundary deformations that are akin to those seen in slab models. A slab model has regions of different plasma properties sitting next to each other in a Cartesian geometry. There have been numerous studies on the wave behaviour of slabs (Roberts, 1981; Edwin and Roberts, 1982; Roberts, 1990; Goossens et al., 1992, 2009; Murawski et al., 2015; Allcock and Erdélyi, 2017; Zsámberger and Erdélyi, 2021). We will focus on an early model given by Roberts (1981) and briefly outline the main steps in their derivation. Roberts (1981) introduce a magnetic slab setting in the same state as outlined earlier in this Section 1.4.6, bar a change in the magnetic field configuration,

$$B_0(x) = \begin{cases} B_i, & \text{if } |x| \leq x_0, \\ 0, & \text{if } |x| > x_0, \end{cases} \tag{1.23}$$

where $\pm x_0$ is the location of the boundaries of the magnetic slab and i (e) denote the parameters internal (external) to the magnetic slab. In this setup, by combining Eqs. (1.13) - (1.17) and assuming a plane wave solution ($f(x) = \hat{f} e^{i(kz-\omega t)}$), one can obtain a wave equation of the form,

$$\frac{d^2 \hat{v}_x}{dx^2} - m_{i,e}^2 \hat{v}_x = 0, \tag{1.24}$$

and,

$$m_{i,e}^2 = \frac{(k_z^2 c_{si,se}^2 - \omega^2)(k_z^2 V_{Ai,Ae}^2 - \omega^2)}{(c_{si,se}^2 + V_{Ai,Ae}^2)(k_z^2 c_{Ti,Te}^2 - \omega^2)}. \tag{1.25}$$

The solutions of Eq. (1.24) have a different functional form depending on the sign of $m_{i,e}^2$. Solutions with $m_{i,e}^2 > 0$ are trapped by the waveguide and are

known as trapped modes. Whereas, solutions with $m_{i,e}^2 < 0$ leak some wave energy laterally and these are known as leaky modes. As we are not focusing on searching for solutions for the leaky waves, we discuss the trapped waves, which have a solution of the form,

$$B_0(x) = \begin{cases} C_{10}e^{m_e(x+x_0)}, & \text{if } x < -x_0, \\ C_{00}\cosh(m_i x) + C_{01}\sinh(m_i x), & \text{if } |x| < x_0, \\ C_{11}e^{-m_e(x-x_0)}, & \text{if } x > x_0, \end{cases} \tag{1.26}$$

where C_{jl} for $j = 0, 1$ and $l = 0, 1$ are constants. By applying the boundary conditions at the interface to the system of MHD equations one can arrive at the dispersion relation,

$$D_k(\omega)D_s(\omega) = 0, \tag{1.27}$$

where,

$$D_k(\omega) = \rho_e m_i(\omega_{\rm Ae}^2 - \omega^2)\coth(m_i x_0) + \rho_i m_e(\omega_{\rm Ai}^2 - \omega^2). \tag{1.28}$$

$$D_s(\omega) = \rho_e m_i(\omega_{\rm Ae}^2 - \omega^2)\tanh(m_i x_0) + \rho_i m_e(\omega_{\rm Ai}^2 - \omega^2), \tag{1.29}$$

The solutions for Eq. (1.27) lead to two separate waves modes, known as the kink wave (from $D_k = 0$) and sausage wave (from $D_s = 0$). The trigonometric functions in Eqs. (1.28) and (1.29) are a key component that determines whether the boundaries of the slab move in (kink wave) or out (sausage wave) of phase, as shown in Fig. 1.8.

There are numerous reports of all these MHD waves in the solar atmosphere (Tomczyk et al., 2007; Tomczyk and McIntosh, 2009; Jess et al., 2009; Morton et al., 2012b). By studying these waves one can provide diagnostics of the plasma properties that we otherwise can find challenging to measure directly, such as density (Verwichte et al., 2013), magnetic field strength (Nakariakov and Ofman, 2001), and temperature (De Moortel et al., 2003). This is known as solar magneto-seismology. Of particular interest to this thesis is MHD waves potential to deform the boundary of spicules and that these wave modes have been reported to occur in spicules (Kukhianidze et al., 2006; Okamoto and De Pontieu, 2011; Jess et al., 2012; Verth and Jess, 2016; Sharma et al., 2018).

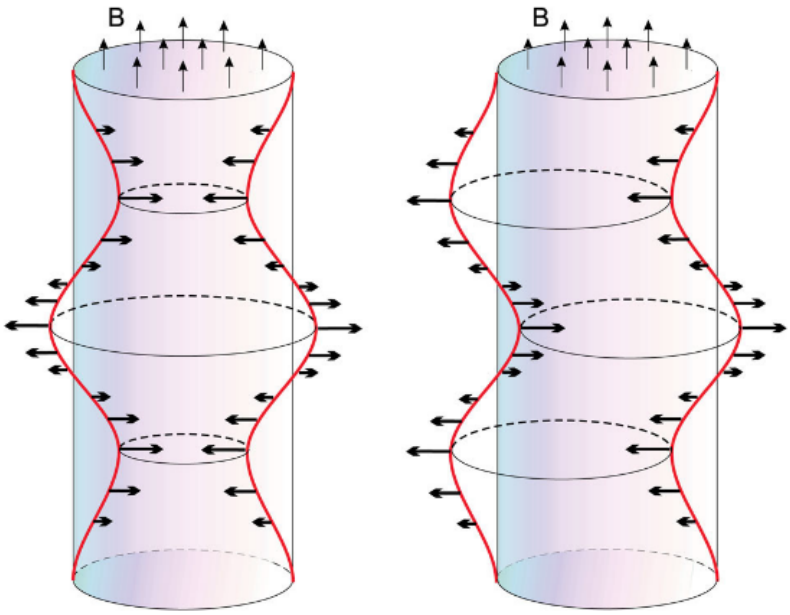

Figure 1.8: Example of the effect of the sausage (left) and kink (right) waves on MFT. This image is extracted from Morton et al. (2012b).

1.5 Outline of Thesis

The thesis aims to investigate the fundamental dynamics of spicular jets by applying simple models. Each chapter will contain the following:

- **Chapter 2**: An overview is given on the current state of numerical models of spicules. We outline the software we use and detail our numerical setup, which is applied throughout the thesis.
- **Chapter 3**: We study synthetic jets in a simplified solar atmosphere. We launch vertical jets with a momentum pulse. By changing multiple parameters linked to the driver (length and initial velocity amplitude) and the magnetic field strength, we investigate how the jet height, cross-sectional width variations, and morphology are impacted by the parameter space.
- **Chapter 4**: In this chapter, we add increasing degrees of tilt from the vertical to see how this impacts the jet dynamics and morphology. A focus parameter space is used to investigate, and an improved jet tracking software is deployed to measure the heights and cross-sectional width variations.

- **Chapter 5**: The cross-sectional width variations identified in Chapter 3 and 4 are studied further by comparison with observations. We postulate the cross-sectional width variations in synthetic jets and observations as standing waves, and apply a wavelet analysis. We also make a comparison of the knots observed in the jet beams of the synthetic jets with blobs reported in observations of larger scale solar jets.
- **Chapter 6**: A summary of the main results and outline the future steps one could take to build upon the research described in the thesis.

CHAPTER 2

Numerical Recipe

2.1 Brief Overview of Numerical Models

How spicules are driven is one of the main issues currently facing solar physicists. The two main avenues of investigation for this phenomenon are observations and numerical simulations. Historically, it has been challenging to spatially/temporally resolve spicular structures and the properties on which to base models have been unclear. This has led to a plethora of numerical models. These models have been reviewed by Sterling (2000) and Aschwanden (2019), and can broadly be split into the following categories: pressure/velocity pulse in lower/upper chromosphere leading to formation of shocks (Shibata et al., 1982; Suematsu et al., 1982; Hollweg, 1982b; Sterling and Mariska, 1990; Heggland et al., 2007; Kuźma et al., 2017a), p-mode leakage (De Pontieu et al., 2004), Alfvén waves which can non-linearly couple and form shocks (Hollweg et al., 1982; Hollweg, 1992; Kudoh and Shibata, 1999; Matsumoto and Shibata, 2010), magnetic reconnection (Yokoyama and Shibata, 1995, 1996; Archontis et al., 2005; De Pontieu et al., 2007b; Isobe et al., 2008; Nishizuka et al., 2008; Sterling et al., 2010b; González-Avilés et al., 2017, 2019, 2018), joule heating due to ion-neutral collisional dampening (Haerendel, 1992; James and Erdélyi, 2002; James et al., 2003; Erdélyi and James, 2004), MHD kink waves (Kukhianidze et al., 2006), and vortical flows which lead to torsional Alfvén waves that drives spicules (Iijima and Yokoyama, 2017; Samanta et al., 2019).

It is important to note that the goal of this thesis is not to determine the origins of spicules. We are mainly focusing on the dynamics and morphology of the jet once it is initiated. For this reason, we decided to establish a method of applying a pulse based, driver and we will give a brief overview of the dynamics of these types of models.

2.1.1 Pulse models

Pulse model simulations start with a form of energy deposition in the photosphere or chromosphere that drives material upwards from these regions into the corona. These types of numerical simulations originated in the 1980s, when Hollweg (1982b) developed the rebound shock model which is triggered with a velocity pulse, Suematsu et al. (1982) placed a pressure pulse in the lower atmosphere, and Shibata et al. (1982) carried out simulations with pressure pulses in the upper chromosphere. Sterling (2000) breaks the velocity pulse into two categories; (i) strong pulse in the lower atmosphere, which covers the photosphere to the low chromosphere, produce initial upward velocities of $\sim$ 60 km s^{-1} for initial velocities; (ii) weak pulse in the lower atmosphere i.e. the rebound shock model, which has upward velocities in the range of $\sim$ 1 km s^{-1}.

Hollweg (1982b) takes a weak pulse of 1 km s^{-1} which is similar to velocities of granular motions at the base of his simulations. Due to the increasing temperature profile of the solar atmosphere, any waves created by disturbing the atmosphere are steepened as they travel upwards. When a wave steepens enough it can form a shock, which lifts the local material. When this lifted material falls back due to gravity, it compresses the lower atmosphere triggering a new wave, which then can propagate upwards and steepen, triggering more rebound shocks. Hollweg (1982b) tried to use this model to explain the formation of spicules as the opposing forces exerted by rebound shocks and gravity, cause the TR to undulate, which he interprets as spicules. Hollweg (1982b) shows this model meets some of the characteristics of spicules as the motion of TR could appear as non-ballistic, with comparable mean upward velocities, heights, temperature, and density. Numerous models have built upon the rebound shock model, by including radiation and heat conduction (Sterling and Hollweg, 1988; Sterling and Mariska, 1990; Cheng, 1992a,b,c). With the inclusion of more sophisticated physics it becomes challenging to reproduce spicule characteristics. For example, when Sterling and Mariska (1990) added realistic radiation losses, they were not able to obtain spicule heights greater than 6 Mm. Cheng (1992a,c) used both radiation losses and ionization. He found the only way of generating jets with properties similar to spicules was by having a longer driving time. Recent simulations carried out by Heggland et al. (2007) used longer driving times. They showed how to generate chromospheric jets in which radiation losses and ionization could be considered,

by placing a monochromatic piston driver at the base of the simulation with velocities (driving times) in the range of $0.2 - 1.1$ km s^{-1} ($180 - 360$ s).

Suematsu et al. (1982) carried out a 1D HD numerical experiment using a strong pulse low in a stratified solar atmosphere. These pulses were initiated by enhancing the pressure ($p/p_0 = 1.1 - 5.0$, where p_0 is local atmospheric pressure) near the base of the simulation in the region of the photosphere to the low chromosphere ($0.00 - 0.75$ Mm), with driving times of 5 mins. These parameters were chosen based on observations of bright points in the chromosphere which are thought to be linked to the presence of spicules (Suematsu et al., 1995; Jess et al., 2012; Oxley et al., 2020). The pressure enhancement leads to the formation of waves that steepen as they travel upwards. When a wave reaches the steep temperature gradient of the TR it produces strong bi-directional shock waves that lift the TR region. The material behind the perturbed TR is interpreted as a spicule. In this model, rebound shock will occur, but the main difference is that, it is the initial pressure pulse itself, not the rebound shock, that lifts the TR. This model can capture parts of the spicule properties, and results in cool spicules (approx. 10^4 k) with a density of 10^{-13} g cm^{-3}, and reaching heights of $3.7 - 14$ Mm. Although the average rise velocity of the spicule of 30 km/s is in the range of observed spicule speeds, in order to reach the upper end of possible spicule heights, the initial velocity of the top of the spicules must be in the range of 50 - 80 km/s, which is the higher limit of observed spicule velocities. These models were further investigated by Shibata and Suematsu (1982) and Shibata et al. (1982), who both studied a wider range of pulse strengths ($1.5 \leq p/p_0 \leq 30$), a wider variety of pulse heights ($0.18 - 1.92$), placing the TR at different heights TR. In both studies, they find that if the length between the pressure pulse and TR is reduced then this results in shorter spicules. This is because the waves have less distance to traverse, therefore less atmosphere to steepen in, which causes the shocks to be weaker.

Another location pressure pulse is placed in the upper chromosphere to simulate spicules. The justification for pressure enhancement at these locations can be created as a consequence of magnetic reconnection. An early example of these models was carried out by Shibata et al. (1982). These were 1D HD simulations used to investigate the properties of surges, excluding radiation and heat conduction. As stated previously, Shibata et al. (1982) took a large

range of pulse heights and strengths. They found that depending on the height which the pulse is located, two different types of jet formation can result, referred to as shock tube jet (above middle chromosphere) and crest shock jet (below middle chromosphere). The shock tube jet is when the pulse itself is responsible for lifting the TR, whereas in the crest shock, the TR is lifted due to a slow shock wave created by the pressure pulse. Compared to the other pulse models there seems to be renewed interest in pressure/velocity pulses just below the TR (Murawski and Zaqarashvili, 2010; Smirnova et al., 2016; Kuźma et al., 2017b,a; Singh et al., 2019). These models include more realistic physics for simulating spicules, such as the inclusion of a magnetic field, radiation losses, thermal conduction, and multi-fluid. They are also able to obtain results in the ranges of spicules height, speeds, temperatures, densities, and trajectories. The resurgence in the upper pulse model may be linked to strong interest in magnetic reconnection as a proposed driver for solar jets, including spicules (Yokoyama and Shibata, 1995, 1996; De Pontieu et al., 2007b; González-Avilés et al., 2017, 2018).

Using pressures, velocity or momentum pulses result in a jet being produced. Both pressure and velocity are linked through the equation of motion, if you drive with a velocity pulse you change the pressure and if you drive with a pressure pulse it would produce velocity. It is difficult to make a direct comparison between different studies as to my knowledge there has been no dedicated study to determine the different effects of using different pulses to drive a jet. To set up a comparable simulation you would need to ensure that each pulse is equivalent, by making sure both contain the same amount of energy. In terms of the system of MHD equations, pressure is scalar and velocity is a vector, so by using a velocity/momentum pulse the degrees of freedom in your system would be reduced. If a common approach is taken for a pressure pulse a uniform ball of pressure is placed just below the TR, then this would expand out isometrically and how much this pulse deviates from isotropic expansion depends on the magnetic field strength. In the case where the driver is a velocity/momentum pulse, then the direction has already been pre-determined. The most important aspect of driving with any type of pulse is the initial location of the pulse with respect to the TR. As highlighted earlier if the pulse is placed lower in the atmosphere it affects what causes the rise of the TR whether it's the rebound shock or the pulse itself when it comes into contact with TR and what heights the TR reaches. The driver used in

this thesis is different as a momentum pulse is used. This causes a significant transport of mass through the simulation. This means that the jets are interpreted as dense column of material kicked up from near the photosphere rather than the lifting of TR region as done in velocity/pressure pulse studies. For my simulations if I was to drive with a pressure pulse at the heights I have driven for the momentum pulse then the results would be similar as displayed in Suematsu et al. (1982). There wouldn't be a significant transfer of mass, the TR region would be lifted by the rebound shock rather than dense jet coming into contact with the TR. Depending on what speeds are produced by the pressure, it may or may not produce knots. When it comes to studying the inclined jets, producing a pressure pulse with a preferred direction would require a particular setup of a pressure gradient which would be more complex than using a combination of v_x and v_y to determine direction. The goal of this thesis is to numerically investigate jets that are a transfer of mass, not just the lifting of the TR.

2.2 MPI-AMRVAC

All the simulations carried out in this thesis use the open source software Message Passing Interface Adaptive Mesh Refinement Versatile Advection Code (MPI-AMRVAC). This software is developed in Fortran 90 parallelized with Message Passing Interface (MPI) (Tóth, 1996; Keppens et al., 2012; Porth et al., 2014; Xia et al., 2017). The main focus of this software is maintaining conservation laws in shock dominated problems. This is achieved using shock capturing schemes to retain near-conservation for a set of hyperbolic partial differential equations, typical in conservative form,

$$\frac{\partial \boldsymbol{U}}{\partial t} + \nabla \cdot \boldsymbol{F}(\boldsymbol{U}) = \boldsymbol{S}_{phys}(\boldsymbol{U}, \partial_i \boldsymbol{U}, \partial_i \partial_j \boldsymbol{U}, \boldsymbol{x}, t), \tag{2.1}$$

where U is the set of conserved variables, $F(U)$ the corresponding fluxes, and S_{phys} are the source terms. The source terms are used to add extra physics, such as gravity, diffusion, and viscosity. In our case, the governing MHD equations are solved in their conservative form (including gravity as an additional source term),

$$\partial_t \rho + \boldsymbol{\nabla} \cdot (\boldsymbol{v}\rho) = 0, \tag{2.2}$$

$$\partial_t (\rho \boldsymbol{v}) + \boldsymbol{\nabla} \cdot (\boldsymbol{v}\rho\boldsymbol{v} - \boldsymbol{B}\boldsymbol{B}) + \boldsymbol{\nabla} p_{tot} = \rho \boldsymbol{g}, \tag{2.3}$$

$$\partial_t e + \boldsymbol{\nabla} \cdot (\boldsymbol{v}e - \boldsymbol{B}\boldsymbol{B} \cdot \boldsymbol{v} + \boldsymbol{v} p_{tot}) = \rho \boldsymbol{g} \cdot \boldsymbol{v}, \tag{2.4}$$

$$\partial_t \boldsymbol{B} + \boldsymbol{\nabla} \cdot (\boldsymbol{v}\boldsymbol{B} - \boldsymbol{B}\boldsymbol{v}) = 0. \tag{2.5}$$

Above is the full system of MHD equations employed in our model, with variables denoted as: time (t), mass density (ρ), plasma velocity $\boldsymbol{v}$, magnetic field ($\boldsymbol{B}$). The total pressure (p_{tot}) and energy density (e) terms are given as,

$$p_{tot} = p + \frac{\boldsymbol{B}^2}{2}, \tag{2.6}$$

$$e = \frac{p}{\gamma - 1} + \frac{\rho \boldsymbol{v}^2 + \boldsymbol{B}^2}{2}, \tag{2.7}$$

where $\gamma = 5/3$ denotes the ratio of specific heats. Solar gravitational acceleration is given by,

$$\boldsymbol{g} = -\frac{GM_\odot}{r^2}\hat{r}, \tag{2.8}$$

where G is the gravitational constant and $M_\odot$ denotes the solar mass.

MPI-AMRVAC has been constructed to be a versatile piece of software, arming the user with a multitude of options. This reduces development time as rather than writing bespoke software for each simulation, modules of the code can efficiently be swapped or modified to produce the desired effect, e.g. changing physic modules, spatial/temporal solvers, grid setup and geometry, changing boundary conditions, and writing one's own custom routines.

2.2.1 Adaptive Mesh Refinement

One of the main features of MPI-AMRVAC is the adaptive mesh refinement (AMR). Using AMR means that rather than having a static fixed resolution for the entirety of the simulation, we have a dynamical grid that adds/removes grid cells as needed. For example, see the differing mesh in Fig. 2.1 from the test case of a hydrodynamic Rayleigh-Taylor Instability (RTI) (see Section 4.3.3 for more description of RTI). In this simulation, there is a denser fluid flowing downwards, and areas of highest resolution are located where rapid changes are occurring in the computational domain. In Fig. 2.2, we can see different levels of AMR being used. For example, cell (3,1) is the level one grid, which is the coarsest resolution initially defined by the user, cells (6,3) and (12,7) are level two and three respectively, with each cell half the size of the previous level. The rules that AMR are allocated and deallocated are:

- The AMR can only be one level higher than its neighbouring cells.

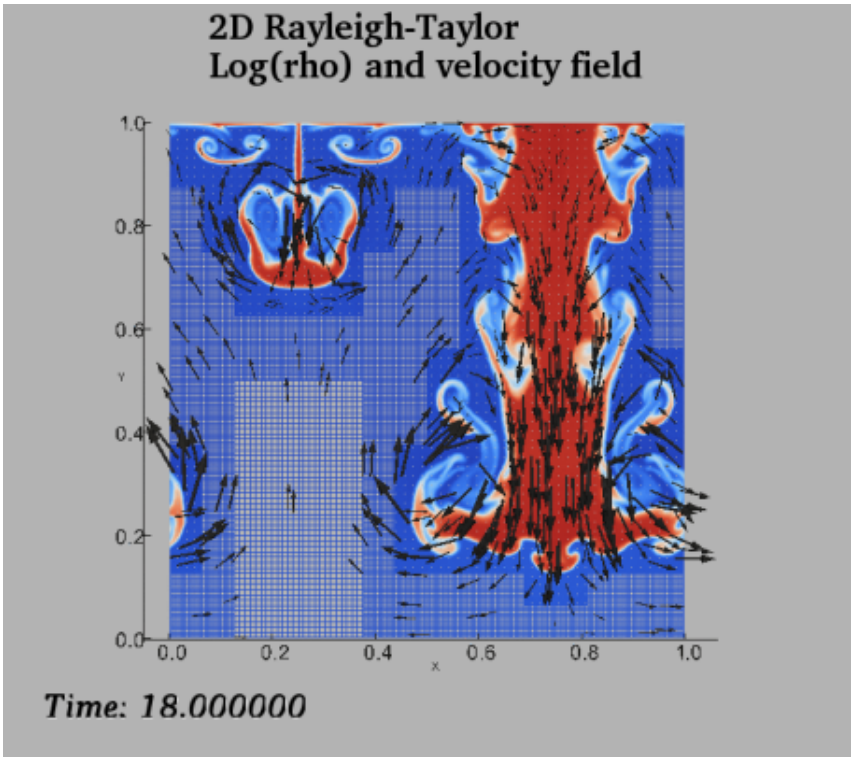

.

Figure 2.1: Example of AMR mesh for RTI. Notice there is an increased number of grid cells around dynamic regions.: http://amrvac.org/md_doc_examples.html

- If the measured local numerical error is greater (lesser) than the user set threshold, the level of the grid cell is increased (decreased).

It is advantageous to use AMR in our simulations as it allows for computationally efficient placement of grid cells to resolve steep gradients, such as the TR and boundaries of the jet, as well as capturing the small scale dynamics. This means that one can increase the grid cells in regions of interest (i.e. where smaller scale dynamics are occurring) based on the numerical error without having to increase the resolution of the whole domain, which would be computationally expensive.

2.2.2 Atmospheric Equilibrium

To model synthetic jets, we need to construct a stratified atmosphere similar to solar conditions. We place the TR at 2 Mm where the temperature smoothly connects an 8000 K photosphere to 1.5 MK corona as shown in Fig. (2.3). The temperature of the atmosphere as a function of height is mathematically

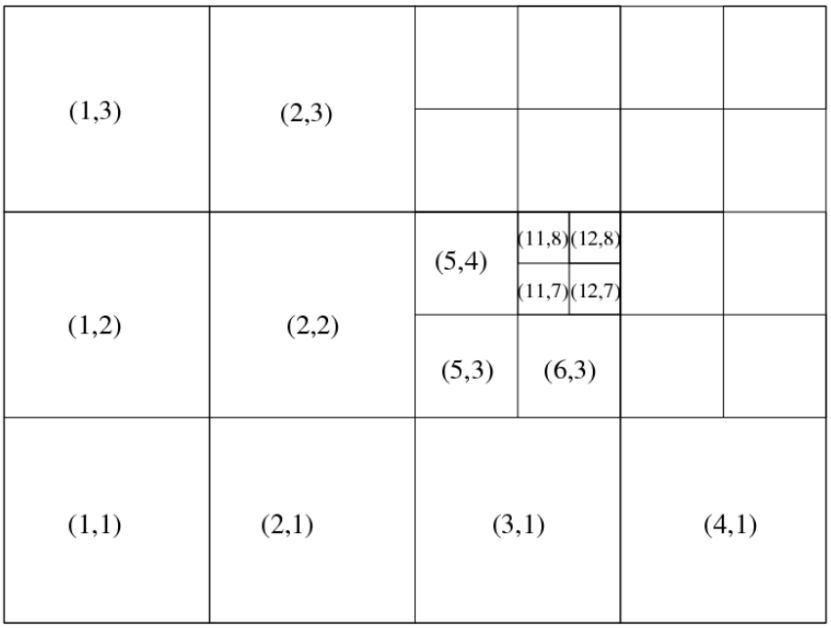

.

Figure 2.2: A generic AMR block skeleton from: http://amrvac.org/md_doc_amrstructure.html

represented as,

$$T_0(y>0) = T_{ch} + \frac{T_c - T_{ch}}{2}\left[\tanh\left(\frac{y-y_{tr}}{w_{tr}}\right)+1\right], \tag{2.9}$$

where y is the vertical position, $T_0(0) = T_{ch} = 8\times10^3$ K ($T_c = 1.8\times10^6$ K) is the chromospheric (coronal) temperature and $y_{tr} = 2$ Mm ($w_{tr} = 0.02$ Mm) is the TR height (width). There is a uniform vertical magnetic, hence $\boldsymbol{j}\times\boldsymbol{B} = 0$ and magnetohydrostatic equilibrium is achieved with,

$$\frac{dp}{dy} = -\rho g. \tag{2.10}$$

Temperature and pressure are related through the ideal gas law,

$$p = \frac{\rho\mathcal{R}T}{M}, \tag{2.11}$$

where M is the mean atomic weight, T is the temperature and $\mathcal{R}$ is the universal gas constant. Therefore, one can obtain the ρ and p in the following form,

$$p(y) = p_0 \exp\left(-\int_0^y \frac{1}{H(y')}dy'\right), \tag{2.12}$$

$$\rho(y) = \rho_0 \frac{T_0}{T(y)} \exp\left(\int_0^y \frac{1}{H(y')}dy'\right), \tag{2.13}$$

where ρ_0 and p_0 are the initial mass density and pressure equilibrium, respectively, at the lower boundary of the computational domain, and the pressure scale heights are given by,

$$H(y) = \frac{\mathcal{R}T(y)}{Mg}. \tag{2.14}$$

Using the temperature profile given by Eq. (2.9) and taking $\rho_0 = 2.34e-4 \times 10^{-4}$ kg m^{-3} we construct pressure and mass density as function of height by means of Eq. (2.12) and Eq. (2.13).

2.2.3 Grid Setup

We set the domain size to 50 Mm $\times$ 30 Mm with a level one resolution of 32 $\times$ 24 (giving a physical resolution of $\sim$ 1.56 Mm $\times$ 1.25 Mm). This coarse level one resolution was chosen to allow the dissipation of shocks as they travel towards the boundaries. To accurately capture the sharpness of the TR, we applied 7 levels of AMR giving a spatial resolution of $\sim$ 12 km$\times$ 10 km. We used unidirectional grid stretching in the horizontal direction, where from the origin the grid cells change by a constant factor of 1.1 from cell to cell. Due to the choice of discretisation scheme for the boundary conditions, we employed ghost cells of 2 grid layers encasing the physical domain in each direction, which have a physical size of 3 Mm. The numerical scheme applied for spatial discretisation is HLL (Harten-Lax-van Leer) Harten et al. (1983) and a third order Čada limiter (Čada and Torrilhon, 2009) for the time discretisation. We used the Courant–Friedrichs–Lewy (CFL) number of 0.8 and generalized Lagrangian multiplier (GLM)-MHD method to maintain $\boldsymbol{\nabla} \cdot \boldsymbol{B} = 0$ (Dedner et al., 2002). For the left and right boundary, we utilised a periodic boundary condition. In the ghost cells of the lower boundary, we fixed ρ, e and $\boldsymbol{B}$ to their initial values. In the ghost cells for the upper boundary the values for ρ, e are determined by the gravitational stratification, and $\boldsymbol{B}$ was extrapolated assuming zero normal gradient. For both upper and lower boundaries, we took an antisymmetric boundary for the velocity components.

2.2.4 Driver

As the driving mechanisms of spicules is an open question, we assumed that the synthetic jet is driven by a momentum pulse from the photosphere to investigate whether simple drivers can recreate the dynamical behaviours of spicules. Rather than going for a pressure pulse, we decided to use a momentum pulse to simulate spicules, as we view spicules as a mass transfer from low

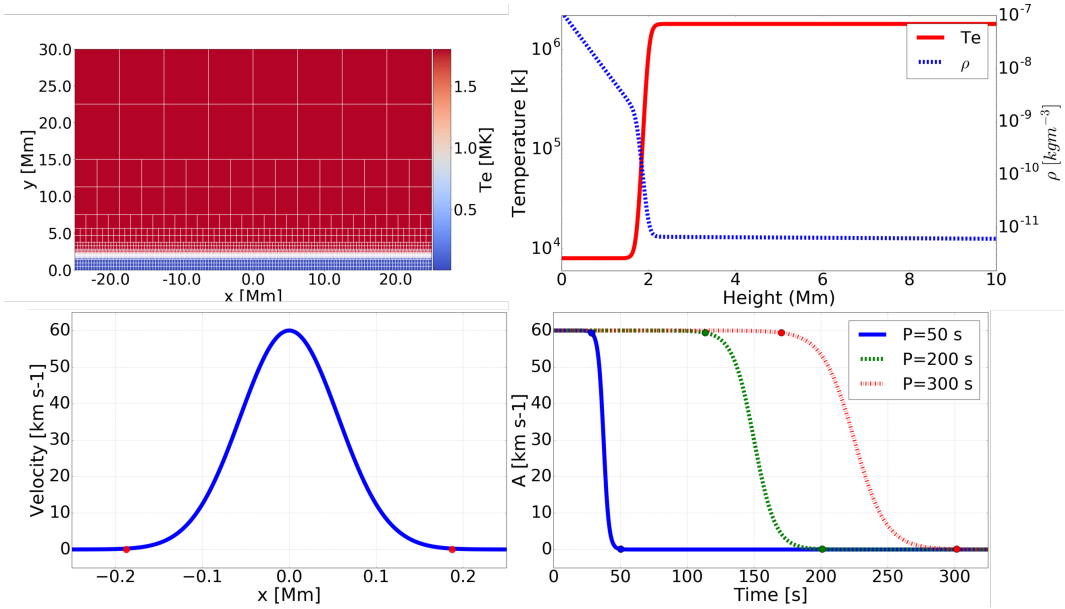

Figure 2.3: The top left plot displays an example of the grid at $t = 0$. The top right plot shows initial temperature (red line) and density (blue dashed) stratification in the first 10 Mm. The lower panels from left to right are an example of Gaussian distribution for $A = 60$ km s^{-1} and $j_w = 187.5$ km marked by red points at $t = 0$ and the driver velocity with $A = 60$ km s^{-1}, $P = 300$ s.

heights, since to our knowledge this is yet to be investigated in a solar context. The jet is launched symmetrically by a driver in the centre of the computational domain which varies both spatially and temporally (see bottom panels Fig. 2.3). In the x-direction the jet velocity is Gaussian with the full width at half maximum (FWHM) of 187.5 km (j_w) and as the jet evolves in time it will reach a switch off phase in which it will shut off with a hyperbolic tangent, as defined by,

$$v_x(x) = \frac{-A\sin\theta}{2}\left(\tanh\left(\frac{\pi(t-P)}{P}+\pi\right)+1\right)\exp\left(-\left(\frac{x-x_0}{\Delta x}\right)^2\right), \quad (2.15)$$

$$v_y(x) = \frac{-A\cos\theta}{2}\left(\tanh\left(\frac{\pi(t-P)}{P}+\pi\right)+1\right)\exp\left(-\left(\frac{x-x_0}{\Delta x}\right)^2\right), \quad (2.16)$$

where A is the amplitude of the driver, θ is the tilt angle from the vertical, P are the driver time, t is time, x is horizontal position, x_0 location of the central jet axis, θ is the launching angles, and the Δx is based on FWHM of the jet width and is given by,

$$\Delta x = \frac{j_w}{2\sqrt{2\log 2}}, \quad (2.17)$$

where j_w is the jet width. The parameter θ can have important implications for the jet dynamics as it causes a discrepancy between jets' propagation direction and the direction of magnetic field. This is explored in Chapter 4 and shows the jet dynamics are sentsitive to the value of θ as shown for small ($\theta < 5°$) and large ($\theta > 40°$) angles of tilt. For $\theta \neq 0$ it increases transverse motions of the jet beam, but for small tilt angles it causes dramatic whiplash motion and for large angles of tilt the jet beam becomes chaotic and less well defined due to large transverse motions.

CHAPTER 3

The Dynamics of Field-aligned Jets in the Solar Atmosphere

3.1 Introduction

The aim of this chapter is to investigate the kinematics and morphology of solar spicular jets under a variety of physical conditions. A peculiar property of the solar atmosphere is that the corona is significantly hotter (approx. 1 MK) than the Sun's surface (approx. $6,500$ K), apparently breaking the 2nd law of thermodynamics. This "coronal heating problem" was discovered by Grotrian (1939) and Edlén (1943) when they realized that a wrongly acclimated new element, coronium, was in fact high levels of ionization of iron, which would only be possible under extreme temperatures. More recently, the appropriateness of the term "coronal heating problem" has been called into question by Aschwanden et al. (2007), who state that it is a "paradoxical misnomer", as there is no evidence of local heating in the corona itself, but rather heating occurs in the TR and upper chromosphere. Essentially, the focus for solving the heating of the solar atmosphere should be shifted to instead solve the chromospheric heating problem, and the way in which heat is transported from these regions into the upper solar atmosphere. Spicular jets are a strong candidate to resolve this problem (Kudoh and Shibata, 1999; De Pontieu et al., 2007b; Martínez-Sykora et al., 2017; Moore et al., 2011; De Pontieu et al., 2017a; Samanta et al., 2019; Zuo et al., 2019; Bale et al., 2019). The energy flux needed to heat the corona is approximately 3×10^5 erg cm^{-2} s^{-1} (Withbroe and Noyes, 1977). The esitmated energy flux hypthesised for spicules ranges from $\sim 1 \times 10^5 - 10^9$ erg cm^{-2} s^{-1} (Athay and Holzer, 1982; Zaqarashvili and

This chapter is based on the following refereed journal article:

Mackenzie Dover, F., Sharma, R., Erdélyi, R.; Magnetohydrodynamic Simulations of Spicular Jet Propagation Applied to Lower Solar Atmosphere Model, *Astrophys. J.*, Volume 913, Issue 1, https://doi.org/10.3847/1538-4357/abefd1.

Erdélyi, 2009; De Pontieu et al., 2011) and with an estimated 2×10^7 (Judge and Carlsson, 2010) Ca II spicules on the Sun's surface at any time, only a small fraction of this energy flux needs to be extracted from a single spicule to maintain the energy budget of the solar atmosphere.

The Sun's magnetic field is omnipresent throughout the whole solar atmosphere, which dictates the flow and dynamics of plasma. This magnetic field is manifested in numerous thin magnetic flux tubes (MFT), which link the photosphere with the corona and facilitate the transport of mass, energy, and momentum across the TR. Moreover, these MFT structures have the potential to act as conduits for magnetohydrodynamic (MHD) wave modes to propagate from lower solar atmosphere to the corona, and to transfer energy between these regions (De Pontieu et al., 2004; Kukhianidze et al., 2006; Zaqarashvili et al., 2007; He et al., 2009a). As outlined in section 1.3, due to multiple observed factors; observed wavelengths, physical characteristics (e.g., length, lifetime, velocity), regions (QS, AR or CH), and/or locations (at-limb or on-disk), MFT structures are categorized as different features (e.g., spicules, mottles, dynamic fibrils, macrospicules, x-ray jets, EUV jets, coronal jets) that permeate the solar atmosphere (see reviews by: Beckers, 1968, 1972; Tsiropoula et al., 2012). In recent years, field-aligned/longitudinal propagation of dominant MHD wave and pulse in MFT structures become has a key focus of research to understand chromospheric heating (Narain and Ulmschneider, 1990; Zaqarashvili and Erdélyi, 2009; Jess et al., 2015). Understanding the propagation of MHD waves and pulses in a dynamic, gravitationally stratified, inhomogeneous environment can provide vital clues about dissipation mechanisms and the formation of shock-like behaviour associated with thin MFT structures. Observations suggest upward flow velocities in the range $15-110$ km s^{-1} for typical lifetimes of between $50-400$ s for off-limb spicular structures (see Table 1.1). The visible apex of these observed features attains a maximum height of approximately 7 Mm and descends back to the surface following a parabolic trajectory (Pereira et al., 2012, 2016).

As highlighted in Section 2.1, many theoretical and numerical approaches have been undertaken to gain an insight into the morphology and dynamical properties of jets in the solar atmosphere. The plethora of models stems from the difficultly constraining parameters with observations and unanswered problems surrounding solar jets: What is their driver? At what height do they originate?

What are their typical density, pressure and temperature profiles? Is the same driver responsible for multiple observed jets, or are there multiple ways of driving the same feature? When it comes to the parameterization of solar jets, the picture becomes muddier when considering the relationship between limb and disk features such as TI spicules, mottles, and dynamic fibrils (see Table 1.1). This makes it challenging, from a mathematical modelling perspective, to determine what are the "correct" parameters on which to base a model. Despite numerous valuable studies, an extensive and qualitative investigation on parameters that influence the observed dynamical characteristics of these spicular features remains missing. In this chapter, we aim to study the propagation of a momentum pulse originating near the photosphere and propagating through the chromosphere and the TR to lower corona in an idealised/stratified solar atmosphere using a simple numerical model. The parameter space comprises driver times, amplitudes, and magnetic field strength, which are examined to assess their role in determining the height, width, and beam structures.

3.2 Parameter Space

Using the numerical setup as described in Chapter 2, we have conducted numerous simulations to quantify the effects of three key parameters; magnetic field strength (B), driver time (P), and initial amplitude (A) on spicular jet's journey through the solar atmosphere. The parameter space covers the values from $P = 50,\ 200,\ 300$ s, $B_y = 20,\ 40,\ 60,\ 80,\ 100$ G, and $A = 20,\ 40,\ 60,\ 80$ km s^{-1} to study the impact on jet morphology (maximum height, width and structure) and kinematics (trajectory, transverse displacement). All ranges are based around typical values for classical spicules (see Section 1.3.1 and Table 1.1). The driver time is chosen within range of the 5-minute oscillations of the p-mode (Leighton et al., 1962), as they are a potential driver for multiple solar features (spicules, mottles and dynamic fibrils) (De Pontieu et al., 2004). In addition, the driver time is based around the measured lifetime of spicular jets (see Table 1.1). The magnetic field strengths are in the range of observed values for spicules, which is consistent with spectropolarimetric estimates for limb spicules (Centeno et al., 2010; Suárez et al., 2015). The range of velocities is chosen based on projectile motion (ignoring drag) to reach spicules' heights. Based on projectile motion, the maximum height for a launching angle of 90° is,

$$h_{max} = \frac{A^2}{2g} \tag{3.1}$$

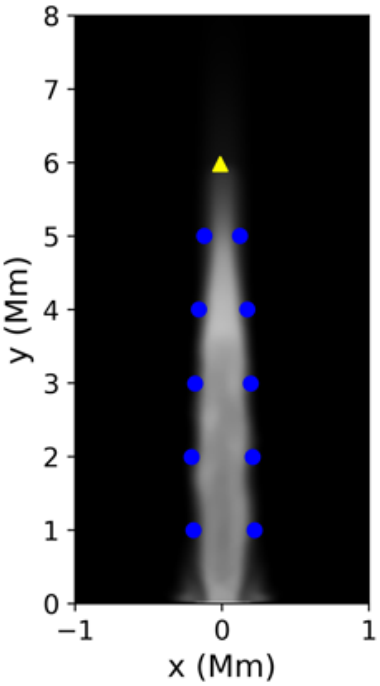

Figure 3.1: Example of jet tracking software that accurately estimates height and cross-sectional width parameters for the simulated jet structure. The jet-apex is marked with a yellow triangle with blue dots on jet edges providing an estimate of widths for each height during different evolutionary phases (rise/fall) of the jet. This figure is available as an animation: https://etheses.whiterose.ac.uk/30244/1/fig_3.1_jet_tracker_example.avi

where A is initial amplitude, $g = 0.274$ km s^{-2} is solar gravity. For $A = 20 - 80$ kms^{-1}, corresponds to $h_{max} = 0.73 - 11.6$ Mm. These values fall in the range of observed speeds (heights) seen in spicular jets which have a range of $10 - 150$ km s^{-1} $(0.4 - 12$ Mm) (see table 1.1). For TI spicule velocity of 80 km s^{-1} is quite high and typically observed for reconnection jets. Despite this we include this high value in parameter scan to cover a large range of values and to see what theoretically occurs for a spicule jet nearer the top end of observed velocities. The magnetic field estimates are consistent with reported magnitudes from spectropolarimetric studies for off-limb spicules (Centeno et al., 2010; Suárez et al., 2015).

3.2.1 Jet Tracking

To understand the jet dynamics, speed, lifetime, trajectory and jet boundary deformation are measured and compared with observational studies. This is achieved by temporally tracking the jet's width (solid blue dots) and apex (yellow triangle), using jet tracking software (see Fig. (3.1)). The jet tracking

software developed for this thesis uses the tracer quantity first introduced in MPI-AMRVAC by Porth et al. (2014). In essence, the tracer is a non-physical quantity, akin to dye injections, which tracks the advection of a selected area of a fluid (in our case flow entering the computational domain). The injected jet material is given a high arbitrary value of 100 (jet value), while the ambient environment is set to 0, and using a threshold of 15%, any snapshot can be split into cells belonging to the jet and ambient medium. This is converted into a binary array where 1 belongs to jet cells and 0 is the ambient medium, which facilitates easy edge detection. The CSW are estimated as a function of the distance between the opposite jet cells at edges, taken from a horizontal slice across the simulated jet at specified heights (see blue dots in fig. 3.1). By having a high resolution with temporal tracking of edges it is possible to obtain useful information of the jet boundary, such as the evolution of boundary deformation at multiple heights. Furthermore, the visible apex of the jet is selected as the highest index of a jet cell in the simulation, which allows us to track the jet's trajectory, speed, acceleration and deceleration (see a yellow triangle in Fig. 3.1).

3.2.2 Jet Trajectories

The identified apex of the simulated jets shows a parabolic motion over time, as shown in Fig. 3.2. The estimated jet trajectories reveal non-ballistic paths of the apex, which is consistent with reported observations (Hansteen et al., 2006; Rouppe van der Voort et al., 2007; De Pontieu et al., 2007b) for chromospheric jets. In the numerical setup, the minimum amplitude for the driver is estimated to be > 20 km s^{-1} for the near-photospheric plasma to attain spicular heights (see Table 1.1). Also, for most cases, the maximum apex for the simulated jets was found to be proportional to the driver amplitude. In each panel, there is a subgroup reaching lower heights due to reduced driving time. We find that our jets have an asymmetric parabolic path as reported in Singh et al. (2019). This could be due to a piling of jet material as the jet begins to fall, as the falling matter will interact with raising matter, slowing the jet's descent.

3.2.3 Effects on Jet Apex and Widths

To understand the impact of the key parameters investigated, we compared how each parameter affects the maximum apex height (panels to the left) and average cross-section width (CSW) (panels to the right) of the jet over its entire life cycle, as displayed in Fig. (3.3). Varying the magnetic field

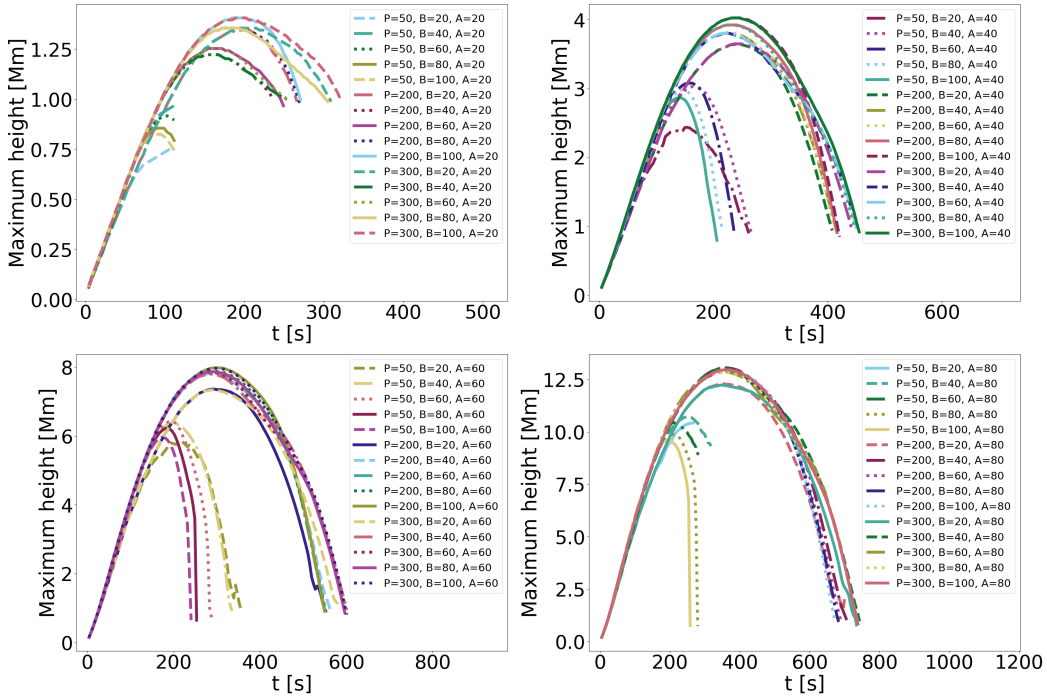

Figure 3.2: Plots show the effects of multiple parameter combinations on maximum apex height attained by the numerical jets'. Results for driver amplitudes with magnitude $A = 20$ km s^{-1} (top-left), $A = 40$ km s^{-1} (top-right), $A = 60$ km s^{-1} (bottom-left), and $A = 80$ km s^{-1} (bottom-right) are shown with jet-apex following a parabolic trajectory. Driver period (P), magnetic field strength (B) and driver amplitude (A) have units in sec, Gauss and km s^{-1} respectively.

strength (B) has less impact on the heights reached by the jet as all cases have shallow gradients, most likely due to the flow of the jet being field-aligned. However, it must be noted that any deviation between jet flow and magnetic field direction can affect the apex height of the jet; this particular aspect is investigated in Chapter 3. The driver time (P) has a nuanced effect, as there is a slight decrease in height for $p = 50$ s, but peaks at $P = 200$ and 300 s. This suggests that to transport significant mass from lower in the atmosphere, an instantaneous pulse will not be sufficient. There needs to be a sustained driver, which past a threshold value, does not impact heights reached, but is important in the behaviour of the CSW variation. Both previously mentioned parameters are grouped by colours and line styles for B and P scans, which correspond to matching initial amplitudes. It is found that the jet height is most sensitive to initial amplitude (A) of the parameters studied. Based on these indications, the jet height is modelled with a power-law function given as,

$$h_{max} = CA^n, \tag{3.2}$$

by collapsing the data by taking an average at each velocity data point and then fitting an optimal curve using least-squares obtaining values of $C = 10^{-2.21}$ and $n = 1.72$ as shown in the bottom left panel in Fig. 3.3. The estimates from the power-law suggest a nonlinear relation between apex height and pulse strength, in contrast to the results reported by Singh et al. (2019), although both results need to be observationally verified. It must also be noted that Singh et al. (2019) used an instant pressure pulse close to the TR as a driver in their simulation, which might not be directly comparable with our investigation. This could be because in this thesis a larger parameter space is investigated, the jets are initiated at a lower atmospheric height, and the jets studied are faster-moving than studied by Singh et al. (2019). By applying probability density functions (PDF) representing various physical parameters of our system we can reveal physical scaling laws and the physical nature of the underlying generation process (Aschwanden, 2019). A power law was chosen as they are a common feature in nature, and indicate scale-free parameter ranges over which nonlinear energy dissipation processes operate, producing coherently amplified events. Based on the presented data there appears to be a parabolic trend that would be captured by a power law distribution. By using a power law to give observers a testable metric to verify the results in the simulation. In future studies the fit of PDFs should be tested as it may indicate different physical relationships behind the parameters driving the jet.

The panels to the right of Fig. 3.3 shows the effect of the parameter space on the mean CSW. To obtain the mean CSW, it is measured at every Mm the jet reaches and the mean value is calculated over the whole life cycle of the jet. Although this is by no means a perfect method, it does give a useful insight into the global deformation of the jet boundary. Our simulations suggest a strong influence of magnetic field strength in determining the widths of the jet structure, with estimated CSW inversely related to the magnetic field magnitudes. This happens because the jet rises through the stratified atmosphere, it has higher internal pressure (as transporting material with lower atmosphere conditions) compared to the ambient medium. This results in expansion of the jet structure and subsequent distortion of the surrounding field. However, in the case of higher magnetic field magnitudes, the jet experiences strong tension forces that result in greater collimation of the jet structure. These results indicate the possibility of lower cross-sectional widths of jet features located near a strong magnetic field environment than those in quiet Sun regions. Another important aspect that influences the jet width is the lifetime of the driver of the jet. The simulations suggest a linear relationship between the driver periods and the jet CSW. This could be due to the long supply of plasma to the jet by a sustained driver resulting in increased CSW. However, the amplitude of the driver had a minimal effect on the width for the jets aligned with radial magnetic fields, although this might not be the case if the jet direction were misaligned with the background magnetic fields.

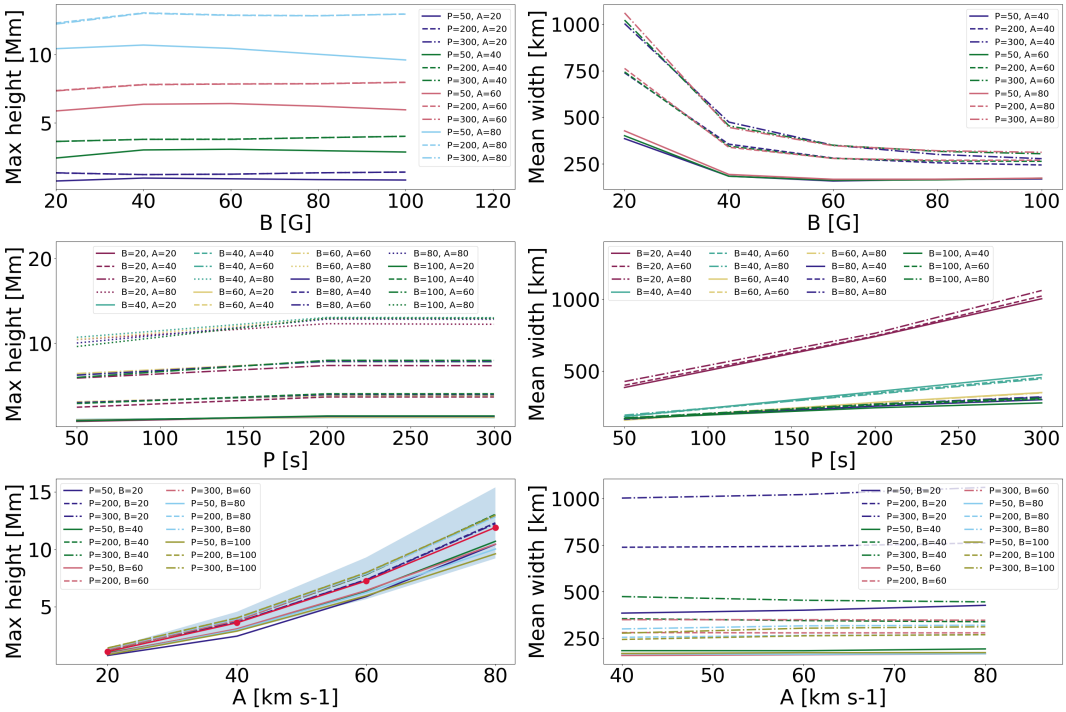

Figure 3.3: Panels compare the effects of different physical parameters (top to bottom: magnetic field strength, driver period, driver amplitude) on the maximum apex height (left) and mean cross-sectional widths (right) for the simulated jet structure. The shaded-region (bottom left) indicates the 1σ error for the power law fit (red line) to the parameter scan. It should be noted that driver period (P), magnetic field strength (B) and driver amplitude (A) have units in sec, Gauss and km s^{-1} respectively.

3.3 Synthetic Jet Morphology

Based on typical criteria for jets of supersonic flows the structures of the jet are akin to a heavy under-expanded jet (Norman et al., 1982; Edgington-Mitchell et al., 2014) as the jet density and pressure are greater than the ambient medium. From the parameter scan, we define a "standard" jet as the one that is most reflective of a spicular jet. The standard jet reaches a height of approx. 8 Mm with a velocity of observed spicules, showing clear boundary deformation, and is suitable middle ground in the range of morphology seen in the parameter scan. This is depicted in Fig. 3.4, with $P = 300$ s, $B = 60$ G and $A = 60$ km s^{-1}, where snapshots of the density (a-d), temperature (e-h) and numerical Schlieren (i-l) are shown.

The numerical Schlieren represents a normalized density gradient magnitude and is defined as follows,

$$S_{ch} = \exp\left(-c_0\left[\frac{|\boldsymbol{\nabla}\rho| - c_1|\boldsymbol{\nabla}\rho|_{max}}{c_2|\boldsymbol{\nabla}\rho|_{max} - c_1|\boldsymbol{\nabla}\rho|_{max}}\right]\right), \tag{3.3}$$

where $c_0 = 5$, $c_1 = 0.05$ and $c_2 = -0.001$. It is important to note while the numerical Schlieren is a physically defined quantity, its use in our analysis is purely from a qualitative perspective as it returns a synthetic shadowgraph image. Shadowgraph images are created by pointing a single light source at a fluid flow in a dark room. It is possible to see the flow patterns because any changes in temperature, pressure, or density, change the refraction index, thus the bending of light rays will create dark and bright regions in the image. An important facet of our simulation is related to the field-aligned jet motions (Fig. 3.4) that show distinct kinematic and morphological characteristics during rising and falling phases in columns (a-b) and (c-d), respectively. In the rise phase (left-panels of Fig. 3.4), the simulated jet shows complex internal substructures and sausage-like deformation of cross-sectional widths in density (a-d) and Schlieren (i-l) data. However, during the fall phase (columns of c-d of fig. 3.4), the complex/internal beam substructure ceases due to driver switch-off. At this stage, the boundary deformation is no longer symmetric, though the jet-axis has noticeable transverse displacement. Modification in sausage-like wave properties associated with CSW estimates during rising and falling phases of simulated jets were recently reported by Dover et al. (2020), as described in more detail in chapter 4. The temperature profile of the numerical jet suggests periodic distortion in the TR layer over the jet lifetime.

The TR deforms as the jet penetrates this layer while generating waves, also known as TR quakes (Scullion et al., 2011). During its entire lifetime, the jet structure remains isothermal/cool without much variation for any combinations of the selected parameters. If the simulations are left to evolve further (approx. $t > 600$ s for the standard jet) then the rebound shock can re-lift the TR as it tries to re-establish an equilibrium after being perturbed by the jet. This is not the main focus of this thesis but is an area of further research. It suggests that a single jet may trigger multiple events from the same location, however, the second would be the rising of the TR rather than the dense plasma jet as shown in this thesis. Without the inclusion of radiative transfer, any significant insight into the potential heating of the solar atmosphere is out of the scope of this research.

Figs. 3.5 and 3.6 showcase the limit cases for the simulated jet with density structure highlighting variations in parameter space in each row for similar time-instance, as shown in fig. 3.4. The panels (a-d) and (e-h) in Fig 3.5 exhibits the effect of strong ($B = 80$ G) and weak ($B = 20$ G) magnetic field strengths, respectively. For the strong magnetic field, the jet was found to be more collimated, with higher density mostly concentrated near the apex. In this case, the complex beam structure is less visible, but due to decreased CSW, it increases the number of knots (areas of enhanced density along the central jet axis) present. The sausage-like jet boundary deformation is less prominent when the magnetic field is stronger. In contrast, in the case of the weak magnetic field, the jet is more diffusive as it balloons out in the solar atmosphere, and due to the large CSW, it decreases the number of knots, as only one is observed. This clearly shows that there is a relationship between CSW and the number of knots. These knots are areas of density enhancements which, when the jet ceases to be driven, flow down the jet to create interesting internal dynamics, particularly in the weak magnetic field example (see (e-f) in Fig. 3.5). Not only are there changes in the jet boundary deformation in the rise and fall phases of the jet, but there are also changes in the jet beam itself, which may be a useful diagnostic for observers when investigating the potential driver for solar jets.

Figs. 3.5 (i-l) and 3.6 (a-d) showcase the effects of high ($A = 80$ km s^{-1}) and low ($A = 20$ km s^{-1}) velocity magnitudes on jet morphology. For higher velocity, the simulated jet had an internal substructure similar to the standard

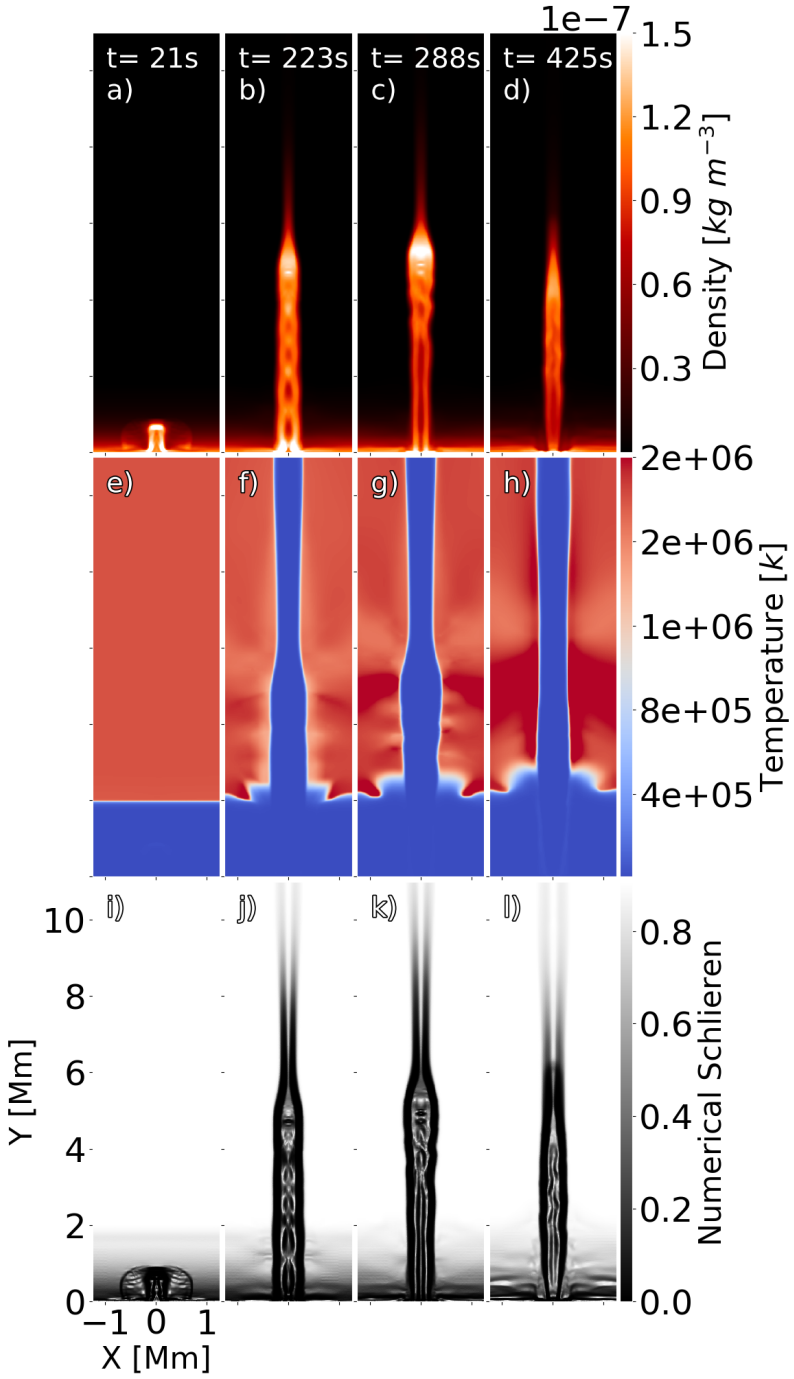

Figure 3.4: Panels show snapshots of temporal evolution of the "standard" numerical jet with uniform radial magnetic field in stratified atmosphere with driver period (P = 300 sec), magnetic field (B = 60 G) and amplitude (A = 60 km s^{-1}). The density (a-d), temperature (e-h) and Schlieren (i-l) images highlight complex internal substructures of the simulated jet with bright apex, possibly due to high-density concentrations. The temperature (middle) panel indicates the isothermal nature of the jet structure with a colder plasma component from the photospheric layer. This figure is available as an animation that runs for 8 s, covering t = 0.0 s to t = 429.4 s: https://etheses.whiterose.ac.uk/30244/2/Fig3.4.avi.

jet, but with more knot features at matching time-steps. The jet shows kinking behaviour from j-l, possibly due to initial high velocity in a slender structure which is more susceptible to kink instability. The transversal displacement travels upwards along the jet beam and starts to bunch closer together when the jet reaches its falling phase, which in turn, changes the directions of flow. For both the standard jet and high amplitude, for example at $t = 288$ s, the internal substructures disappear, indicating a close association between driver time and knots lifetimes. For $A = 20$ km s^{-1} (top panel: Fig. (3.6)), the simulations suggest that for a lower velocity the jet heights are reduced and there is an absence of any significant substructures. The initial amplitudes show that they are a key factor in the dynamics and morphology of the jet, as they are responsible for the complex internal substructures and the CSW variations. The horizontal dynamics are a particularly important aspect of this research, as numerical simulations of solar jets do not typically report on CSW variation, even though in observations of spicules they are not just vertically dynamic, as solar spicules exhibit complex motions horizontally (Sharma et al., 2018; Antolin et al., 2018).

Panels e-f and i-l in Fig. 3.6 highlight the role of driver period for two cases with magnitudes $P = 50$ and 200 s, respectively. In case of shorter driver period ($P = 50$ s), the jet at $t = 21$ s shows a similar evolutionary trend as for the longer durations ($P = 200$ and 300 s), with a lifetime of around $t = 223$ s. For long duration drivers ($P = 200$ s), jet boundaries are smooth and show no kink-like deformation in the fall-phase. A key difference between the two driver periods is the amount of mass injection in the jet, which has direct implications for the CSW as the less time the driver is given to supply energy, the faster the jet boundary undulates.

Overall, the results indicate that changing parameters, whether linked to the driver or the environment through which a jet travels, both have a noticeable impact on the dynamics and morphology of the jet. The parameter scan shows the impact of the morphology of the jet and raises an important question about what is driving these solar jets. This series of simulations suggest that if the driver is an instant pulse/short driving time would lead to very thin, low-density jets without complex structures. It also predicts that in regions with a strong magnetic field the jets would be thin, but denser. For each simulation shown, it displays the jet heads being the densest part of the jet. Observational

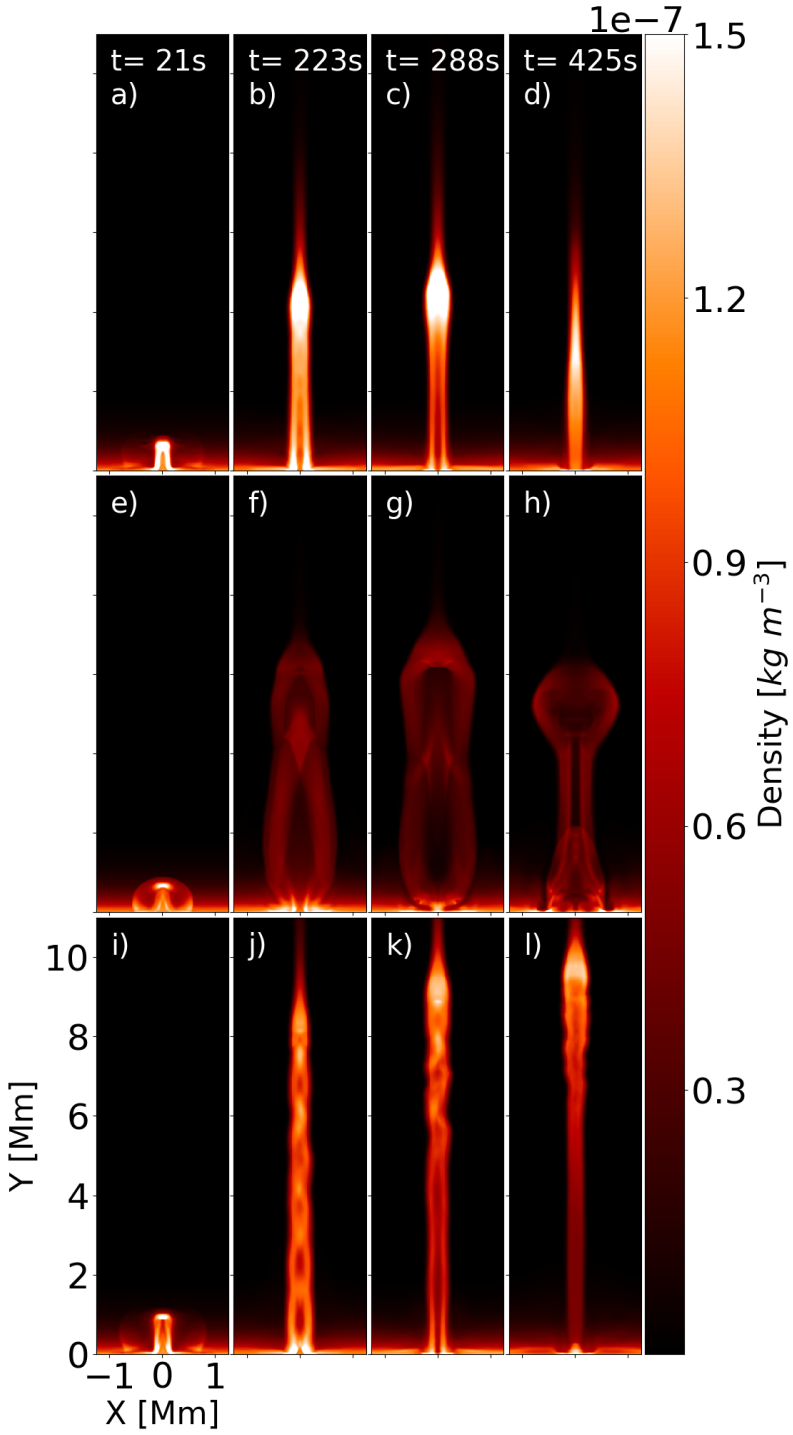

Figure 3.5: Evolution of the synthetic jet with a different combination of magnetic field and driver amplitude parameters, in a stratified solar atmosphere with uniform radial magnetic field. Parameters are varied for the "standard" jet configuration to identify the effects of a particular parameter on jet morphology and kinematics. Panels (top-bottom) show variations with $B = 80$ G (a-d), $B = 20$ G (e-h) and $A = 80$ km s^{-1} (i-l), respectively. Animation available for each case are presented in the top row: https://etheses.whiterose.ac.uk/30244/3/fig3.5___3.6.avi

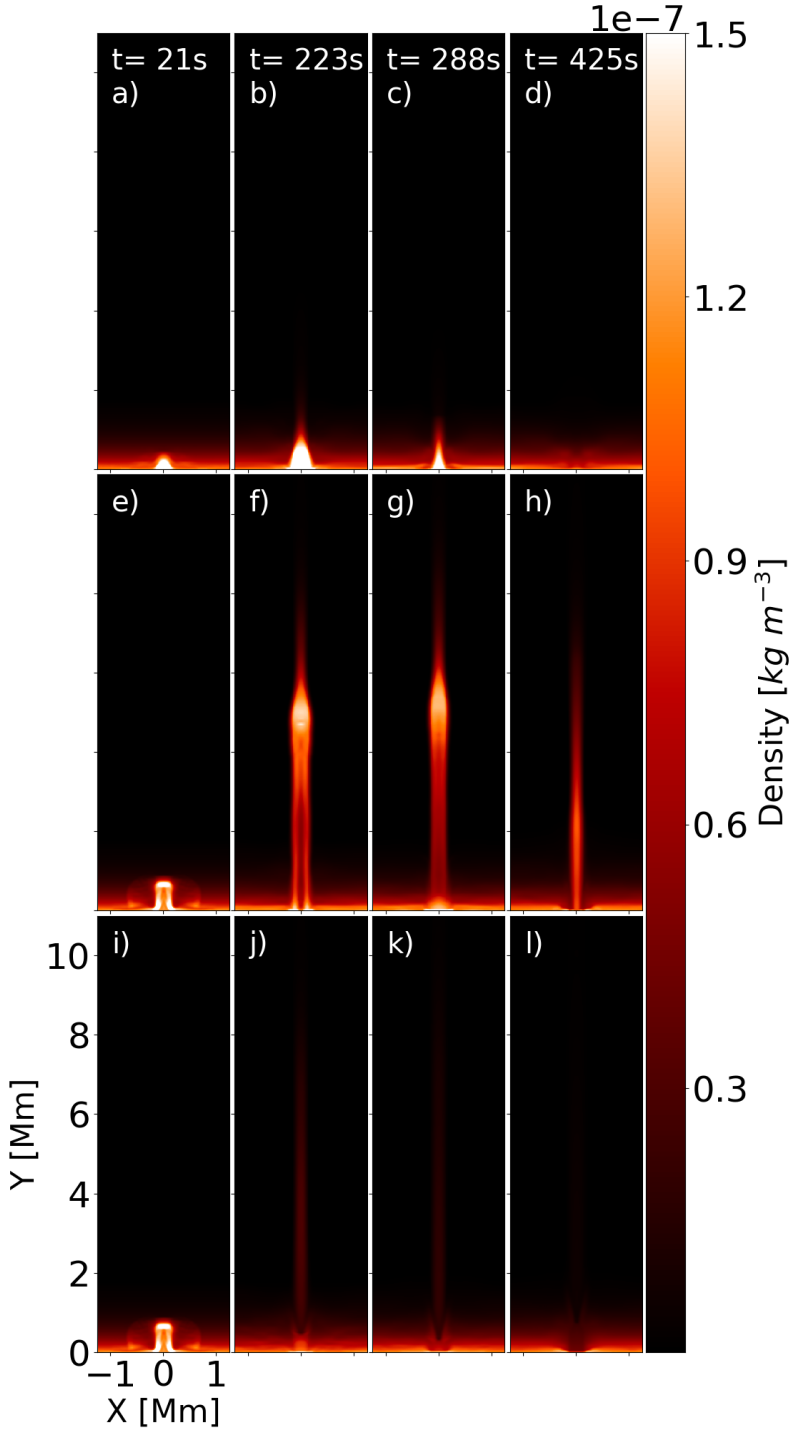

Figure 3.6: Similar to Fig. (3.5) with panels (top-bottom) highlighting variations with $A = 20$ km s^{-1} (a-d), $P = 200$ (e-h), 50 s (i-l) respectively for "standard" jet configuration. Animation available for each case are presented in the bottom row: https://etheses.whiterose.ac.uk/30244/3/fig3.5___3.6.avi

evidence for these bright bulb-like substructures at the jet apex was recently reported in a few studies (De Pontieu et al., 2017b; Srivastava et al., 2018) for chromospheric jets. De Pontieu et al. (2017b) used a combination of 2.5D radiative MHD simulations and observations for spicule structures, and identified bright leading substructures as "heating fronts". These authors proposed the formation of these regions as a consequence of upward propagating magnetic waves and/or dissipation of electric currents due to ambipolar diffusion between ions and neutrals. Srivastava et al. (2018) reported ubiquitous observations of chromospheric jets with a leading bright apex, trailed by a dark region in running-difference images. They labelled these jets as "tadpoles" and suggested the role of pseudo-shocks in the formation of these observed bright substructures.

3.3.1 Jet Beam Structure

Our simulations revealed a yet to be observed phenomenon for spicules, as the synthetic jets contain complex beam substructures. Multiple cases with varied driver amplitudes/periods and magnetic field strength (Figs. 3.4 and 3.6), highlighted criss-cross/knot patterns within the jet beam, along with CSW variations. Complex beam structure seems to be a common feature in the nature in jets, for example with astrophysical (van Putten, 1996; de Gouveia Dal Pino, 2005; Hada et al., 2013; Cohen et al., 2014; Hervet et al., 2017) and laboratory jets (Menon and Skews, 2010; Edgington-Mitchell et al., 2014; Ono et al., 2014). With current resolution limits, these features would be challenging to observe in solar jets. Two possible mechanisms for the presence of the complex beam structures:

1. Knots are the manifestation of non-equilibrium pressure forces prominent within and around the jet structure. As the jet raises it to bring plasma from the lower atmosphere, it thereby has a higher pressure than the ambient medium. Thus, initially, the internal jet pressure results in expansion of the jet which is then counter-balanced by the tension force of the surrounding magnetic field. Eventually, the magnetic pressure dominates the internal plasma pressure, and the jet boundary decreases while resulting in compression of the jet structure. Essentially, there is a "tug of war" occurring between the pressure forces of the jet and the surrounding magnetic field. This process over height and time appears as CSW deformation of the jet, along with the sites of high density/pressure as knots within the jet structure.

2. The knot features could be the sites within the jet structure where internal shock waves become reflected from the jet boundary (Norman et al., 1982). If the jet has supersonic velocities (synthetic jets have Mach numbers are around ∼1-3), it can give rise to a myriad of internal substructures due to high velocities.

Continuing further in the lens of (2), a schematic overview of these beam substructures is given in Fig. 3.7, highlighting two main features, osculating jet boundary and criss-cross pattern formation, that are present in supersonic jets. The boundary deformation arises due to non-equilibrium between the pressure of the jet and the ambient medium. The jet expands from the point of origin as the jet pressure is highest, however, the jet repeatedly overshoots equilibrium points due to the effects of the boundary, communicated to the interior by the sound waves, which are travelling more slowly than the supersonic flow of the jet. Hence, the jet goes through a sequence of expansions and contractions. Not only do supersonic flows give a sausage-like boundary deformation, but the areas of low/high pressure/density are out of phase with maximum/minimum CSW of the jet (see fig. 3.7). This is observed in the numerical jets as highlighted in Fig. (3.8).

The knots inside the jet beam are the manifestation of shock waves trapped inside the jet boundaries. An expansion fan (blue dashed lines in Fig. 3.7) forms at the base of the jet due to the difference in pressure between the jet and the ambient atmosphere. This expansion fan causes an outward flow, making the jet enlarge. The Mach lines of the expansion waves reflect off the jet boundary inwards towards the jet centre in the form of compression waves and a compression fan due to pressure continuity (red lines in Fig. 3.7). The compression waves are reflected at a nearly constant angle from the jet boundary, and as this boundary is curved, the Mach lines of the compression waves tend to converge into a conical shock wave before reaching the centre of the jet. This incident shock either goes under a regular reflection or becomes a Mach disk depending on the angle between the incident shock and the central jet axis, for small and large angles respectively (see black lines Fig. 3.7). These shock waves determine the crisscrossing in the jet beam as well as the shape of the knots. As the flow passes through this shock it increases the pressure in the jet. When the reflected shock reaches the jet boundary it forces the boundary outwards, creating an expansion fan and thus allowing the process to be repeated.

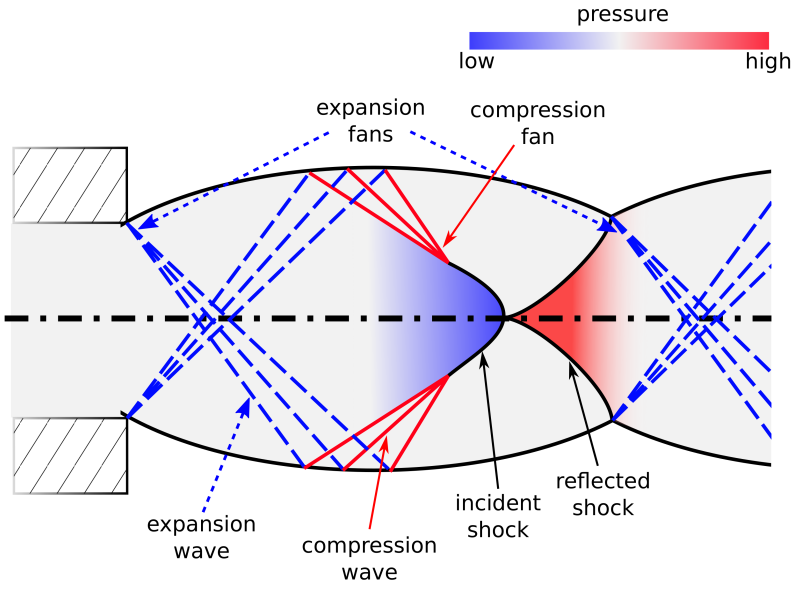

Figure 3.7: A cartoon depicting complex internal substructures in a supersonic jet. The cross-sectional width variations due to formation of regions with high and low pressure as a consequence of internal shock waves, are shown. These wave patterns appear as knots in our simulations, highlighting the role of initial velocity of momentum pulse in generating axisymmetric deformation in a jet structure.

The presence of shock waves in the simulation is evidenced by Fig. (3.9) where each panel displays a time-distance plot for a vertical slices taken in the centre of the computational domain up to 12 Mm for $P = 300$s $B = 60$ G, and $A = 60$ km s^{-1} . In panel (a) the parabolic trajectory of the jet can be seen. In addition the changing position of the knots as the jet evolves are observed. It is clear there is change in the presence of knots once the driver starts its switching off phase as the knots change from undulating to a steep drop in height and density. This further evidences their link to the driver. In panel (b) the temporal changes in temperature is shown. It displays the lifting of the

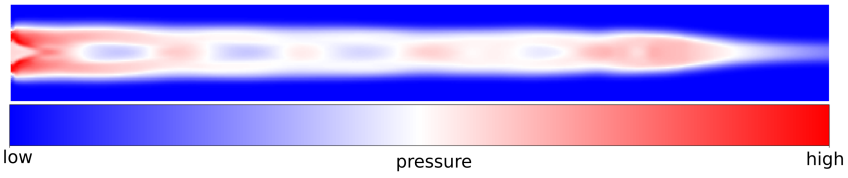

Figure 3.8: Plot of the pressure of the standard numerical jet in a style matching Fig. (3.7) to highlight the similarities.

TR as it is impacted shock waves produced from driving the jet. From 90 s onwards it's clear that 3 main regions of different temperatures correspond to 3 separated velocity fronts as shown in (d). Where the light red and dark red contain subsonic speeds and the change from dark red to blue separate subsonic and supersonic regions. The TR becomes not only a discontinuity in temperature, but also in velocity and is the location of a shock front. In panel (c) the changes in the horizontal velocity is shown. These speeds are subsonic with most variation occurring in the jet beam and significantly slower than the vertical velocity in panel (d). In panel (d) the vertical velocity is exhibited as clearly shows the numerical jets reach supersonic speeds, the sharp changes in colour scheme clearly show the boundaries of shock fronts. It clearly evidences there is supersonic speeds occurring in the simulation where the jet is located and therefore it is entirely possible that shock waves are responsible for the knot structures in the simulations.

These shock waves explains the formation of stationary knots while the flow is active, along with CSW deformations (which do not have an anti-node), density enhancements and cavities in the jet structure. In addition, this provides a vital clue about the disappearance of the complex beam substructures during the driver's switch-off phase. In our simulations, the standard jet (Fig. 3.4) clearly showcase these knots, and their disappearance with the driver switch-off at around $t = 288$ s. Similar behaviour is evident from Figs. 3.5 and 3.6. If this substructure can be seen in jet observations then it gives insight into the driving times.

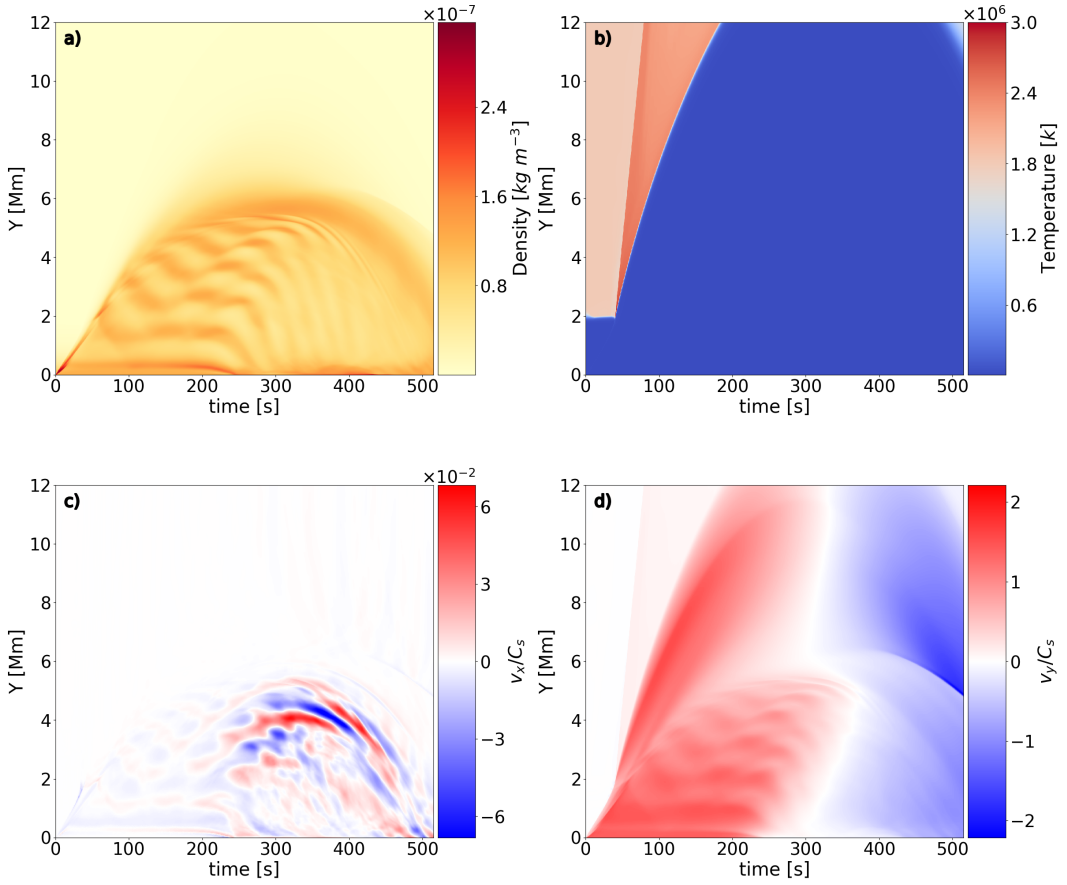

Figure 3.9: Panels show snapshots of temporal evolution a numerical jet with uniform radial magnetic field in stratified atmosphere with driver period ($P =$ 300 sec), magnetic field ($B = 50$ G) and amplitude ($A = 60$ km s^{-1}). Vertical 12 Mm slices are taken at the of the jet beam with a step size of 0.43 s from $t = 0$ to 515 s. The density (a), temperature (b), v_x/c_s (c) and v_y/c_s (d) show the sharp changes occurring as the jet evolves.

3.4 Summary and Discussion

In summary, we have used a simple model to study the effect on jet heights and widths when it is driven by a momentum pulse with enough strength to raise near photospheric material to spicules' heights. This approach is taken to focus on the dynamics of the jets across an extensive parameter scan. The main results of this approach are:

- The visible apex of the jet structure followed a non-ballistic parabolic trajectory with heights comparable with observed spicule motions. A parameter scan suggests a strong influence of driver amplitude in determining the longitudinal dynamics of a jet structure.

- Jets emanating from regions with higher background magnetic field magnitudes are more collimated/dense than those originating in quiet Sun conditions.

- First reports of complex internal substructures are formed during the rising phase of a solar jet structure. These knot patterns are possibly formed due to the reflection of internal shock waves at jet boundaries.

- Temperature maps from our simulations reveal periodic distortions of the transition region due to penetration of jet structure at this layer. However, the jet remained isothermal for its entire life for all combinations of initial parameters. For these simulations, it would be difficult to conclude how much heating these jets can provide to the corona. More physics would need to be added (e.g. radiative transfer and inclusions of neutrals), which is out of the scope of the scientific goals.

- Simulated jets in our study show a bright, bulb-like apex, similar to observed cases of chromospheric jets.

Additionally, the morphology of the synthetics jets is sensitive to the parameters covered in these simulations, i.e. magnetic field strength, driver times and initial amplitude. This may lend credence to linking jet-like events such as dynamics fibrils (AR), mottles (QS) and TI spicules (QS), but apparent differences could partly be attributed to different atmospheric/magnetic environment conditions and differences in parameters of the driver. However, more theoretical and observational evidence is required, for example, running a numerical simulation with the same driver, but changing environmental conditions to match those of observed ARs and QS.

The synthetic jets show interesting internal dynamics in the beam structures, which need to be confirmed observationally. Two possible mechanisms are proposed; (1) "tug of war" of jet and ambient pressure, or (2) shock waves caused by the supersonic flow. However, the supersonic flow framework explains the beam structures that are created, the reason that there are areas of density enhancements referred to as knots, cavities along the central jet axis, and the boundary deformation. Knots are seen in many jets from large astrophysical jets (van Putten, 1996; de Gouveia Dal Pino, 2005; Hada et al., 2013; Cohen et al., 2014; Hervet et al., 2017) to small laboratory jets (Menon and Skews, 2010; Edgington-Mitchell et al., 2014; Ono et al., 2014), hence it makes natural sense that knots are present in solar jets if flow speeds and driver times are sufficient. While this has not yet been observed in small scale solar jets, it is likely due to current resolution limits. In Fig. 3.10, the impact of resolution in identifying these features is shown. For observing spicules the highest spatial resolution is achieved by the Swedish Solar Telescope (SST), at around $70-110$ km (Scharmer et al., 2003a; Berger and Berdyugina, 2003), as shown in panels e-f. It may be possible to identify jet substructures in the foreseeable future with telescopes such as Daniel K. Inouye Solar Telescope (DKIST). DKIST can achieve spatial resolution of approximately $14-60$ km (Rast et al., 2020; Rimmele et al., 2020), which is represented by panels a-d. By achieving higher observational resolution, it will be possible to confirm these beam structures, and also to make significant leaps forward in our understanding of solar jets.

As highlighted earlier, the question of what drives the spicular jet is not yet resolved. The presence/absence of complex beam structures, if observationally verified, would be a significant step forward in understanding the nature of the driver of jets. If observed, then, this can be used to measure lifetime drivers and be used to identify whether a jet is in a rising or falling phase. If they are not observed, then this points towards a short pulse event (e.g. magnetic recognition) as the driver. These substructures could give a new window through which to investigate this phenomenon.

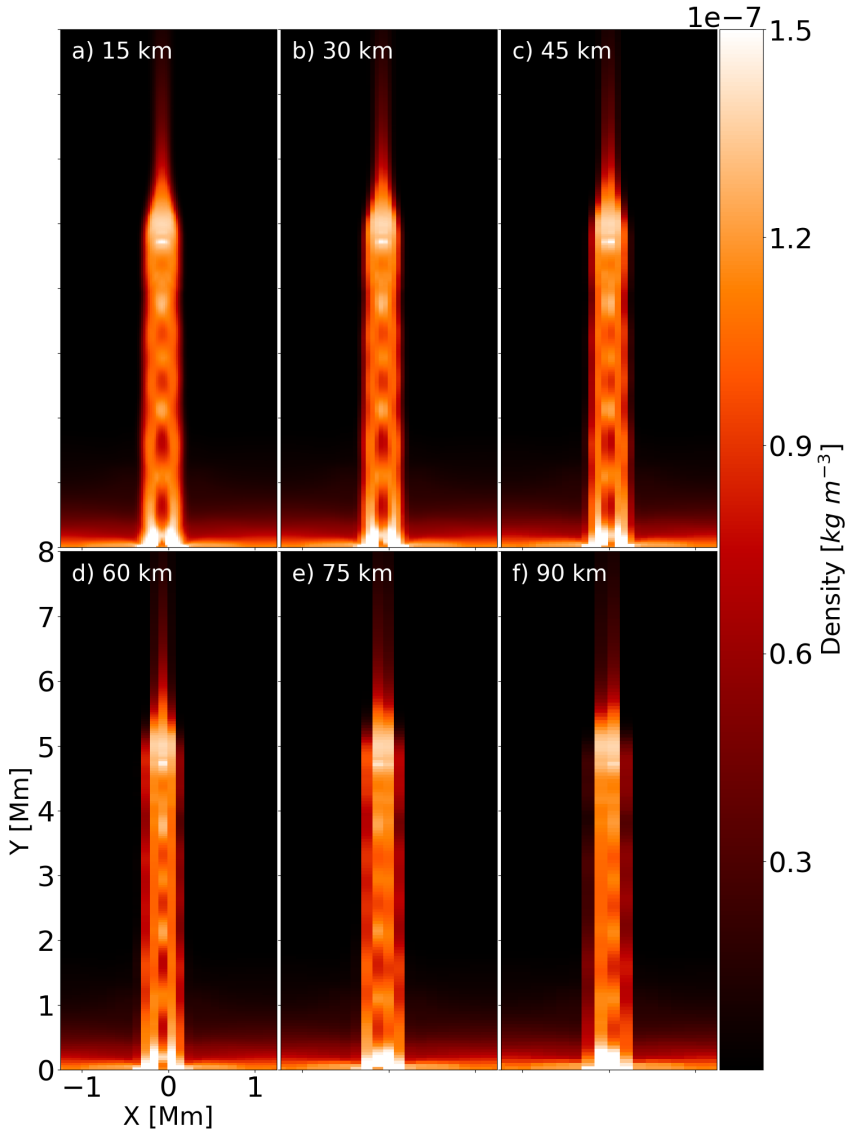

Figure 3.10: Using the same time step as panel (b) in Fig. 3.4, the density grid has been degraded to give a rough estimate of the appearance of the jet over a range of resolutions. The panels a-d give covers the possible resolution range of DKIST and panels e-f show the resolution in ranges of SST.

CHAPTER 4

The Effects of Non-field Aligned Flow on Spicular-jets

4.1 Introduction

A basic question one can ask is, do the flows of plasma in the chromosphere trace the magnetic field lines? Often it is assumed that plasma follows the magnetic field lines in the solar atmosphere. The typical length scale for flows on the Sun tend to be large and the magnetic diffusivity is small, which for ideal MHD means that there is a high magnetic Reynolds number (ratio between advection and diffusion). For a perfectly conducting plasma, the magnetic field lines are frozen into the plasma. This means that the plasma flow is channelled along the field lines, but the perpendicular motion of the flow leads to either the magnetic field lines pushing the plasma or being dragged with the plasma. This is the frozen-in condition that is valid for most plasma features in the coronal environment. However, one can question whether this applies to the chromosphere, where gas pressure can play a more important role than in the corona. de la Cruz Rodríguez and Socas-Navarro (2011) investigated whether solar chromospheric fibrils or spicular features trace the magnetic fields. In most cases, these dynamic features trace the field lines, but there were a significant number of examples where there was a misalignment between the plasma structure and the magnetic field lines (approx. 40% of a sample of 32). This misalignment in extreme cases can be larger than 45°. The misalignment of magnetic field and spicular jets was studied further numerically by Martínez-Sykora et al. (2016) with a 2.5D radiative MHD simulation, which included ion-neutral interaction effects. The results indicate that the majority of the simulated spicules are misaligned with respect to the magnetic field lines. They record misalignment angles up 25°, and in a more extreme case 40°. Even recent simulations of coronal loops have highlighted that misaligned flows could account for observations of dense plasma falling back to

the solar surface (Petralia et al., 2018).

Another aspect to consider is that spicules are typically inclined from the vertical. Some recent studies measure an average incline of 23.4° with a range of $0 - 55°$ (Pasachoff et al., 2009). Tavabi (2012) reported that spicule inclination from the vertical is affected by the regions in which they manifest, e.g. $< 20°$ in polar regions, approximately 10° for CHs, and in ARs they can range from $\pm 60°$. All these results are in agreement with older studies on the average inclination of spicules, which report inclinations ranging between $19 - 35°$ (Beckers, 1968; Mosher and Pope, 1977; Heristchi and Mouradian, 1992; Tsiropoula et al., 2012).

The aim of this chapter is to investigate what effect misalignment between jet flow and the magnetic field have on the dynamics and morphology of spicules. The steps taken follow a similar pattern to that of Chapter 3, where a parameter scan is undertaken and, using the jet tracking code, the jets' apex and CSW are measured, and density evolution is investigated.

4.2 Jet Tracking

To keep the results comparable over a range of tilted jets, extra steps have been introduced into the jet tracking software. To accurately measure the width of the jet we can no longer take horizontal slits (as done in Section 3.2.1) as this could artificially alter the width measurements. For example, imagine a rectangle with a slit across it in a fixed position that finishes on the opposite ends (see (a-b) Fig. 4.1); if one rotates this shape as shown in panel (b), the slit would change in size, hence changing the width measurement of the rectangle as displayed in panel (c). In this case, a slit needs to be placed perpendicular to the central axis, of the rectangle to correct this tilt factor.

Modifications have been made to the jet tracking software to account for this by tracking the central axis (see yellow stars in Fig. 4.2). The yellow stars are the midpoints of horizontal slits taken at 0.1 Mm intervals. To keep the position of the slits consistent, they are placed at every 1 Mm based on the jet's length, rather than the height (see the green solid lines in Fig. 4.2). The slit is placed perpendicular to the angle of the central jet axis determined by the angle between the data point at each megameter of jet length (j_{ln}) and

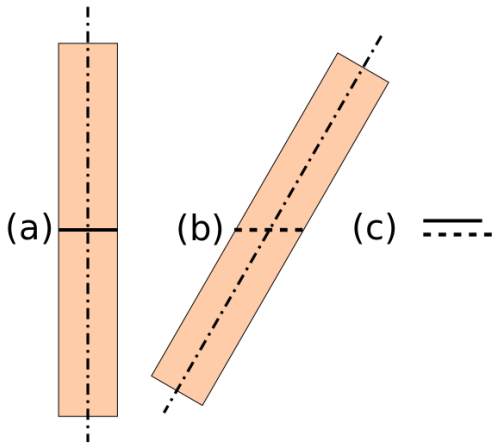

Figure 4.1: Example of widths being increased artificially due to a tilt in flow, where the width is shown by the black line across the orange rectangle. (a) is the width of a straight jet, (b) is the width taken at the same height, but with the tilted flow, and (c) displays the width measures with (a) [(b)] solid [dashed] black line.

its upper neighbour (j_{ln+1}). The edges are identified by first converting the tracer into a binary image as outlined in Section 3.2.1. A region of 1 Mm by 0.75 Mm, with j_{ln} as the centre point is selected. The values along the slit are interpolated from the grid and then a gradient is taken to identify the edges. If only one edge is found then the search box is increased approximately by 60×50 km (see Fig. 4.3) and the process is repeated until 2 edges are found. The solid blue dots in Fig. 4.2 show the method of horizontal slits at every 1 Mm of height as outlined in Section 3.2.1. The analysis carried out in this chapter shows the measurements of both methods of taking slits. They are referred to as traced slits when correcting for tilt angles, and horizontal slits to match the earlier method.

4.3 Parameter scans

Based on the results in Chapter 3, two focused parameter spaces (P1 and P2) are carried out to reduce computational cost. The main goal of P1 is to test the trends observed in Chapter 3, and to determine whether they retain, despite the changes in the flow inclination. The range of values used are: lifetimes with $P = 300$ s, this parameter was found to be less important in determining jet heights over the investigated range, therefore we stick with the standard jet value; initial amplitudes range from $A = 20,\ 40,\ 60$ km s^{-1}, the velocity

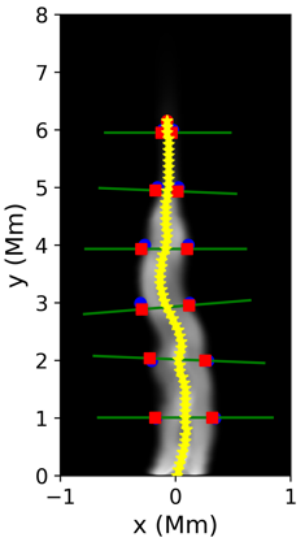

Figure 4.2: Example of extended jet tracking software for $\theta = 10°$. Solid blue dots mark the jet edges of the original method and the red solid dot marks the jet's apex. The green solid line corrects for the tilt and represents the data sampled to find the edges (solid red squares). The yellow stars give the central axis of the jet. Animation is available: https://etheses.whiterose.ac.uk/30244/4/fig_4.2_jet_P300_B60_A60_T10widths.avi.

Table 4.1: Two sets (P1 & P2) of parameter magnitudes, including driver lifetimes (P), velocity amplitude (A), magnetic field strength (B) and corresponding inclination angles for simulated jet structure.

Parameter Scan	P [s]	A [km s^{-1}]	B [G]	θ [°]
P1	300	20, 40, 60	20, 40, 60, 80	0, 5, 15
P2	300	60	60	0, 5, 10, ..., 60

upper limit matches the standard jet and as 80 km s^{-1} is near the upper end of observed spicule velocity, it has been omitted; magnetic field strength covers the same range $B = 20,\ 40,\ 60,\ 80$ G; tilt angles $T = 0, 5, 15°$, this range is to show a small tilt and a value closer to typical tilt angles. The purpose of P2 is to study how the trajectories, CSWs and morphology are affected by the tilting angle of the standard jet ($P = 300$ s, B = 60 G, A = 60 km s^{-1}). A range of tilts $T = 0 - 60°$, in increments of 5° is investigated. Both parameters scans are sumerised in Table 4.1:

4.3.1 Parameter Scan P1

The results of P1 with a horizontal slit are displayed in Fig. 4.4. For each panel, the colour (line style) corresponds to the tilt angle (initial amplitude for

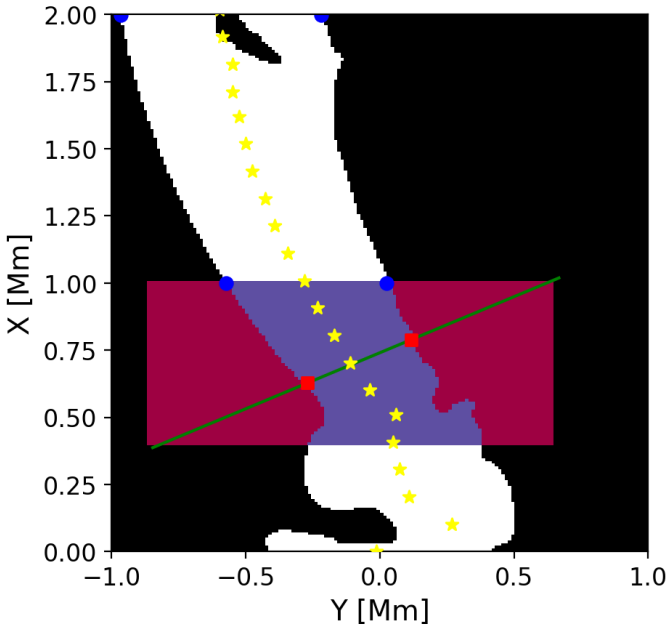

Figure 4.3: Example of a binary image used for the search area (coloured box) used in the jet tracking. Markers have the same representation as Fig. 4.2.

top panels or magnetic strength for bottom panels). From the $\theta = 0°$ data it is clear that in each panel the general trends and groupings are retained. Overall, introducing a tilt into the flow has a subtle effect on jet heights and mean widths. From the relation between maximum heights and magnetic field, the greater the initial amplitude, the more notable the effect the magnetic strength has on reducing apex heights. This trend is seen in the relation between initial amplitude and maximum height, where again, the greater the tilt angle and initial velocity, the more prominent the reduction in height, as the range of values fans out around $A > 40$ km s^{-1}. For both mean width panels, there is not a clear trend on how the tilt affects this parameter.

This process is repeated, but using the maximum length in place of the jet apex and using the traced slits for calculating the mean widths. For the maximum length there is a similar trend to that seen in Fig. 4.4, where the magnetic field does not have a significant impact on jet lengths (except for $P = 300$ s, A $= 60$ km s^{-1}, T $= 15°$ data), and there is a positive correlation between maximum length and initial amplitude. In the bottom left panel, it is shown that the maximum length varies more for $A > 40$ km s^{-1} for increasing tilt angles. In general, it appears that increasing the tilt reduces the length of the jets, because the jet is intersecting the magnetic field, hence the magnetic

field provides a resistance to the jet's forward momentum. An exception is in the case of $P = 300,\ A = 20,\ T = 15$, where the length is increased, which might be due to the combination of a higher velocity jet, with a weaker magnetic field. In this setup the transverse motion would be larger, thus increasing the length, but maintaining a shorter height. The traced slits shows the jets increasingly collimate with the stronger magnetic field (top right panel), and that there is a greater mean width with larger initial amplitudes. The main difference between the traced and horizontal slits is that the traced slits return slightly larger jet widths.

In Fig. 4.5 the same parameter scan is investigated, but using a traced slit to account for the tilting of the jet. The top left panel shows the effect of maximum length against the magnetic field strength. The magnetic field strength, in most cases, does not affect the maximum length of the jet. For $P = 300,\ A = 60,\ T = 15$, increasing magnetic field reduces the synthetic jet's length. For the panel in the bottom left, with $A > 40$ km s^{-1} the tilt begins to reduce the maximum length of the jet, but it shows that the greater the initial velocity the longer the jet length. The panels on the right show the effects of the mean width against the change in the magnetic field strength, and initial velocity, top and bottom respectively. The top right panel shows that with increasing magnetic field straight there is more collimation of the jet. From the bottom left panel, as the initial amplitude increases the greater the jet CSW. The trends that we have seen in Chapter 3 are maintained when the jet is launched at an angle.

4.3.2 Parameter Scan P2

For P2, the effect of the tilt on the CSW measurements and the difference in widths measured using both slits are investigated (see Fig. 4.6). This parameter scan gives a clear indication that increasing tilt angle increases the jet CSWs. At 45° this trend stops, which happens because as the tilt angle increases, the more nebulous the jet becomes. This occurs particularly in the falling phase, when the jet no longer falls as one clearly defined column, thus making it challenging to identify jet boundaries (see (c),(g), and (k) in Fig. 4.14). Both slits display the same trend, but the traced slit (red solid line) consistently measures higher jet widths, which is in agreement with P1.

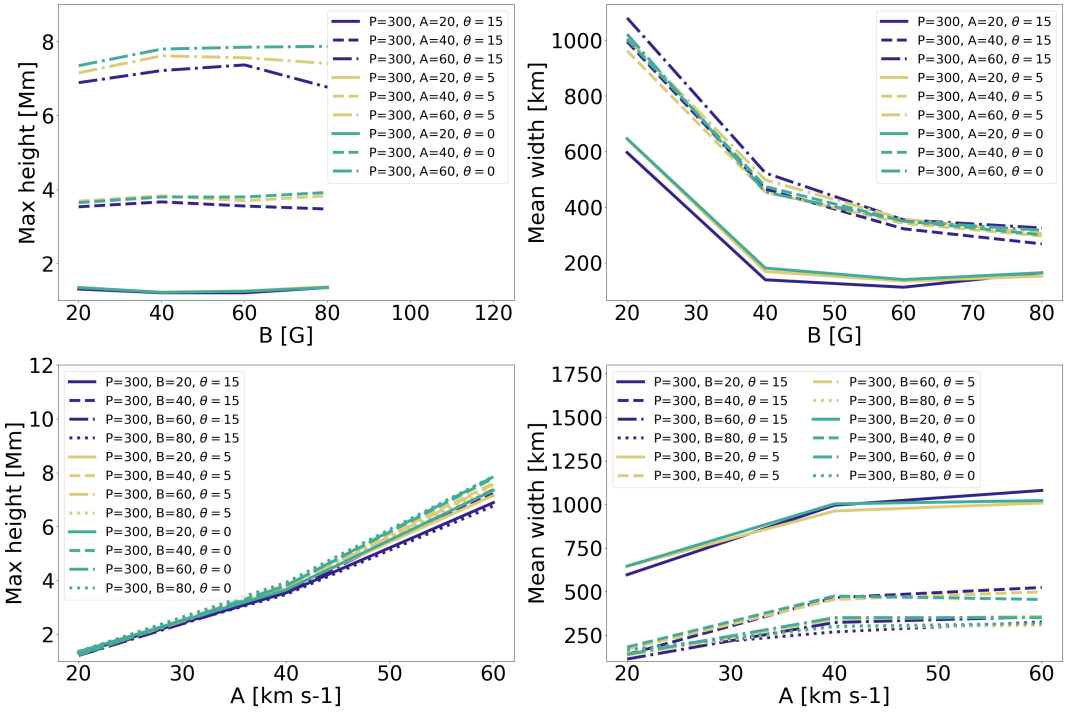

Figure 4.4: Focused parameter scans demonstrate the effect of tilt over a variety of jet configurations. Panels on the left (right) are based on the maximum apex (mean width) of the jet.

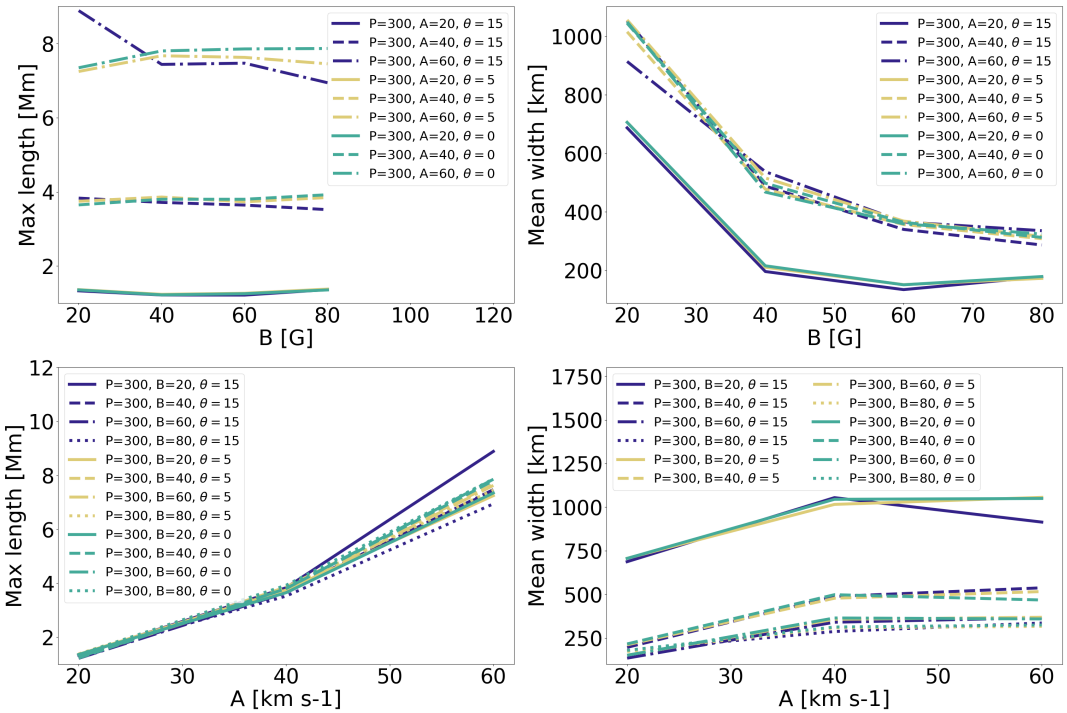

Figure 4.5: Focused parameter scans shows the effect of tilt over a variety of jet configurations. Panels on the left (right) are based on the maximum length (mean width) of the jet.

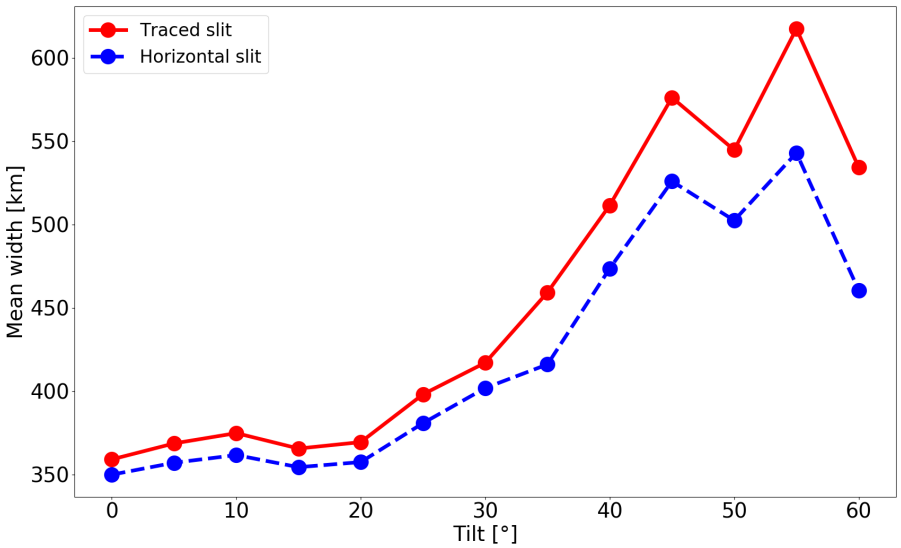

Figure 4.6: Effect of tilt on the mean width measurement, comparing traced slit (red solid line with data markers) and horizontal slit (blue dashed line with data markers).

The analogous trends for both slits originate from the method of angle selection for the traced slits. This is due to the tracking of the central axis of the jet being determined by horizontal slits with small intervals. In combination with a small sample of data points being used to determine the tilt angle, this means that the width measurements may not deviate much from the original slit method. It is possible that a different method of identifying the central axis and/or more data points used for angle determination would modify the trend for the traced slits. Overall, even the less sophisticated method currently used is an improvement on the horizontal slit method and gives an accurate measure of the mentioned jet parameters. However, future improvements are outlined in Section 6.2.

The apex height and length of the jet are tracked and displayed in the left panel of Fig. 4.7. There is a clear trend, in that both the maximum height (solid black marked line) and length (dashed red marked line) are decreased with a tilting angle. The maximum length is larger than height, and the difference widens above 20°. The increased difference between height and length can be attributed to larger transversal displacement with increasing tilt. Both trajectories of the jet (right-hand panels) display a decrease in max-

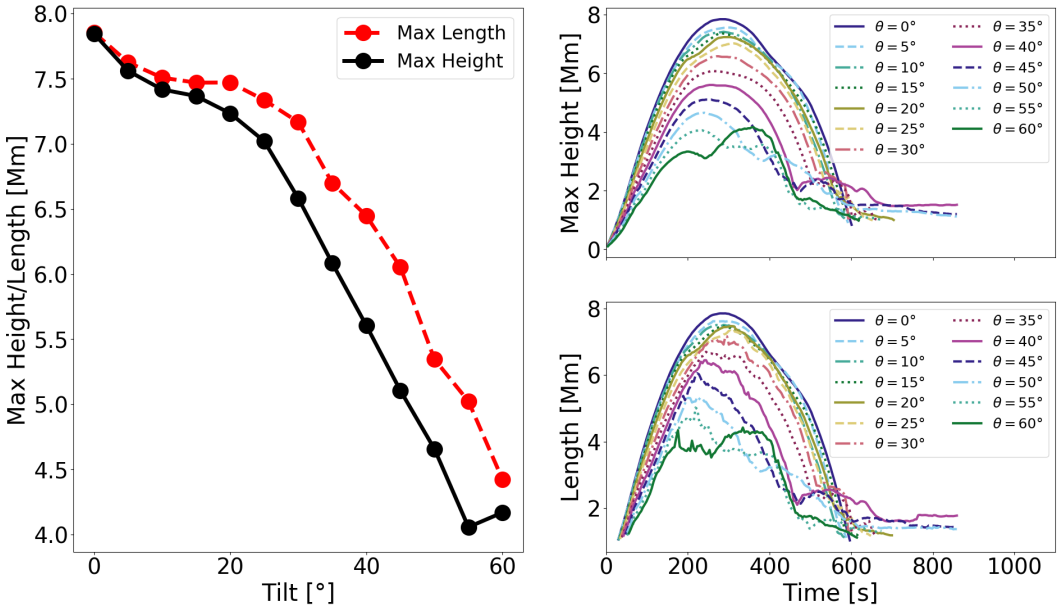

Figure 4.7: Plots shows the effect of non-field aligned flow on apex (top panels), length (bottom panels) and trajectories (rightmost panels).

imum height/length and a slight decrease in jet lifetimes of about 150 s, over the range of tilt angles. The results indicate that once tilted up to 50°, the trajectories deviate from what is typically seen in spicular jets. A similar pattern is seen when the jet length is tracked, but the trajectory is less smooth. This latter is because the jet is undergoing transverse motion and is constantly changing in length. These results indicate that both the magnetic field and horizontal perturbations could alter the trajectory of the jet.

An interesting aspect of the results is that introducing a small tilt in the flow has produced spicules with differing heights and lifetimes. This means that, a spicule generated with similar energy can appear differently due to non-field aligned flows, which with more misalignment causes shorter heights and lifetimes. This latter finding could explain why spicules appear and disappear over a variety of heights. However, unlike the situation with TII spicules, their appearance would be similar to their higher propagating counterparts. It is only in an extreme case of tilt angles (approx. 50°) that the trajectory significantly deviates from a parabolic flight.

4.3.3 Tilted Jet Morphology

Figs. 4.11 to 4.14 visualise the density evolution for the standard jet at various tilt angles. The first row of Fig. 4.11 serves as a reference to the $\theta = 0°$ jets described in Chapter 3. Note that in Figs. 4.11 to 4.13 the timesteps selected are the same as in the simulation snapshots in Chapter 3, this is purposefully chosen for comparison.

An interesting aspect of the simulation is that even for small tilting angles of $5 - 10°$, the morphology of the jet is significantly changed, particularly in the falling phase shown by columns containing panels (c-d). At about $t = 253$ s for 5° and 10°, the jet experiences an instability, causing a kinking motion to travel through the jet beam, giving a whip effect (see panel (g) in Fig. 4.11 for aftermath). This whip motion causes significant mixing to occur in the jet beam (see panels (g) and (k) in Fig. 4.11). This is also observed for higher degrees of tilt, but does not cause significant mixing in the jet beam. Another phenomenon observed in jets with higher degrees of tilt ($> 20°$) is finger-like structures occurring in the down-flow of the jet, both in the jet beam and its right-hand side boundary. Both these dynamics are likely produced by instabilities. In both cases, to determine precisely which instabilities cause these dynamics is not a trivial task and requires further investigation. Despite this, from their appearance and with the data available, it is possible to narrow down to three potential candidates:

1. Rayleigh-Taylor instability (RTI) is the instability of an interface between two fluids of differing densities, where the heavy fluid is on top. If this system is subjected to gravity, then any slight perturbation leads the denser fluid to fall through the lighter fluid, forming finger-like structures as shown in Fig. 4.8.

2. Kelvin-Helmholtz instability (KHI) occurs if there is a velocity shear in a single continuous fluid. The shearing between these two fluids, once above a critical threshold, causes the interface to form vertices; see Fig. 4.9.

3. Dynamic kink instability (DKI) occurs when plasma flows on a curved trajectory. There are two opposing forces acting on the jet; the centripetal force which is trying to destabilise the flow, and the Lorentz force which is acting to stabilise the flow, as shown in Fig. 4.10. If the

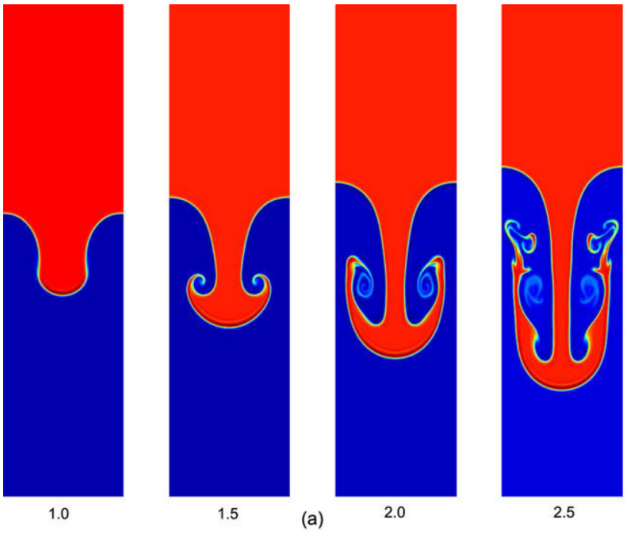

Figure 4.8: Example of the formation of an RT instability at various time steps. These are results from a simulation shown in Liang et al. (2019). The red-coloured fluid represents a denser fluid than its blue counterpart and gravity is directed downwards leading to the formation of RTI.

flow is super-Alfvénic then the centripetal force can outweigh the Lorentz force, enhancing the transverse displacement. This instability occurs in HD but is called a kink instability (KI) (not to be confused with MHD KI), which like the DKI is caused by centripetal force in curved flows (Drazin, 2002). Note that this instability, is different from an MHD kink instability which arises due to the Lorentz force enhancing kink motion.

From the list of potential instabilities, the two candidates for the whip effect are KHI or DKI. KHI is observed in many instances in nature, e.g. from clouds, waves in the ocean, and Jupiter's eddies *etc.* They are present in numerous solar features: coronal mass ejections (Foullon et al., 2011, 2013), coronal loops (Barbulescu et al., 2019), prominences (Berger et al., 2010; Ryutova et al., 2010), solar jets (Filippov et al., 2015; Li et al., 2018), and spicules (Kuridze et al., 2016; Antolin et al., 2018). As there are significant velocity differences between the jet and ambient medium, the interface between these two regions can become KH unstable. This can lead to deformation of the jet boundary and if shearing is strong enough, it can destabilise the jet. However, Chandrasekhar (1961) has shown that a magnetic field aligned with the flow will impede the development of KHI, which is the case of the simulation showcased. Another aspect to consider is that KHI would be localised to the jet boundary, and would not propagate through the jet beam as seen in the simulations.

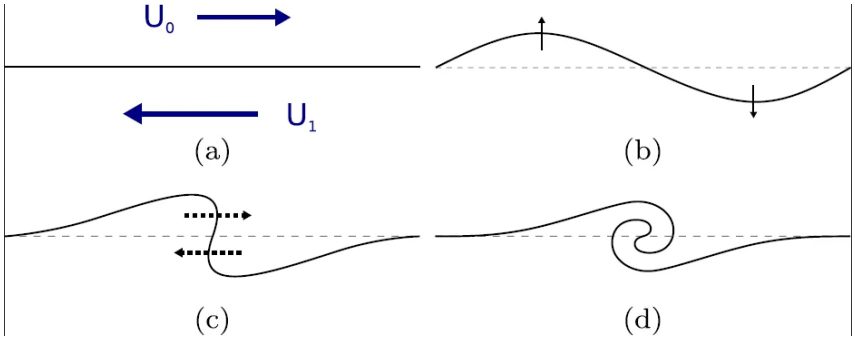

Figure 4.9: Example of the formation of a KHI taken from Barbulescu and Erdélyi (2018). Stage (a) shows the interface between two fluids where U_0 and U_1 are arbitrary flow speeds before they are subject to a perturbation shown in stage (b). In stage (c) the perturbation is enhanced by the flows creating non-linear wave steepening. This leads to stage (d) where a vortex forms, mixing both fluids.

Due to these factors, it is unlikely that KHI is responsible for the whip effect occurring in the simulations.

A strong candidate to explain the whip effect is the DKI. Zaqarashvili (2020) proposed a model showing DKI could cause transverse motions in spicules. If a spicule is travelling at an angle (in their case the curve was introduced by considering a vertically expanding flux tube) and the flow is super-Alfvénic, then DKI can enhance transverse motions. DKI can explain the presence of the whiplash motion going through the jet. More investigation is needed to understand why at shallow angles of $5-10°$, mixing occurs in the falling phase of the jet beam. One possibility is that above 15° horizontal motion is sufficient to dampen the instability due to the magnetic field. The magnetic field is acting as a brake to the jet flow, i.e. the more tilt, the more impeded the jet will be thereby resulting in smaller up-flows and a reduction in the effect of the DKI. Interestingly, the whip motion can be seen in Fig. 3.5 for $A = 80$ km s^{-1}, which does not fully fit in with the DKI, because the flow is not on a curved trajectory.

Two possible instabilities to account for finger-like structures in the falling phase of the jet for tilts between $20-45°$ are RTI and KHI. RTI is hypothesised to form at prominence boundaries (Berger et al., 2008, 2010; Hillier et al., 2012; Berger et al., 2017), but for spicules, there is no strong observational evidence for RTI occurring. Numerical simulations of astrophysical jets have

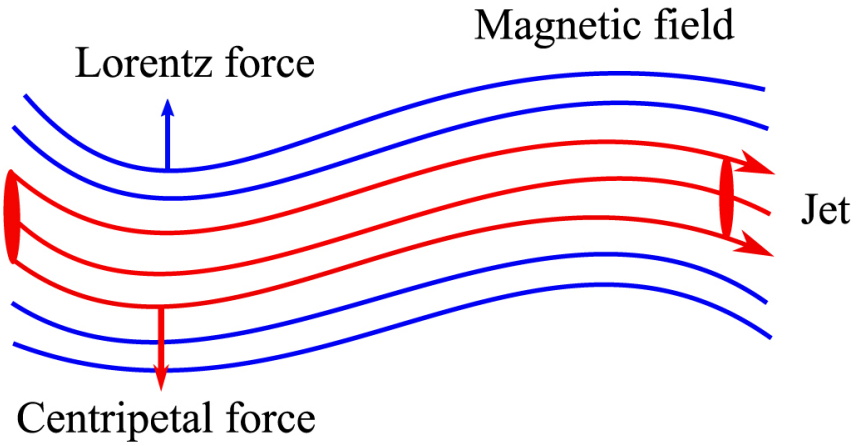

Figure 4.10: Cartoon of dynamic kink instability taken from Zaqarashvili (2020). The blue (red) lines represent the magnetic field (jet). The blue (red) arrow shows the direction for the Lorentz (centripetal) force.

shown that RTI instability can occur at the jet boundary, where the finger-like structures are seen in the perpendicular cross-section with regard to the central jet axis (Toma et al., 2017; Matsumoto et al., 2017), and laboratory plasma jets have shown evidence of RTIs (Zhai and Bellan, 2016). It may be that with a 3D version of the synthetic jet simulation, RTI would form at the boundaries of the jet. The lack of observations of RTI in spicules, and the fact that RTIs would be oriented in the direction of the magnetic field, makes it unlikely that these are responsible for the finger-like structures seen in the simulations. It is more likely to be KHI, as the finger-like patterns form in the falling phase of the jet where there will be an interaction of up and down flowing material, causing increased shearing. The finger-like structures appear near regions of high density, which are located near the edges of the greatest transverse displacement. With higher resolution or less diffusive numerical schemes the KHI could appear as vortices at these locations.

The tilt has an important impact on the structuring of the beam. The main noticeable difference is the appearance of knots, as seen in columns containing them (b) in Figs. 4.11 to 4.14. For tilt $< 15°$ the knots are denser and deformed, but for higher degrees of the tilt ($> 10°$) the knots are no longer easily identified. This would mean only slight horizontal disturbance to the jets would make it even more challenging to identify knots if present in observations. The tilt causes the densest parts of the jet to change from being contained to the head and knots, as seen in Chapter 3, to the edges where the

most transversal displacement is. The greater the tilt, the more the edges of transversal displacement become the densest part of the jet, and the rest of the jet beam reduces in density. The column containing panel (d) reaffirms the earlier result that the jet has a lower apex and reduces the jet lifetimes for increasing tilt.

Another method of producing tilted jets would be to incline the magnetic field instead of changing the direction of the driver. The impact of the inclined magnetic field has been investigated in numerous studies for laboratory, astrophysical and solar jets (Koide et al., 1996; Hurka et al., 1999; Murawski and Zaqarashvili, 2010; González-Avilés et al., 2017, 2021; Revet et al., 2021).

Koide et al. (1996) studied the impact of the oblique magnetic field in 2D and 3D simulation to understand the bending of astrophysical jets. They found that the bending scale of the jet depends on the jet velocity and the magnetic field angle with respect to the jet. If the jet has a high Alfvén Mach number (> 2.5) then the jet goes straight compared to a jet with a lower speed. The magnetic field with the angle between the jet and magnetic field of 45° bends the jet most quickly. In all cases, the tilting of the magnetic field causes compression at the jet head and deceleration of the speed of the jet. Hurka et al. (1999) investigates whether strong magnetic fields can bend stellar jets. In their 3D study, they find a critical velocity v_{cr} that determines if the jet is deflected by the ambient magnetic field. They find almost a linear dependence of the v_{cr} and the ambient magnetic field. However, one should note that in this study the jets occur in an environment very different from the solar jets. For example, the magnetic field strength is much weaker than investigated in this thesis ($50 - 100$ μG), but with similar velocity scales ($2 - 40$ km s^{-1}) and tilt angles from $10 - 70°$. Both Koide et al. (1996); Hurka et al. (1999) show a general bending of the whole jet due to the magnetic field rather than the kinking motion seen in the simulation presented in this thesis. However, it would be interesting to see what the value of v_{cr} would be in a solar context.

In González-Avilés et al. (2017) they simulated a solar reconnection jet with the interaction of two magnetic arcades of different polarities. When the magnetic field is set up in an asymmetric manner it gives a tilted launch angle for the reconnection jets. This produces a jet that travels at an angle with speeds ranging from $3.7 - 76.5$ km s^{-1} and shows transverse displacement of

the main jet beam in the falling phases similar to what is seen in the simulation presented in the thesis. In both Murawski and Zaqarashvili (2010) and González-Avilés et al. (2021) they carried out 2D simulation exciting spicules and macrospicules, respectively by placing a velocity pulse just under the TR at 0.5 and 1.75 km. The jets initiated in both these studies follow the magnetic field lines and don't exhibit the transverse motions shown in tilted numerical jets in this thesis. For the marcospicules the initial velocity pulse was at a higher value than used in this thesis set at 100 km s^{-1}. It should be noted that neither of the simulations will show a significant transport of dense jets due to the location of where they were driven. In general, it seems the main effect of tilting the magnetic field is that it bends the jets and would reduce the maximum height of the jet and decelerate the jet speeds. Another difference introduced in the context of the simulations in the thesis is that inclining the magnetic field would extend the time the jet travels in the lower atmosphere before reaching the TR. The jet would perturb TR at an angle affecting the trajectory of the TR as it lifted, so the TR will raise at an angle rather than purely vertically. When the TR falls and produces a rebound shock this would no longer be symmetric and would affect the waves that would propagate along the TR layer.

4.3.4 Effect of Tilt on Cross-sectional width variation

By introducing tilt into the jets, they not only undergo CSW variations but also transverse motions. These are two key dynamical ingredients that need to be captured in spicular models. Spicules are not just vertically dynamic plasma sticks, they display complex motion all through the body of the jet (Sharma et al., 2018).

Using the horizontal slits time-distance plots were created at $1-3$ Mm heights (see Figs. 4.15 to 4.17), over the range of tilts. From Fig. 4.15 for $\theta = 0°$ there are clear sausage-like motions in the CSW variations. It shows that there is a cavity inside the jet, which is due to the process that creates the knots. Even with the smallest tilting angle ($\theta = 5°$) investigated, it makes substantial changes to the CSW variations of the jet beam. This appears to be the only example where the combination of both CSW variations and transversal displacement can be cleanly observed at this height, as with increasing tilt the sausage-like CSW variations become less noticeable. The main dynamics shift from symmetrically CSW variations, to transversal displacement that reaches

up to approximately 1 Mm in width. For a tilt of $\theta > 25°$ the most horizontally displaced regions have much denser edges. These could be regions where the material is building up due to the magnetic field redirecting flow as it is perturbed. With increasing amounts of horizontal velocity, the more the jet travels into the magnetic field, hence the jet material collects at turning points creating denser regions at the jet boundary. For the tilted jets, the large scale transverse motions in the simulations are due to the restoring forces of the ambient magnetic field, which are trying to re-establish an equilibrium. Once the tilt passes $\theta = 40°$, there is less of a clear jet structure. Similar behaviour is seen at 2 Mm and 3 Mm (Fig. 4.16 and 4.17), where there appears to typically be one-two global sways of the jet during its lifetime. This shows that the wave-like motion propagates throughout the jet.

The whip motion has been observed in chromospheric jets (Liu et al., 2009). In Liu et al. (2009), the observed jet undergoes a transverse disturbance with a whip motion. This jet has length scales (approx. 43.5 Mm), lifetimes (approx. $>$ 1hr), observed speed (approx. 430 km s^{-1}), and proposed origin is magnetic recognition. The whip motion is proposed to be due to the jet being composed of helical threads undergoing untwisting spins, outlined by Shibata and Uchida (1985, 1986) and Canfield et al. (1996). Although the phenomena has very different origins and scale, the overall motion time-distance plots, present in Liu et al. (2009), appear similar to time-distance plots presented in Figs. 4.15 to 4.17 that are proposed to be produced by DKI. This whip motion has been shown in simulations of reconnection jets, where material from the chromosphere is ejected by a sling-shot effect due to reconnection and produces a whip motion (Yokoyama and Shibata, 1996; Kotani and Shibata, 2020). We do not disagree with these outlined mechanisms, but DKI could be playing a role in the transverse motions. DKI could form as in this reconnection jet scenario there is both curvature and horizontal perturbation to the magnetic field, in addition to a fast flowing jet.

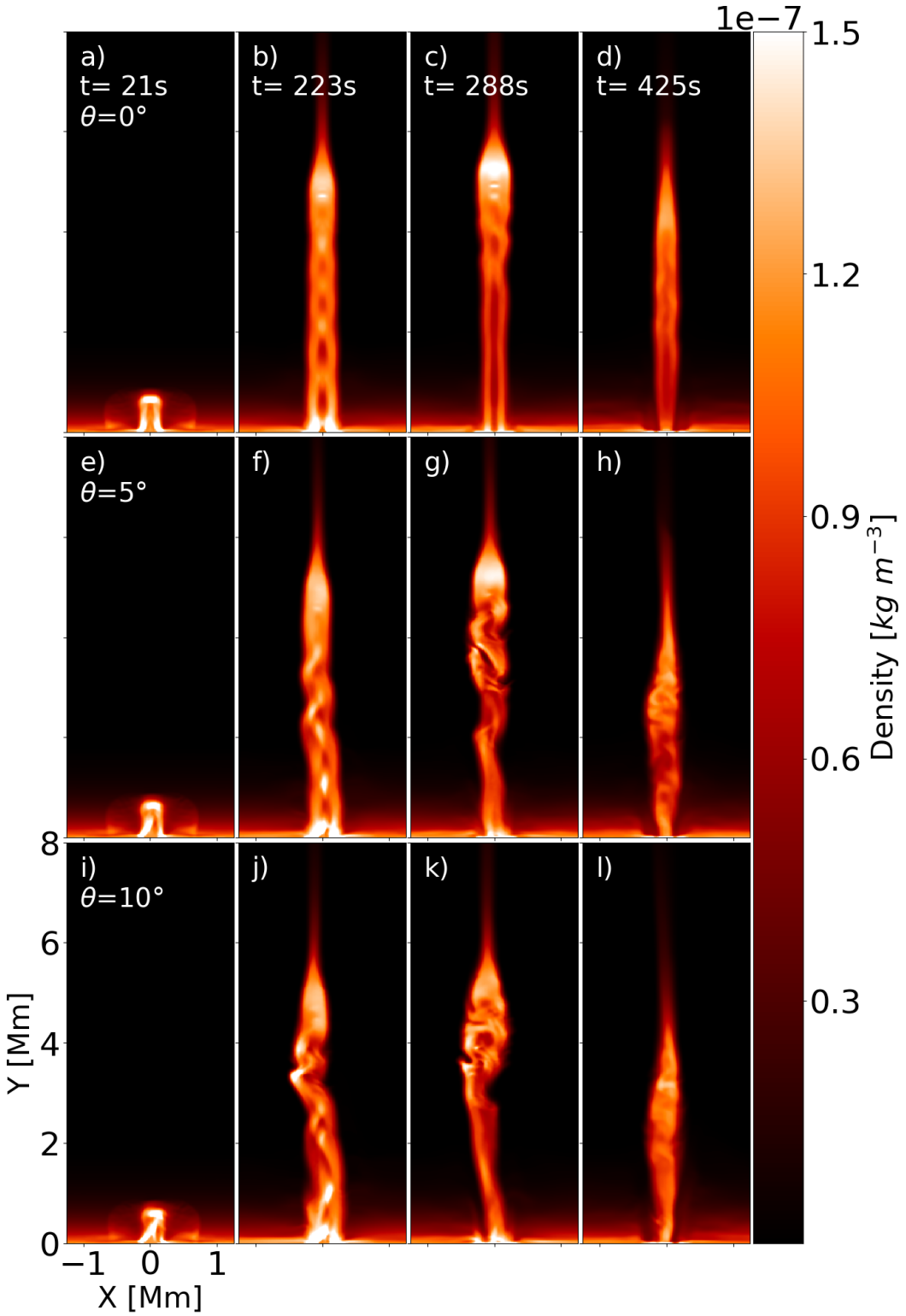

Figure 4.11: Example of the temporal evolution of different tilt angles for jets from 0, 5, 10° from top to bottom. Animation available where cases a, e, i are in the top row: https://etheses.whiterose.ac.uk/30244/5/fig_4.11___4.12.avi

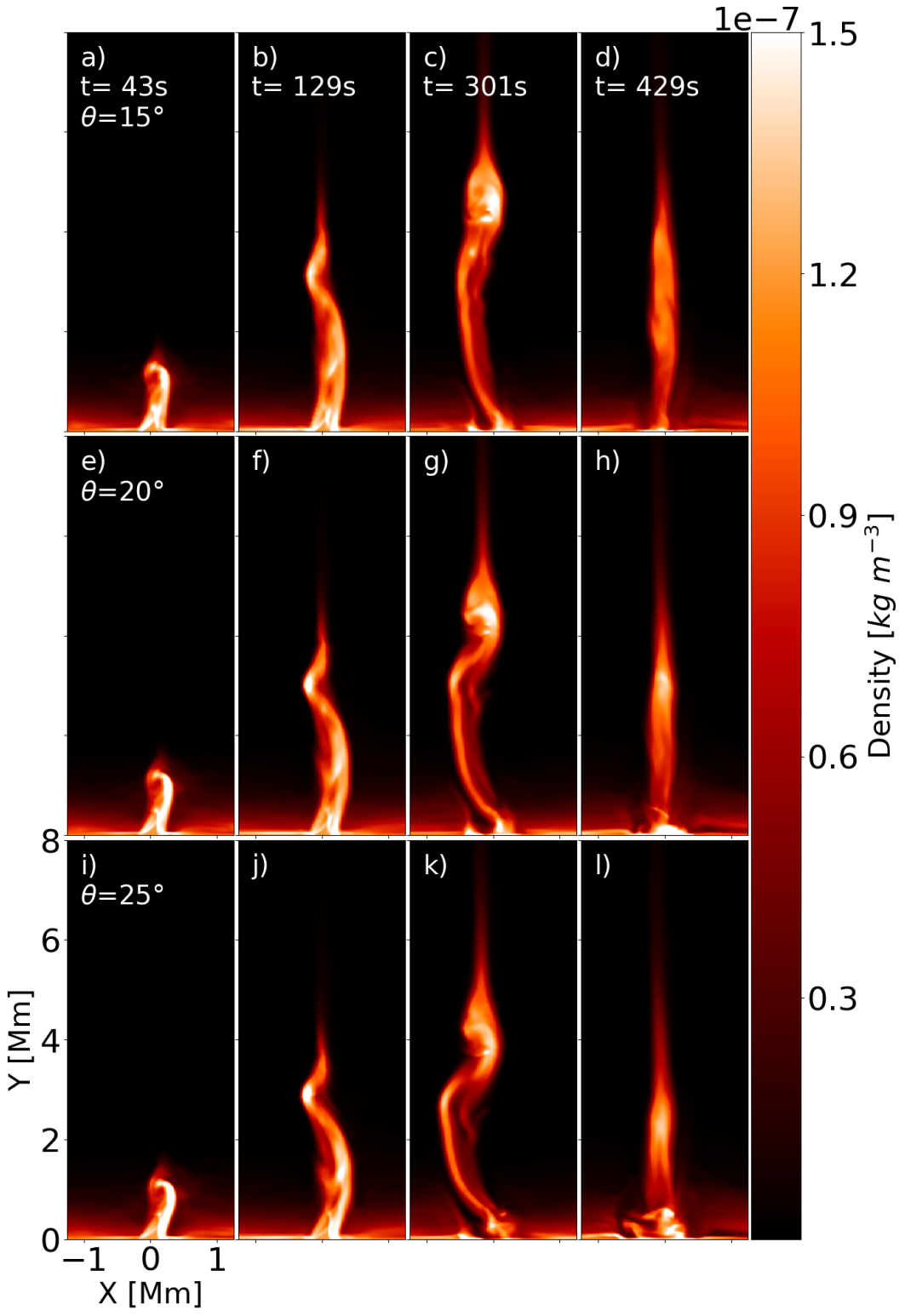

Figure 4.12: Example of the temporal evolution of different tilt angles for jets from 15, 20, 25° from top to bottom. Animation available where cases a, e, i are in the bottom row: https://etheses.whiterose.ac.uk/30244/5/fig_4.11___4.12.avi

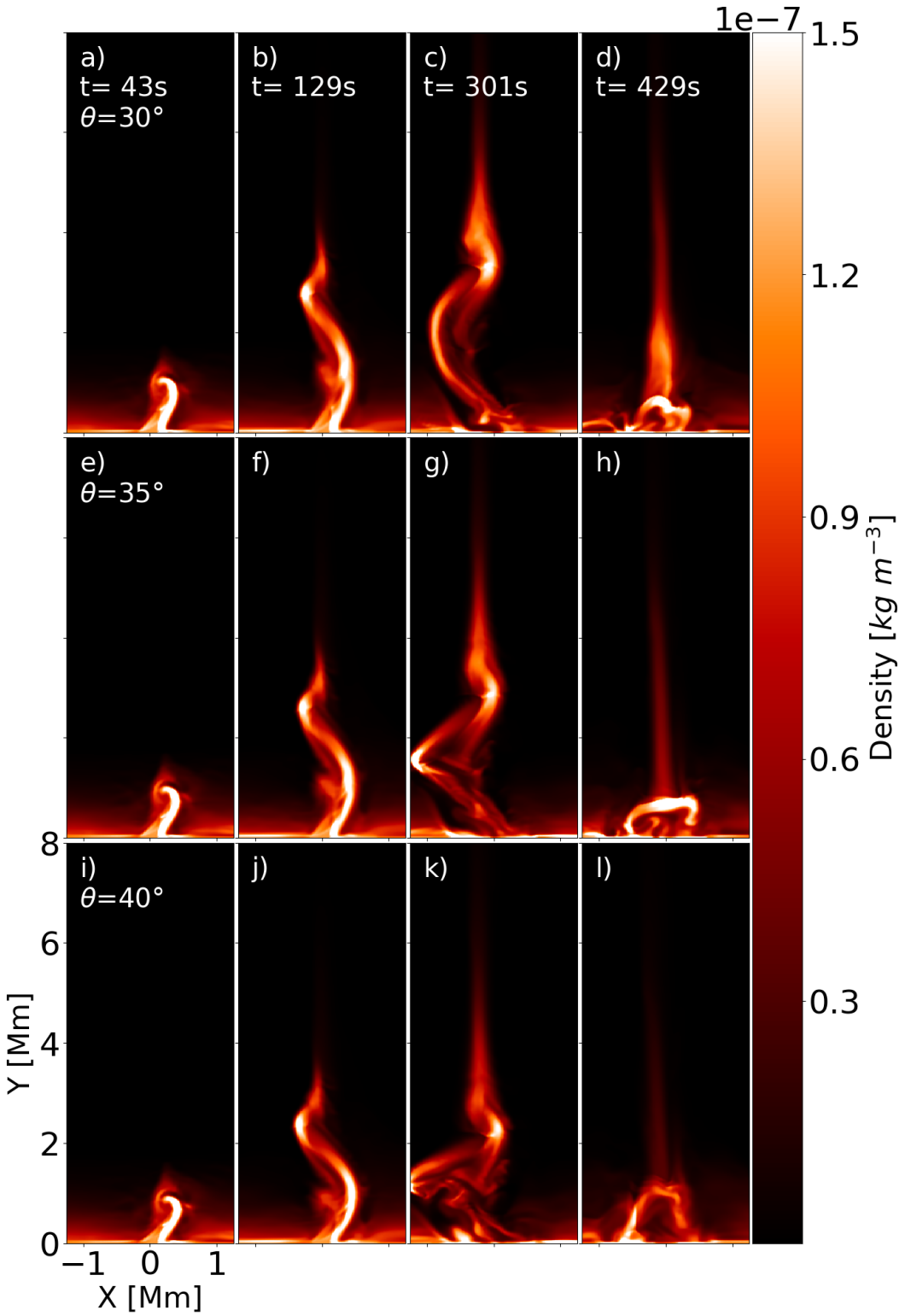

Figure 4.13: Example of the temporal evolution of different tilt angles for jets from 30, 35, 40° from top to bottom. Animation available where cases a, e, i are in the top row: https://etheses.whiterose.ac.uk/30244/6/fig_4.13___fig_4.14.avi

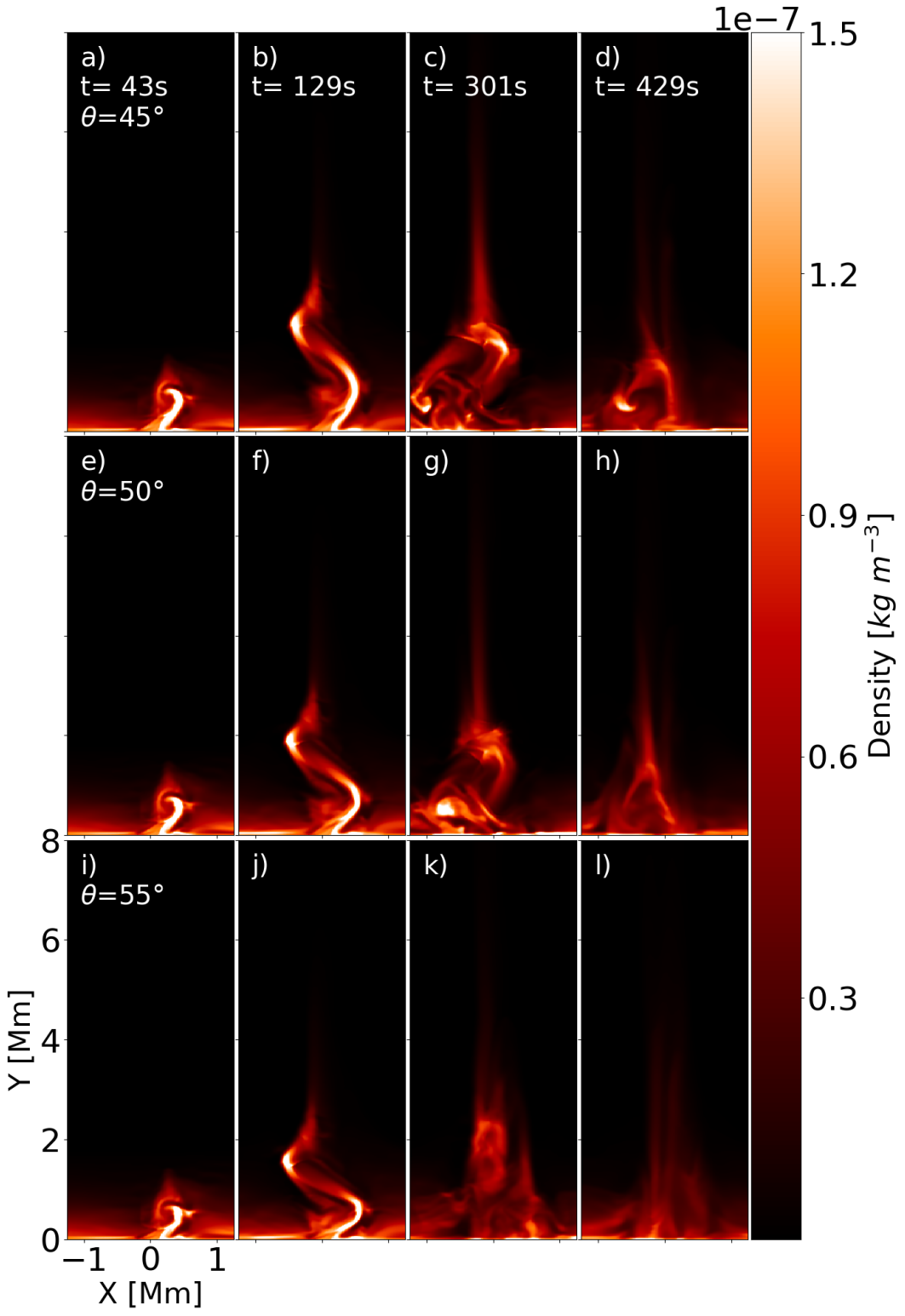

Figure 4.14: Example of the temporal evolution of different tilt angles for jets from 45, 50, 55° from top to bottom. Animation available where cases a, e, i are in the bottom row: https://etheses.whiterose.ac.uk/30244/6/fig_4.13___fig_4.14.avi

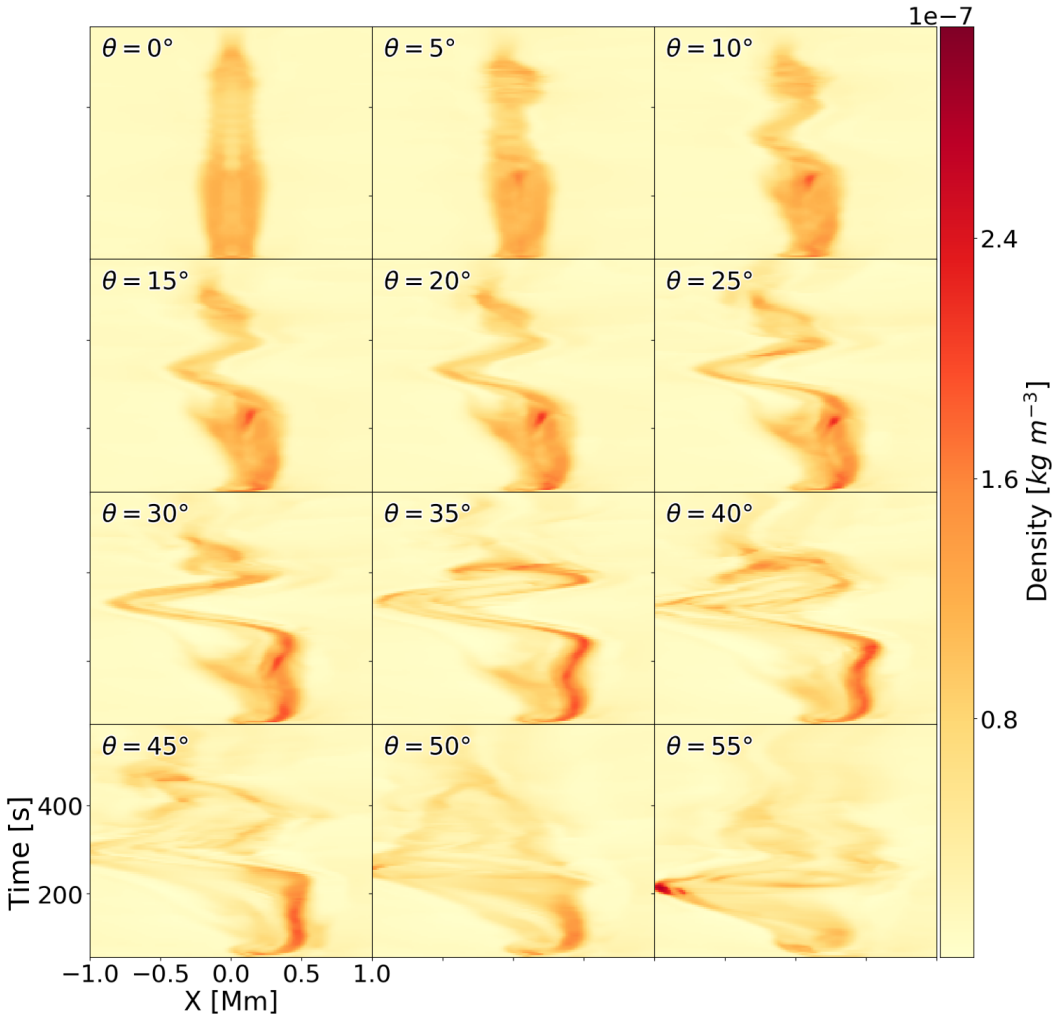

Figure 4.15: Time distant plot with horizontal slit at 1 Mm for tilt values $0 - 55°$.

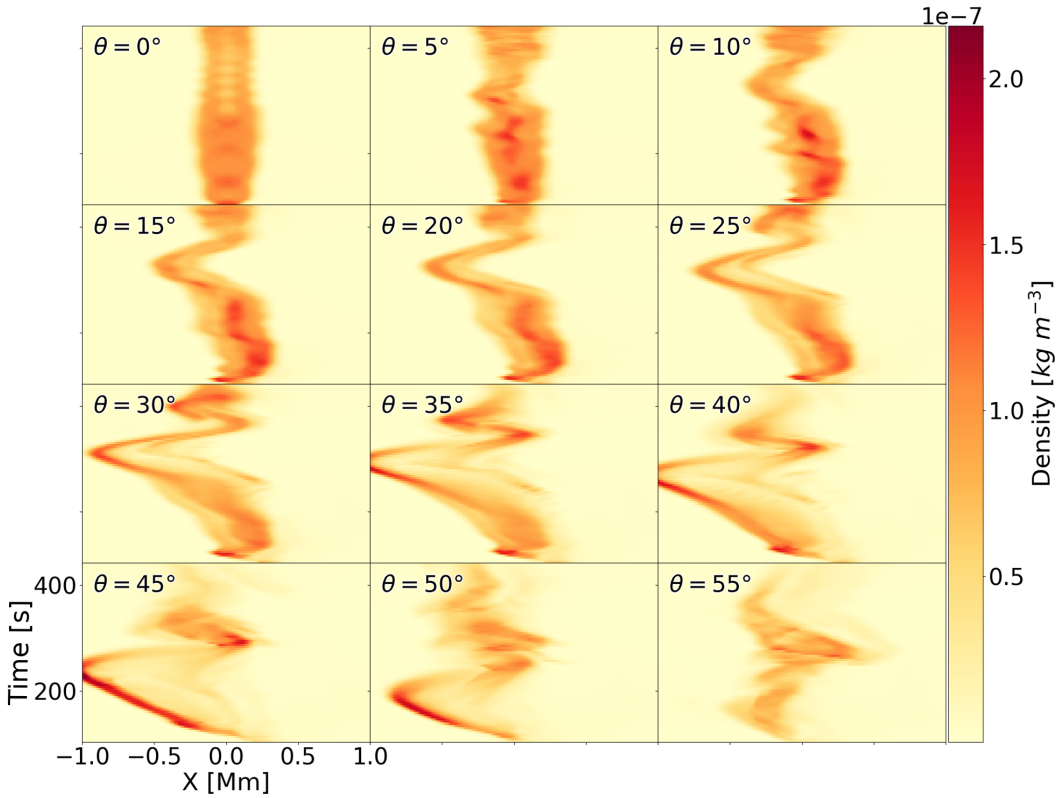

Figure 4.16: Same as fig. 4.15, but at 2 Mm.

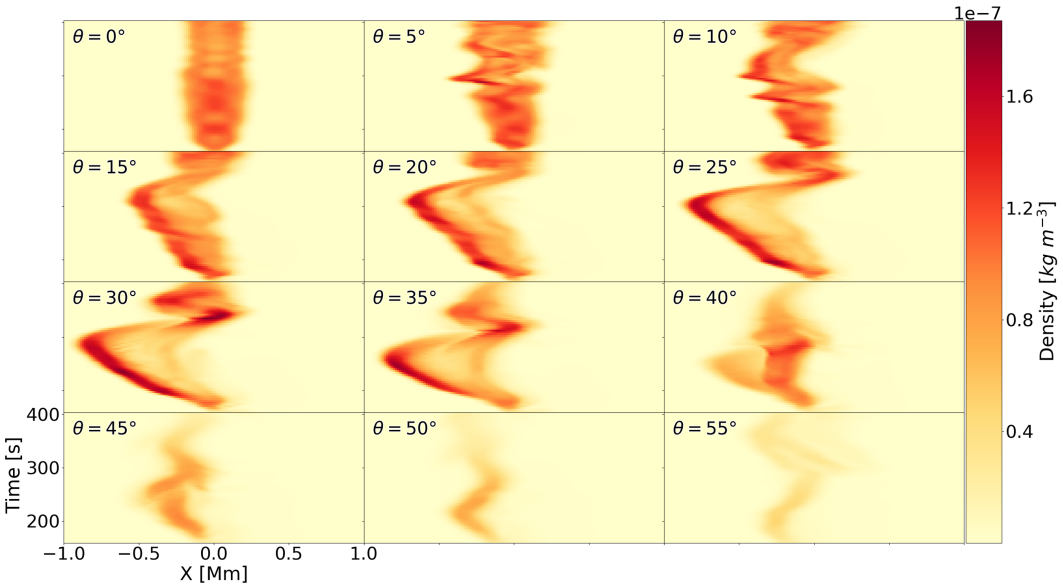

Figure 4.17: Same as fig. 4.15, but at 3 Mm.

4.4 Summary and Discussion

In summary, the model used in Chapter 3 has been generalised to produce non field-aligned flows to study its effect on jet heights, widths and density evolution. A simple approach is taken to capture the basic dynamics of the jet across two focused parameter scans. The main results obtained from this Chapter are:

- Over the range of the parameter space studied, the tilt led to a reduction in apex height and length of the jet.
- Knots may be more challenging to observe in solar jets than first proposed in this thesis. Even with small amounts of tilt the clear structure seen in straight jets becomes deformed and more blended into the jet beam. At high inclination angles, it would be unlikely that knots would be observed.
- The whip motion in the jet is probably due to DKI, but more analysis of the simulations is required to confirm this. The assumptions and physical set up (e.g. different form of stratification of atmosphere, geometry, and magnetic field configuration) that are used to derive the dispersion relation in Zaqarashvili (2020) are not directly applicable to the synthetic jet. A new dispersion relation would need to be derived and the wave frequency inside the jet would need to be calculated to determine the point at which the onset of DKI occurs.
- By introducing tilt into the jets, they not only undergo CSW variations but also transverse motions. These are two key dynamical ingredients that need to be captured in spicular models. For small tilting angles ($< 10°$) there is a combination of both CSW and transverse displacement, but for larger tilts the transverse motion dominates.

An important result of these simulations is that even a slight misalignment between flow and magnetic field produces noticeable transversal displacement and has major effects on the morphology. The first evidence of transverse motion in spicules was identified by Pasachoff et al. (1968). The mechanism by which transverse motion arises remains a subject of debate. Several mechanisms have been suggested, including overshooting of convective motions in the photosphere, granular buffeting, rebound shocks, global p-mode oscillations, and reconnection near foot point (Roberts, 1979; Sterling and Hollweg, 1988;

Vranjes et al., 2008; Jess et al., 2012; Ebadi and Ghiassi, 2014). The interpretation of the bulk motion of spicules has typically been through the framework of MHD waves. Many studies report the transverse motion of spicules are due to MHD kink waves (Kukhianidze et al., 2006; De Pontieu et al., 2007c; Jess et al., 2012; Ebadi and Ghiassi, 2014; Tavabi et al., 2015; Jafarzadeh et al., 2017). The increased interest is due to the spicules' potential to transport the energy contained in these waves throughout the lower atmosphere (De Pontieu et al., 2007c; He et al., 2009b; Morton et al., 2012b; Jess et al., 2012). These transverse motions are clearly an important ingredient in the dynamics of spicules and potentially in maintaining the hot solar atmosphere. Non-field aligned flow gives another mechanism to produce transverse motions. This simple mechanism is likely to occur due to the conditions of the chromosphere (where the flow will not always be aligned with the magnetic field), and the complexity of the Sun's magnetic field. Regardless of the tilt angle, the synthetic jets undergo $1-2$ sways of transverse motion, which are larger with increasing tilt angles. Even with simple models of jets, this highlights the complexity of the dynamics. Understanding how a common component of tilt affects the appearance of the jet is a key part of interpreting the dynamics of spicules, and this should be a factor included in any model of spicules.

CHAPTER 5

Comparing Synthetic Jets to Observations

5.1 Introduction

In this Chapter, the aim is to investigate the cross-sectional width behaviour of straight jets and compare them with observations of Hα spicules. Observations indicate that spicules generally emanate near the inter-granulation lanes and remain subject to MHD stresses at their footpoint. The associated motions, irrespective of whether turbulent or coherent, become channelled through the spicule structure and are reflected in their observed dynamic behaviour. Broadly, spicule kinematics can be categorized into three major domains: radially transverse, field-aligned, and torsional. These have been extensively examined and interpreted in terms of discrete MHD wave modes (see review: Zaqarashvili and Erdélyi, 2009).

Since the discovery of standing kink oscillations that cause transverse displacement in solar structures (Aschwanden et al., 1999; Nakariakov et al., 1999; Aschwanden et al., 2002), and MHD waves in solar structures have gained much attention (Cally, 1985; Kudoh and Shibata, 1999; Fujimura and Tsuneta, 2009; Zaqarashvili and Erdélyi, 2009; Kuridze et al., 2012; Jess et al., 2012; Mooroogen et al., 2017; Allcock et al., 2019). This is due to their potential to provide estimates that we can not directly measure in solar structures (e.g. magnetic field strength), and because they are thought to carry sufficient energy to heat the corona (Alfvén, 1947; Gordon and Hollweg, 1983; Poedts, 2002; Srivastava et al., 2017). The first report of kink waves in spicules was by Kukhianidze et al. (2006), and numerous studies have since followed, with the

This chapter is based on the following refereed journal article:

Dover, F., Sharma, R., Korsós, M., Erdélyi, R., (2020); Signatures of Cross-sectional Width Modulation in Solar Spicules due to Field-aligned Flows, *Astrophys. J.*, Volume 905, Issue 1, https://doi.org/10.3847/1538-4357/abc349

goal of identification and study of transverse (kink and torsional Alfvén) wave modes (De Pontieu et al., 2007c; Ebadi and Ghiassi, 2014; Pascoe et al., 2016; Sharma et al., 2017; Tiwari et al., 2019). However, reports of CSW variations have remained elusive, due to current resolution limits for observations of jet-like chromospheric features. The presence of CSW variations in thin MFT structures, as a possible consequence of $m = 0$ MHD sausage and/or $m = 2$ fluting modes, was postulated in earlier theoretical studies (Ziegler and Ulmschneider, 1997b,a; Ruderman et al., 2010). Observations that report on CSW variations in spicular structures are limited to on-disk fibrils, where concurrent transverse and CSW were reported as coupled kink and sausage modes by Jess et al. (2012) and Morton et al. (2012a). Similar observations for CSW, and intensity oscillations in on-disk slender chromospheric fibrils were reported by Gafeira et al. (2017a) and interpreted as MHD sausage wave modes. Moreover, an ensemble of coupled transverse, CSW and axisymmetric torsional motions were reported in off-limb spicules by Sharma et al. (2018), which were interpreted as nonlinear kink modes.

Spicules are essentially jet-like features where mass flows along their magnetic field with velocities in the range of $25 - 100$ km s^{-1} (Beckers, 1972; Sterling, 2000; Pereira et al., 2012). These velocities may even have a dominant effect on the waves that are present in spicular jets. Plasma flows will interact with the oscillatory modes of spicules, e.g. periodic motions along or anti-parallel to the bulk motion will be affected differently. Wave motions in steady waveguides have been investigated in the past in a few theoretical studies for different slab and cylindrical geometries (Narayanan, 1991; Nakariakov and Roberts, 1995; Terra-Homem et al., 2003; Soler et al., 2008). It was concluded that mass flows can generate a shift in frequencies for confined MHD waves and can influence the wave propagation, even causing resonant flow instabilities, depending upon the direction and strength of mass flows. Though possible effects of mass flow on wave periodicities/propagation are known theoretically, they are yet to be observed in highly localised dynamic waveguides such as solar spicules.

At multiple points through this thesis, there has been a comparison between the simulations and observations. Interesting features that have arisen in the synthetic jets, particularly the CSW variations and the knots. In this Chapter, we aim to focus on these aspects of the observations by comparing the CSW variations in off-limb spicules with the observed dynamical behaviour

with synthetic jets, and highlight observed solar features where knots may be present.

5.2 Cross-sectional Width Variation in Synthetic jets

The synthetic jets studied in the thesis capture some of the fundamental dynamics of a chromospheric jet in a stratified atmosphere. Though the momentum-driven simulated jet lacks a few observed complex physical mechanisms, e.g. radiative losses, ambipolar diffusion, and ion-neutral effects, it still models crucial kinematic behaviour, such as longitudinal/field-aligned plasma motions with CSW variations (Fig. 5.1) in both rising and falling phases of the jet evolution.

Using the jet tracking code as outlined in Chapter 3 the CSW have been measured for a jet with parameters of $\theta = 0°$, $P = 300$ s, $B = 50$ G, and $A = 60$ km s^{-1} (see Fig. 5.1). The parameters of these jets are similar to those of the standard jet, and hence display similar dynamics, morphology, lifetimes, knots, and CSW variations. The jets' widths are temporally tracked at multiple heights, where the blue marks measure the widths and yellow triangle locked onto the apex of the jet. The results of the widths for each megameter the jet reaches in the computational domain are displayed in Fig. 5.2, which also demonstrates that there are oscillatory patterns at each height, except from at 6 Mm. Oscillatory motion is not seen at 6 Mm due to lack of time which the synthetic jet spends at this height.

We decided to focus on slit height at 2 Mm as it can be compared against observations, and because choosing a lower height gives more temporal data to analyse than higher slits. The life of a jet can be separated into two phases; the rising phase, where the jet is being driven and is propagating upward, and the fall phase where the jet is no longer being driven and apex height is decreasing with time. These regions are separated by using the parabolic trajectory and calculating the point at which the gradient switched from positive to negative, i.e. the apex of the trajectory, which is marked temporally by the solid black vertical line in Fig. 5.3. One striking feature is seen in Fig. 5.3; to the best of our knowledge we are the first to discover that there are distinct differences in the behaviour of the boundary deformation for the rising (green

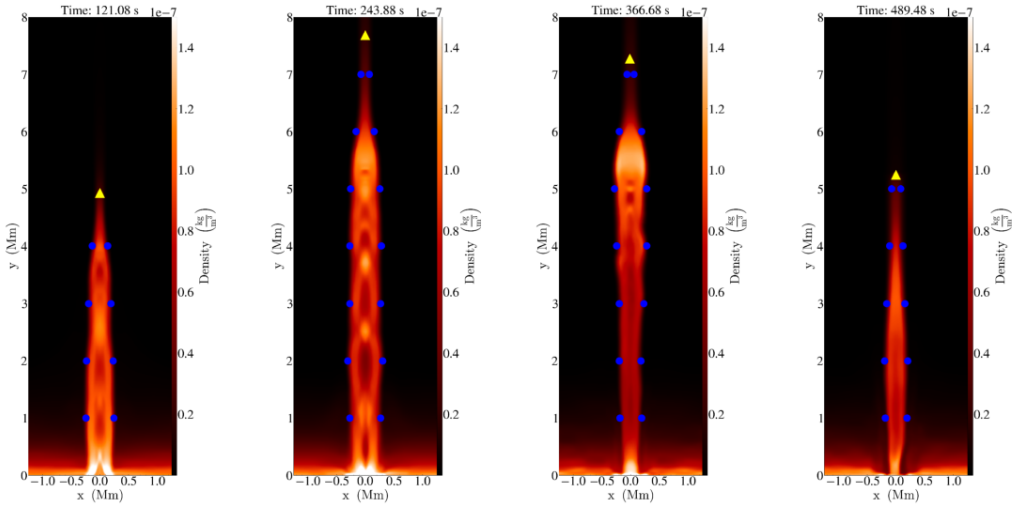

Figure 5.1: Panels showing the temporal evolution of the simulated spicule density structure at four time-steps with apex marked by a yellow triangle. From $121.08 - 243.88$ s ($366.68 - 489.48$ s) the rising (falling) phase. Locations of tracers edges are also shown as blue dots, which are used to estimate the variations in CSW during rising and falling phases of jet structure.

line) and falling (cyan line) phases of the jet. During the rising phase, the CSW is larger and with only a few undulations, whereas in the fall phase the CSW are shorter and faster undulations. The blue and orange lines show the quadratic fit used to detrend the rise and fall phases respectively in Section 5.4.

It is possible to observe width variations of multiple solar structures as highlighted in observational studies, e.g. for fibrils (Morton et al., 2012a), coronal loops (Aschwanden and Schrijver, 2011), EUV jets (Zhang and Ji, 2014; Chen et al., 2022), and spicules (Sharma et al., 2018). Currently, there are not many studies that have temporally investigate the width variations of spicules, but I believe this will change with the planned advancements in telescopes and better spatial resolution they will provide, such as DKIST. This motivated us to provide an early study that point in direction of potential discoveries to made in the investigation of CSW of spicules.

5.3 Observations of Cross-sectional Width Variation in Spicules

In Section 3.4 we have discussed that SST currently offers one of the highest spatial resolution observations of the chromosphere, making it an ideal telescope to use for tracking the widths of such small features as spicules. SST

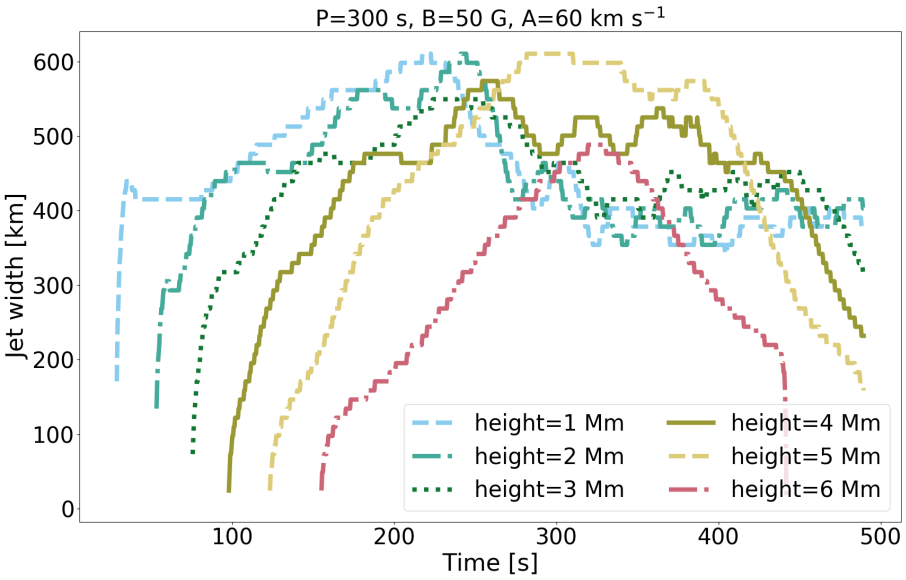

Figure 5.2: CSW variations over multiple heights for synthetic jet with $P = 300$ s, $B = 50$ G and $A = 60$ km s^{-1}.

is a ground-based telescope located in La Palma, which has one of the best seeing conditions in the world, placed 2400 m above sea level. It has a nearly 1 m sized aperture and uses active optics to minimise data degradation due to Earth's atmospheric conditions. The data captured in this section uses the CRisp Imaging SpectroPolarimeter (CRISP), which covers a wavelength range of 510 to 860 nm, with a field of view of approximately 43.5 × 43.5 Mm, and a pixel size of roughly 43 km. The spectral line selected for observation is Hα (656.3 nm), giving an angular resolution of approximately 95 km. Hα can only form in the light spectrum from regions of the Sun that are cool enough for hydrogen to exist in its atomic form, which are the photosphere and chromosphere. It is part of the Balmer series and forms absorption or emission spectra for hydrogen when the electron jumps from or falls to $N = 2$, where N is the electron orbital number. The Hα line is commonly used for observing chromospheric structures as it reveals many complex structure in the messy chromosphere (Parmenter, 1966; von Uexkuell et al., 1985; Nishikawa, 1988; Judge, 2006; Leenaarts et al., 2007; Rutten, 2008; Jess et al., 2012; Pereira et al., 2016; Rutten, 2017).

The spicules' structures presented in Figs. 5.4, 5.6 and 5.7 were identified in observations carried out on AR NOAA AR11504 at 07:15-07:48 UT, June 21, 2012. The identification of the spicules and data processing of these ob-

servations was carried out in collaboration with Dr. Sharma; we will outline the steps taken. The AR was scanned using 31 equally spaced line positions with 86 mÅ steps from −1.376 to +1.29 Å, relative to the line centre, along with the additional 4 positions in the far blue wing from −1.376 to +2.064 Å. Following data acquisition, post-processing of data was carried out using the Multi-Object Multi-Frame Blind Deconvolution (MOMFBD; van Noort et al., 2005) image restoration algorithm. Also, standard procedures available in the image pipeline for CRISP data were implemented (de la Cruz Rodríguez et al., 2015), including differential stretching and removal of dark and flat fielding.

The processed data spans around 30 mins and a cadence of 7.7 s. Following the Nyquist criterion, the temporal-resolution of the dataset allowed the detection of MHD wave modes with periodicities over 15.4 s. Three spicules (SP:A, SP:B, and SP:C) were selected as they needed to be a high-intensity structure with the least possible superimposition by any other surrounding features during their visible lifetime in an observed passband. The identified spicules have an average lifetime of 118 ± 17.88 s measured from the Hα line-centre. It is possible their true lifetime is longer, as spicules tend to change temperature during their evolution and therefore evolve through multiple passbands, which measurements by Pereira et al. (2014) have shown to have lifetimes in the range of $500-800$ s. The observed features have an average length of about 3 ± 0.36 Mm with apices reaching up to an average height of 4.83 Mm.

The CSW of observed spicule features were estimated using the method adopted from Sharma et al. (2018). A single Gaussian function with linear background is used to fit the intensity profile across the observed spicules and the FWHM is taken as a measure of CSW of the feature. For the selected spicules, the average FWHM of the spicules measured at 2 Mm is 144.47 km, which is comparable with other observations for off-limb spicules (Sharma et al., 2018). The spicules are resolved as there is a 3.36 (1.52) pixel (angular-resolution) cover, bearing in mind that the intensity values belonging to the spicule will occupy a space larger than the FWHM. This process is outlined in Fig. 5.4, where panels a1-a4 shows snapshots of the identified spicule where the cyan line is the vertical slit to track field-aligned plasma motions and horizontal yellow slit is placed at 2 Mm to track the CSW. Panel (b) displays time-distance data captured with across the vertical slits, which are used to estimate the speed of the spicules and allow for the separation of the rise

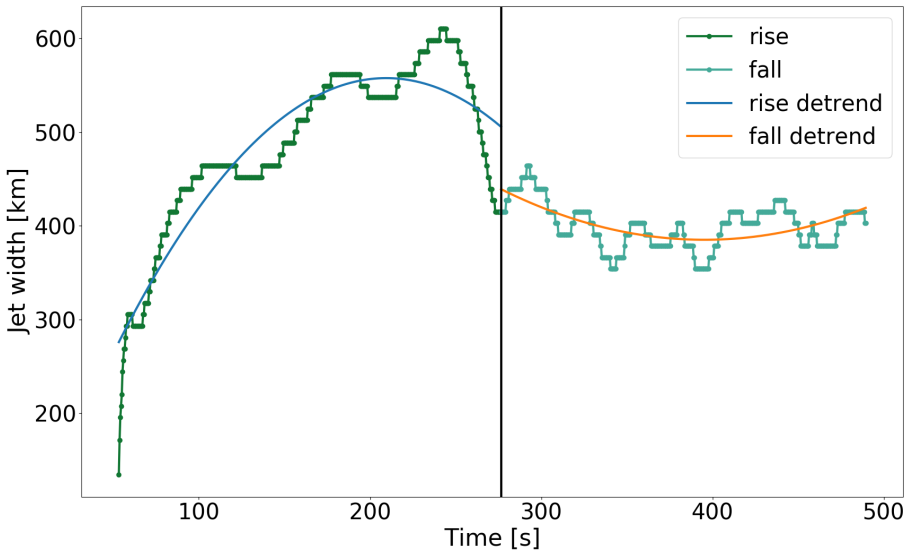

Figure 5.3: CSW variation for slit at 2 Mm. The solid vertical black line separates the rise (green line) and fall (cyan line) phases, located at the time where the jet reaches its apex. The blue and orange lines are a quadratic fit used to detrend the data.

and fall phases. Panel (c) shows the process of calculating the FWHM of the spicule, where the dark (light) shaded region marks the unperturbed (perturbed) width W_u (W) during the spicule lifetime measure by the yellow slit. The unperturbed width is fixed individually for each spicule as the average FWHM calculated over its lifetime, and the perturbed width is the FWHM calculated at each time step of the observations. The temporal variations in CSW are calculated with $\delta W = W(t) - W_u$ and were used to estimate the periodicities.

SP:A in Fig. 5.4 is an off-limb spicule that was observed at -1.032 Å from the Hα line core with a total lifetime of around 161.7 s. The feature had a physical length of 3.8 Mm at an inclination of 21.4° over the observed limb, with apex height reaching a maximum of 5.3 Mm. The longitudinal motions in the Lagrangian frame were analysed to estimate the velocity and duration of rising and falling phases, using a vertical slit (Fig. 5.4 a1–a4) along the axis of spicule structure. The time-distance analysis of the vertical slit suggests a parabolic profile (Fig. 5.4(b)) of mass motions with an average ascending velocity of $\sim$46.9 km/s. The plasma attains the maximum height in about 81 s and then falls back to the surface with an average velocity of 40.2 km/s. For

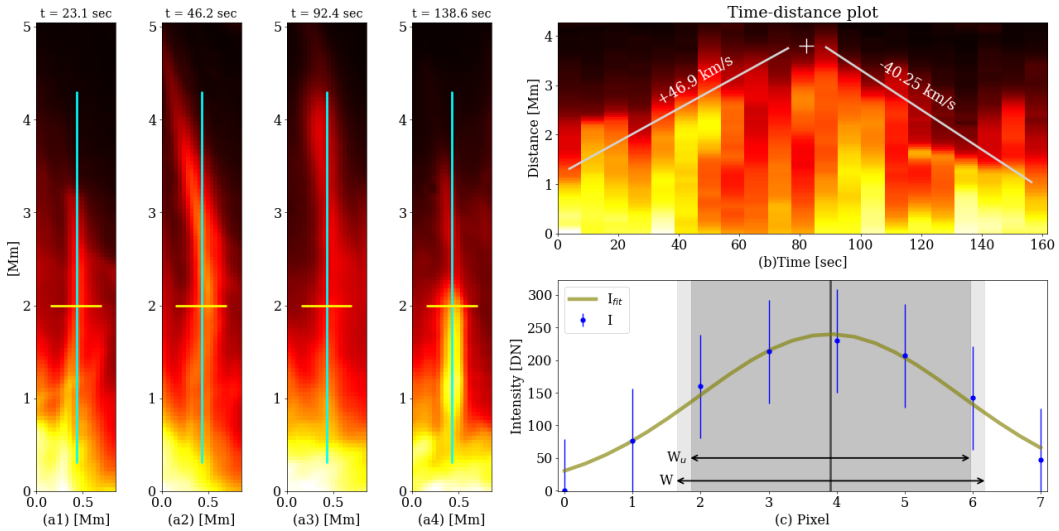

Figure 5.4: Panels (a1) – (a4) show the temporal evolution of candidate spicule feature (SP:A) in the Hα passband at four instances, with positions of vertical (cyan) and horizontal (yellow) slits used for the estimation of field-aligned mass flows and CSW respectively. Panel (b) shows the time-distance plot from the vertical slit on the spicule, highlighting the rise- and fall-phases of field-aligned mass flow. The maximum height attained by the visible plasma is marked with the '+' symbol, along with estimated velocities (46.9 km/s, 40.25 km/s). Bottom panel (c) shows an example of Gaussian fit for intensity magnitudes for horizontal slit location (marked as a yellow line on (a1) – (a4)), with error bars, denoting the standard deviation for intensity values. The vertical black line marks the position of the amplitude of Gaussian fit, while shaded-regions mark average/unperturbed width (W_u) during spicule lifetime and perturbed/instantaneous width (W). This figure is taken from Dover et al. (2020) and was produced by Dr. Sharma.

the observed lifetime, the average/unperturbed CSW estimate (W_u) for the spicule structure was around 176 km.

5.4 Comparison of Cross-sectional Width Variation in Synthetic Jets and Spicules

The CSW estimates from both observation and synthetic jets indicate an oscillatory pattern during the feature's lifetime. These were further analysed using wavelet transform to understand the nature of periodicities and associated wave physics. The results obtained from this analysis is viewed in the framework of ideal MHD waves, as this is likely how this phenomenon would be interpreted in observations. To identify any significant periodicities, wavelet power spectra (WPS) and the associated global power spectrum (GPS) are constructed using open-source software developed by Torrence and Compo (1998). The default Morlet wavelet profile was employed with a two-σ confidence level on CSW estimates from observations (top panels) and synthetic jet (bottom panels) as shown in Fig. 5.5. The wavelet analysis is applied to both the rising and falling phases, as well the full signal. For the synthetic jets, the rise and fall phases are independently detrended with a quadratic polynomial (see Fig 5.3). A low order polynomial is chosen to avoid over fitting. In addition, the detrended data are smoothed to reduce noise with a moving average with a window size of 15 and 10 for the rising and falling phases, respectively.

The peak frequencies were identified in the wavelet analysis as spectral magnitudes in WPS with significance levels over unity and higher, highlighted as black contours in Fig. 5.5. The peaks also had GPS over two-σ (95%) confidence levels (orange dashed-line in Fig. 5.5). The wavelet spectra for observed width variations during spicule lifetime suggest a strong spectral density concentration around 17 s for 5 cycles. Interestingly, for the simulated jet structure, the WPS indicates the presence of harmonics concentrated around 65 s and 32 s for 8 and 5 cycles, respectively. The oscillatory behaviour between the rising and falling phase is displayed in the last two columns, respectively It becomes clear with the wavelet analysis that there are remarkable differences in the periodicities of the falling and rising phases for each example (see periodicities in Table 5.1 and Figs. 5.5 to 5.7). This modulation of frequency could be tied to the change in direction of flow and its relation to gravity from rising (working against gravity) and falling phases (working with gravity).

Wavelet transforms for observational width variations indicate approximately 27 s periodicity for 3 cycles, while a powerful 70 s periodicity is present in both GPS and WPS of the simulation data. However, there is a noticeable shift towards lower/higher periodicities/frequencies for two out of three of our identified spicule cases (Table 5.1) during the fall-phase of the plasma flows in the jet structure. The wavelet spectrum for observed width variations shows dominant periodicity at 16 s for 5 cycles, while for simulated data there are two strong periods concentrated around 30 s and 68 s, each persistent for 5 and 2.5 cycles. These results are consistent with previous reports for CSW oscillations in on-disk fibrils (Gafeira et al., 2017a).

An important aspect of our investigation is the confirmation of the first overtone in cross-sectional width periodicities associated with dynamic waveguides in the solar chromosphere. Earlier studies were able to only identify higher harmonics in static waveguides (e.g., in a coronal loop), with the presence of fundamental and first overtone (Verwichte et al., 2004; Guo et al., 2015). Recently, the presence of a second overtone was also reported for coronal loop observations by Duckenfield et al. (2019), associated with transverse kink oscillations. It must be noted that wave harmonics can provide vital clues regarding plasma and magnetic field characteristics of the waveguide via solar magneto-seismology applications (Andries et al., 2005, 2009). The presence of overtones in jets provides a key tool for chromospheric magneto-seismology. This phenomenon is not limited to this one observation, as shown in Fig. 5.6 and Fig. 5.7. For a summary of the results and physical properties of all the selected spicules see Table 5.1.

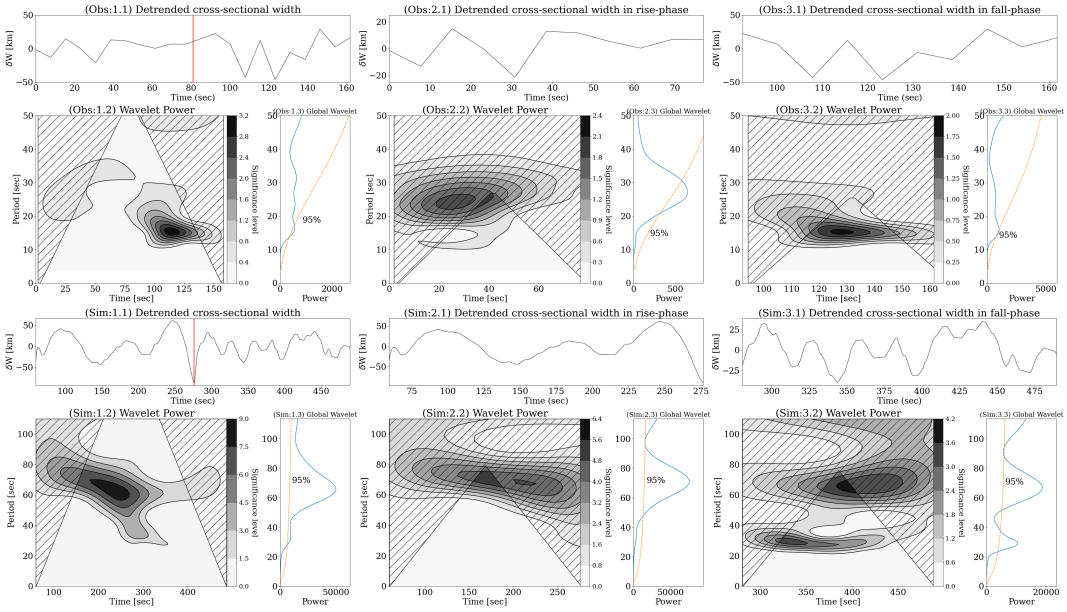

Figure 5.5: Panels showing the results of spectral analysis of cross-sectional width estimates of observed (top) and simulated (bottom) jet structures. Each panel depicts temporal evolution of overall widths (1.1) and subsequent rise- (2.1) and fall-phases (3.1), along with Wavelet Power Spectra (WPS: 1.2, 2.2, 3.2) and Global Power Spectra (GPS: 1.3, 2.3, 3.3) during each phase of the evolution of the jet. Vertical red line in plots (Obs: 1.1 and Sim 1.1) marks the time when the field-aligned plasma attained the apex height. Further, plots (Obs: 1.1, Sim: 3.2) provide clear indication of a second harmonic of the cross-sectional width deformations in the dynamic spicular waveguide. This figure is taken from Dover et al. (2020) and produced by Dr. Korsós and Dr. Sharma.

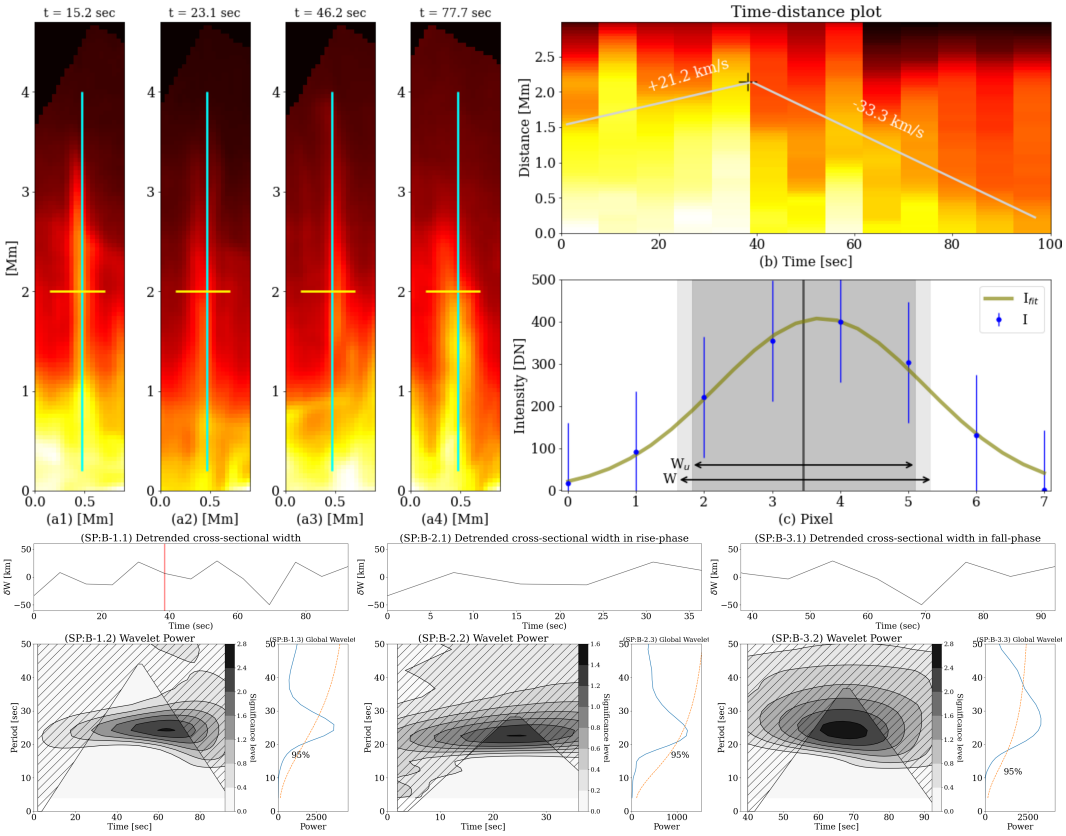

Figure 5.6: Details of spicule SP:B are shown, where panels (a-c) show the same analysis carried out as for Fig. 5.4, and the bottom 2 panels show the corresponding wavelet analysis as done in Fig. 5.5. This figure is taken from Dover et al. (2020) and was created by Dr. Sharma.

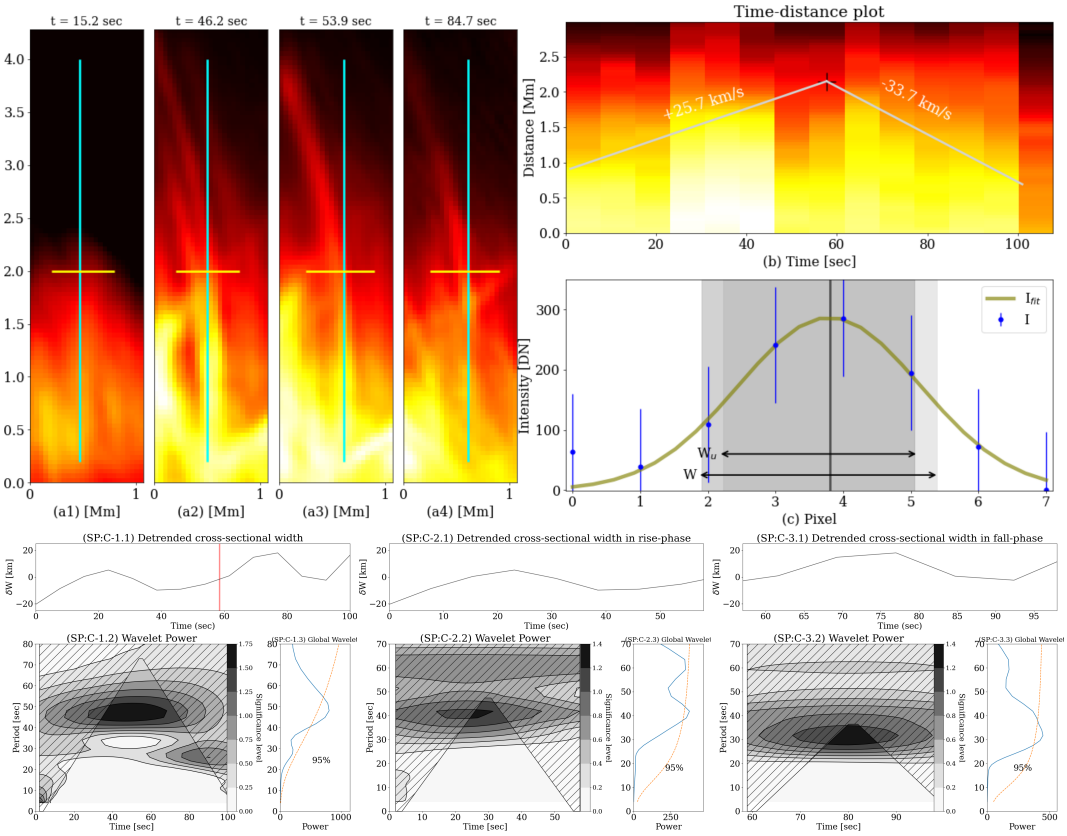

Figure 5.7: Same as Fig. 5.6, but for spicule SP:C, where panels (a-c) show the same analysis carried out as for Fig. 5.4 and the bottom 2 panels show the corresponding wavelet analysis, as done in Fig. 5.5. This figure is taken from Dover et al. (2020) and made by Dr. Sharma.

Table 5.1: Summary of observed physical characteristics of candidate spicule structures along with estimated periodicities during rising, falling and overall phases. Physical and spectral parameters of the synthetic jet structure are also provided for a comparison between observed and simulated case(s).

Spicule	Lifetime	Length	Apex-height	Unperturbed Width	Periodicity (s)		
	(sec)	(Mm)	(Mm)	(km)	Rising phase	Falling phase	Overall
SP:A	161.7	3.8	5.3	176.0	27.0	16.0	17.0
SP:B	92.4	2.2	4.8	134.6	22.5	27.4	24.7
SP:C	100.1	2.8	4.4	122.8	41.2	31.3	48.8
Simulated jet	489.48	8.0	8.0	187.5	70.0	30.0 & 68.0	32.0 & 65.0

5.5 Blobs in Solar Jet Observations

Observing knot structures is challenging due to the current resolution limits, as stated throughout the thesis. However, larger-scale jets occur on the Sun, and if the flow speed is sufficient then it is possible that patterns of the knots may be observed. In a series of studies on coronal jets blobs structures were observed (Zhang and Ji, 2014; Zhang et al., 2016; Chen et al., 2015, 2017).

Zhang et al. (2016) show multiple observations of blob structures in solar jets. The observations were captured by Extreme-Ultraviolet Imager (EUVI) in the Sun-Earth Connection Coronal and Heliospheric Investigation (SECCHI) (Howard et al., 2008) instruments of the Solar TErrestrial RElations Observatory (STEREO) (Kaiser, 2005) and SDO, using the AIA instrument (Lemen et al., 2012). The images in Fig. 5.8 were observed with STEREO-B in 171 $\AA$ filter with a spatial resolution of approximately 2320 km (3.2″) and a cadence of 75 s. Two jets (J1 and J2) originate around a coronal bright point (BP1). These are thought to arise due to magnetic reconnection (Priest et al., 1994; Mandrini et al., 1996; Longcope, 1998; Santos and Büchner, 2007), and the jets flow along closed magnetic loops. J2 is particularly interesting as multiple blobs form along with the jet, which is highlighted by the white arrows in panels (f-g). Magnetic reconnection is the process of breaking and reconnection of magnetic field lines with opposite polarities in a plasma. This process results in the magnetic field energy being converted into kinetic and thermal energy. The energy released in these events is proposed to drive solar jets. If a jet is driven by magnetic reconnection then one possible mechanism for knots formation in the jet beam is the tearing mode instability (Furth et al., 1963). These arise as plasmas carrying oppositely directed magnetic field lines are brought together, a strong current sheet forms between them. If this current sheet is extremely thin a small perturbation to this system can cause it to go unstable and trigger the tearing mode instability which forms plasmoids due to magnetic islands (Drake et al., 2006). This would appear as bright blobs of plasma. Numerous plasmoids would form due to tearing mode instability and appear as knots as they would be ejected away from the location of reconnection and travel along the jet beam causing the change of density distribution along the jet. This process for EUV jets is outline in Fig. (5.10) panels A-C. These plasmoids are proposed by Zhang et al. (2016) to explain the blobs in their jet observations. One possible way to identify which mechanism created

the knots is whether they are stationary in the jet beam. If they are stationary then it's due to shock waves, if they move through the jet beam then it's due to magnetic reconnection driving a tearing mode instability. This further emphasises the importance of studying knots in spicules this gives another path to investigate the origin of the driver. Interestingly, the formation of the blobs by magnetic reconnection has been proposed for chromospheric anemone jets (Singh et al., 2012), alluding that blobs may occur over a range of different scales of jets (Zhang et al., 2016).

Chen et al. (2015, 2017) reported multiple jets observed at the western edge

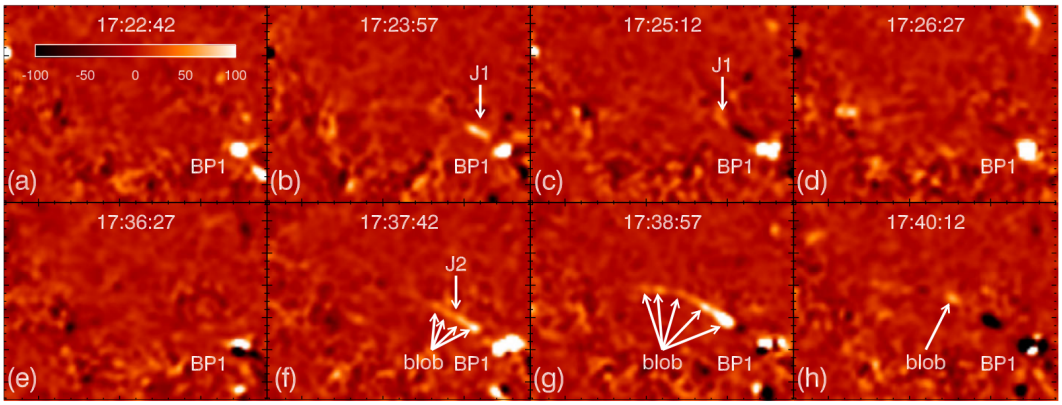

Figure 5.8: Observations of solar jets on 2014 September 10 taken from Zhang et al. (2016). Panels (a-h) are running difference images in 171 $\mathring{A}$ show the occurrence of two jets (J1, J2). The white arrows highlight where the bright blob-like structures sit along the jet beam.

of AR 11513 on the 2nd and 3rd of July 2012. In these jets, blobs are seen in the jet beam (see Fig. 5.9). The space-borne observations were captured with SDO using the Atmospheric Imaging Assembly (AIA) instrument. AIA has a spatial resolution of 1088 km (1.5″) and a temporal resolution of 12 s for the EUV lines shown in Fig. 5.9. The example jet clearly shows blobs, as highlighted by slices 1 and 2 in panel (b). The conditions under which these form are similar to that outlined by Zhang and Ji (2014) and Zhang et al. (2016), as the brightening at the base of the jet has been shown to contain magnetic fields of opposite polarities (Chen et al., 2017).

The suggested mechanism of blob formation in Zhang et al. (2016) is plausible, but so too is the mechanism put forward in Section 3.3.1 for blobs/knots to form in the jet beam when the flow is sufficient. In Fig 5.8 jets J1 and J2 have high apparent speeds of 145 ± 15 km s^{-1} and $203 \pm$ km s^{-1} respectively

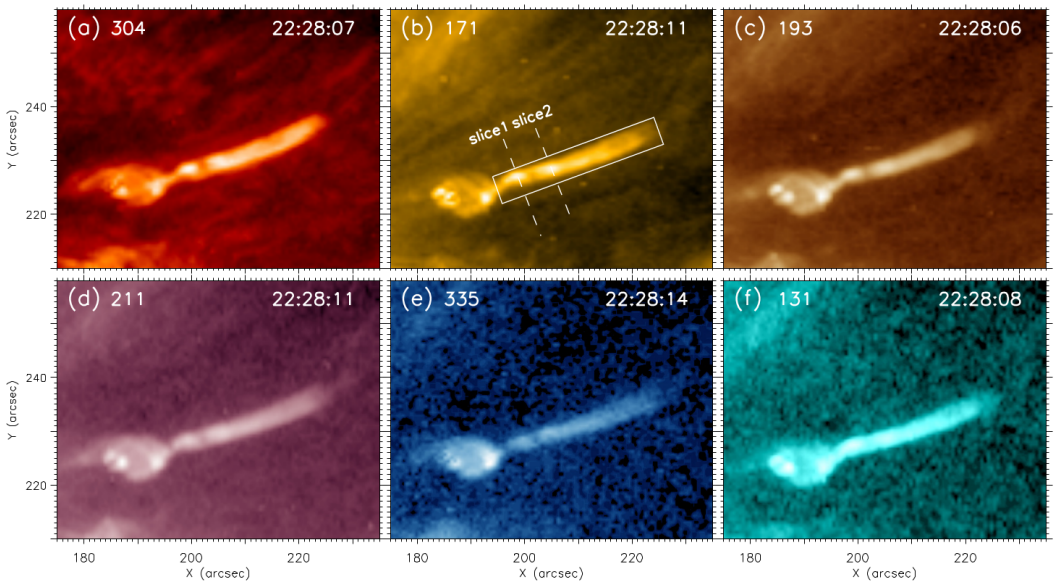

Figure 5.9: EUV jet observed in the west of AR 11513 on July 2, 2012. Each panel represents different passband observations denoted in the top left-hand corner in units of Angstroms. The bright blobs in the jet beam are most noticeable in 171 $\mathring{A}$ where the slices are located. This figure and the analysis it encapsulates was produced by Dr. Chen.

(Zhang et al., 2016) and the jet in Fig. 5.9 is approximately 200 km s^{-1} (Chen et al., 2017). Based on the results of the simulations in the thesis it is feasible with these high speeds in a coronal environment for the blob formation to be generated/driven by shocks containing waves trapped in a jet beam. To rule out blobs forming due to shocks, one needs to measure the flow rate of the jet. This is because, as demonstrated in Chapter 3, when the driver for the jet switches off, the knots start to fall through the jet and disappear. Therefore, if there is a continuous flow then a shock-based process may be plausible, or if it is a short, burst-like release of energy that produces flow then it is more likely to be due to magnetic reconnection.

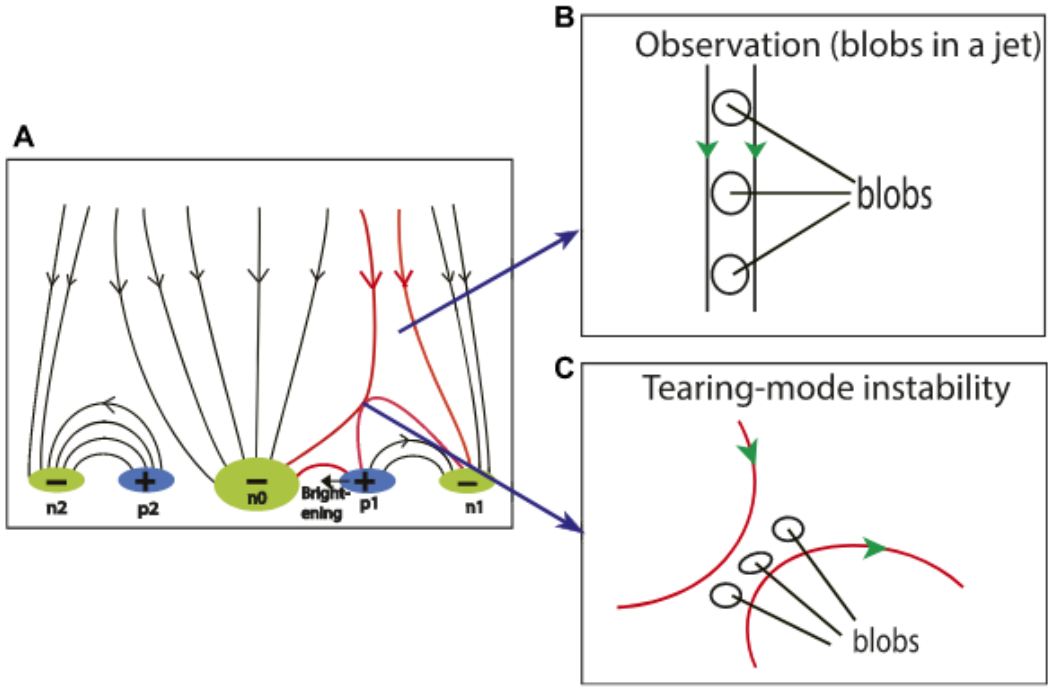

Figure 5.10: A cartoon outlining an example of magnetic reconnection jet formation. Panel A shows the magnetic field configuration, B shows the presence of "blobs" or knots that have been driven upwards from the reconnection location and C shows the formation of knots at the reconnection site where tearing mode instability is occurring. Cartoon taken from Chen et al. (2022)

5.6 Summary and Discussion

This Chapter compares the CSW properties of the synthetic jets with three observations of spicules captured with high-resolution CRISP/SST Hα data. For both the simulation and observation, wave behaviour is identified by CSW estimates. Wavelet analysis of the CSW shows the effects of plasma flows on estimated periods. The Chapter discusses the possibilities that blob structures in observations of large solar jets could be knots produced by trapped shock waves in the jet. The main conclusions drawn from the results as follows:

- CSW variations are present in both the observed and synthetic jets, which highlight that CSW variations are a fundamental property of spicule jets. Earlier reports interpreted these variations as a consequence of confined sausage waves in chromospheric jet structures, although similar characteristics are also shown by MHD fluting wave modes. Here, for the first time, an alternate explanation is provided in terms of internal shock waves for cross-sectional deformations of chromospheric waveguides. In Chapter 3 we discussed that this phenomenon occurs over

a whole range of jets with vastly different length scales, e.g. from astrophysical to laboratory jets. Therefore, the CSW variations are an intrinsic physical characteristic of jets with fast flow speeds. However, insufficient attention has been paid to this for solar jets, primarily due to observational constraints.

- Spectral analysis using wavelet transform suggests noticeable modulation in estimated periodicities for the CSW in both observed and synthetic jet structures. In most cases, the CSW variations have a shorter period in the falling phase than the rising phase. Similar effects were reported in the past for changes in linear MHD wave characteristics due to mass flows in theoretical and prominence studies.

- For the first time, the first overtone in the estimated periodicity is identified in both observed and simulated dynamic chromospheric waveguides (spicules). This could have important implications for chromospheric magneto-seismology, further enabling the estimation of much needed information for the longitudinal plasma and magnetic field for chromospheric jets.

- Knot formation could be an alternative explanation for blob structures reported in larger solar jets.

This Chapter indicates the possible coupling between the longitudinal mass motions and CSW variations in spicule structures. Understanding such behaviour is crucial for the accurate estimation of the overall energy budget for atmospheric heating and associated dissipation mechanisms. Furthermore, simulations suggest the formation of knot substructures within the jet beam, prevalent during the rise-phase of plasma density. These substructures were closely linked with the estimated CSW variations in the jet and could be generated due to shock waves. The simulation results should inform observers to be cautious in attributing CSW variation in fast-flowing jets to sausage waves, as there other mechanisms, (e.g. shock waves occurring in supersonic flows) that can display CSW variations.

For the larger-scale EUV jets, it should be noted that regardless of formation mechanisms of knots in the jet beam, they can occur over a whole range of scales in jets. It is likely that with the increase in spatial observation on the horizon for spicules, it is only a matter of time before knot structures are observed in spicular jets.

CHAPTER 6
Conclusion and Future Work

6.1 Conclusion

The thesis aimed to investigate the fundamental dynamics and morphology of spicular jets. We have achieved this through a simple model, which uses a momentum pulse to drive the jets to simulate a transfer of mass in an idealised solar atmosphere and with a vertical uniform magnetic field. We have taken full advantage of MPI-AMRVAC mesh options to simulate the synthetic jets' rising and falling dynamics with a high spatial resolution.

In Chapter 3 vertical launching of the jet was investigated. An extensive parameter space was investigated, which determined that spicule dynamics and morphology are sensitive to the parameters related to the driver (lifetimes and initial amplitude) and magnetic environment (magnetic field strength). The vertical and horizontal evolution of spicules is measured with our own automated jet tracking software. By using the jet tracking software we capture the main observable features of spicules with the synthetic jets, as we obtained similar heights, speeds, widths and trajectories. Despite numerous numerical studies on the subject of spicular jets, few have reported on the CSW variations and fine structures of spicular jets. We report on both of these and find complex fine structures in the jet beam of spicules due to shock waves, which also create symmetrical deformation of the jet boundary. These fine structures are yet to be observed, but we show that higher resolution observations with telescopes such as DKIST may be able to identify these fine structures.

In Chapter 4 we continued to study with the same model for launching jets, but explored the effects that misalignment between the direction of the driver and the magnetic field has on the dynamics and morphology of the synthetic jet. The tilt of the synthetic jet flows introduces interesting dynamics that were

not seen in Chapter 3. The main result of this study, even with small tilts angles of 5°, there is a significant impact on the appearance of the synthetic jets. In this thesis, we have presented one of the few models that obtained both the transverse and horizontal dynamics of the spicule. An interesting result is that the misaligned flows cause whip motions and redistribution of the densities to the jet edges. We tentatively propose that the whip motions are possibly a consequence of a DKI, but further research is required. Our research highlights the importance of properly tracking the central axis of the jets to obtain accurate jet trajectories and measurements of CSWs. Non-field aligned flows give another possibility for producing transverse motion in spicules. Given the complexity of the structure of the atmosphere that spicules propagate in, we conjecture that it is likely that non-field flow will occur, and it is an important aspect to include in any models of spicules.

In Chapter 5 we revisit the field-aligned jets and compare their properties with Hα observations captured by SST. CSW variations are present in both observations and synthetic jets. We perform a wavelet analysis to measure any significant wave periods. One of the main results in this thesis is that we are the first to report differences in the jet boundary deformation when the jet is in its rising or falling phase. Under the wave interpretation, there is frequency modulation in the falling phase of all the jets, with shorter periods in the falling phase in comparison to the rising phase. We propose that this is due to the change in direction of the mass flows of the jet with respect to the waves. In this wave-based framework, the results of the synthetic jets could be interpreted as identifying the fundamental mode and its first overtone of the sausage wave. However, I think that the results for the CSW variations of the synthetic jets highlight that we should be cautious with this interpretation. As described in Chapter 4, we showed that CSW variations are possible due to supersonic flows. The boundary deformation of the synthetic jets shows no obvious sign of having an antinode which is an expected feature for a wave, and this may indicate CSW variations are not due to waves, but rather a consequence of the supersonic flow. This result should be kept in mind for observers reporting variations of spicule widths, as there may be other phenomena that can account for these motions.

The numerical study presented here has limitations when compared with the spicules actual nature. To have a closer match with spicules', extra physics

would need to be included, such as radiative transfer, heat conduction, and deploying a 3D model. These limitations are mostly addressed in the future work section. Despite this, there is value in studying less complex models, as they gives insight into the fundamental nature of spicules and allow us to more easily unpick the phenomena occurring in the simulations. This thesis highlights the importance of identifying what is driving the jets, as it is the most important factor for determining their dynamics and morphology. We are at the beginning of the next generation of solar telescopes, with mirror sizes approximately four times that of SST, such as DKIST, which recently released the highest resolution image of the Sun's surface to date and allowed us to see features as small as 30 km, and EST, with first light planned in 2026. When this data becomes available, we can advance our knowledge of the fine structuring of the spicules and pin down their driving mechanism. This would be a significant step forward and allow us to narrow down the appropriate numerical models from which to simulate spicules.

6.2 Future Work

Multiple improvements can be undertaken to build upon the existing work in this thesis. The jet tracking code for the tilted examples could be improved further. Its current weakness is that it relies on horizontal slits to track the central axis. It would be better if one autonomously separated the left and right boundary of the jet, which is not a trivial task. Then, for each boundary, measure a set distance to assign data points to match up with its boundary counterpart. Then, taking the midpoints of these pairs would yield a more accurate position of the central jet axis. Steps that need to be undertaken to integrate numerical simulations with observations are as follows; spicules are 3D objects, therefore with a 2D model we may be missing important dynamics, for example, torsional motions (De Pontieu et al., 2012), and in astrophysical jets, RTI can format the boundary in 3D jet simulations for fast moving jets (Matsumoto and Masada, 2013). A 3D simulation would better capture the dynamical motion of the spicules and may yield interesting results for the behaviour of the boundary deformation. All the simulations in this thesis use a simplified solar atmosphere, and it would be more appropriate to base the atmospheric stratification on semi-empirical data such as VALC or the C7 atmospheric model (Vernazza et al., 1981; Avrett and Loeser, 2008). More

complex physics could be added; radiative transfer and heat conduction are important to include as they can impact the final height of the spicules (Sterling and Mariska, 1990). These additional physics are key if we wish to study the synthetic jet's contribution to chromospheric/coronal heating. Carrying out a two-fluid model of the simulation could be another avenue to investigate, as neutrals could play an important role in spicule evolution (Kuźma et al., 2017a). Another direction to investigate would be to try different magnetic field configurations. A significant progression would be to see how an expanding flux tube would impact the presence of the knots. One major improvement of the model, particularly useful for comparing to observations, would be to use forward modelling to convert the parameter of the simulation into observables. For example, the FoMo code (Van Doorsselaere et al., 2016) is set up to accept MPI-AMRVAC data structures. Forward modelling would allow for a more concrete comparison to observations, and may allow us to identify potential observational signatures for the jet phenomena simulated throughout the thesis.

Bibliography

H. Alfvén. Magneto hydrodynamic waves, and the heating of the solar corona. *Mon. Not. Roy. Astron. Soc.*, 107:211, January 1947. doi: 10.1093/mnras/107.2.211.

C. E. Alissandrakis and C. J. Macris. A Study of the Fine Structure of the Solar Chromosphere at the Limb. *Solar Phys.*, 20(1):47–56, October 1971. doi: 10.1007/BF00146093.

Matthew Allcock and Robert Erdélyi. Magnetohydrodynamic Waves in an Asymmetric Magnetic Slab. *Solar Phys.*, 292(2):35, February 2017. doi: 10.1007/s11207-017-1054-y.

Matthew Allcock, Daria Shukhobodskaia, Noémi Kinga Zsámberger, and Robert Erdélyi. Magnetohydrodynamic waves in multi-layered asymmetric waveguides: solar magneto-seismology theory and application. Frontiers in Astronomy and Space Sciences, 6:48, July 2019. doi: 10.3389/fspas.2019.00048.

J. Andries, T. van Doorsselaere, B. Roberts, G. Verth, E. Verwichte, and R. Erdélyi. Coronal Seismology by Means of Kink Oscillation Overtones. *Space Sci. Rev.*, 149(1-4):3–29, December 2009. doi: 10.1007/s11214-009-9561-2.

Jesse Andries, Inigo Arregui, and Marcel Goossens. Determination of the Coronal Density Stratification from the Observation of Harmonic Coronal Loop Oscillations. *Astrophys. J. Lett.*, 624(1):L57–L60, May 2005. doi: 10.1086/430347.

P. Antolin, D. Schmit, T. M. D. Pereira, B. De Pontieu, and I. De Moortel. Transverse Wave Induced Kelvin-Helmholtz Rolls in Spicules. *Astrophys. J.*, 856(1):44, March 2018. doi: 10.3847/1538-4357/aab34f.

Patrick Antolin, Kazunari Shibata, Takahiro Kudoh, Daiko Shiota, and David Brooks. Predicting observational signatures of coronal heating by Alfvén waves and nanoflares. In Robert Erdélyi and César A. Mendoza-Briceno, editors, Waves & Oscillations in the Solar Atmosphere: Heating and Magneto-Seismology, volume 247, pages 279–287, May 2008. doi: 10.1017/S174392130801497X.

Patrick Antolin, Paolo Pagano, Paola Testa, Antonino Petralia, and Fabio Reale. Reconnection nanojets in the solar corona. Nature Astronomy, 5: 54–62, January 2021. doi: 10.1038/s41550-020-1199-8.

T. Appourchaux and T. Corbard. Searching for g modes. II. Unconfirmed g-mode detection in the power spectrum of the time series of round-trip travel time. *Astron. Astrophys.*, 624:A106, April 2019. doi: 10.1051/0004-6361/201935196.

T. Appourchaux, K. Belkacem, A. M. Broomhall, W. J. Chaplin, D. O. Gough, G. Houdek, J. Provost, F. Baudin, P. Boumier, Y. Elsworth, R. A. García, B. N. Andersen, W. Finsterle, C. Fröhlich, A. Gabriel, G. Grec, A. Jiménez, A. Kosovichev, T. Sekii, T. Toutain, and S. Turck-Chièze. The quest for the solar g modes. *Astron. Astrophys. Rev.*, 18(1-2):197–277, February 2010. doi: 10.1007/s00159-009-0027-z.

V. Archontis, F. Moreno-Insertis, K. Galsgaard, and A. W. Hood. The Three-dimensional Interaction between Emerging Magnetic Flux and a Large-Scale Coronal Field: Reconnection, Current Sheets, and Jets. *Astrophys. J.*, 635 (2):1299–1318, December 2005. doi: 10.1086/497533.

Iñigo Arregui. Wave heating of the solar atmosphere. Philosophical Transactions of the Royal Society of London Series A, 373(2042):20140261–20140261, April 2015. doi: 10.1098/rsta.2014.0261.

Markus J. Aschwanden. Image Processing Techniques and Feature Recognition in Solar Physics. *Solar Phys.*, 262(2):235–275, April 2010. doi: 10.1007/s11207-009-9474-y.

Markus J. Aschwanden. New Millennium Solar Physics, volume 458. 2019. doi: 10.1007/978-3-030-13956-8.

Markus J. Aschwanden and Carolus J. Schrijver. Coronal Loop Oscillations Observed with Atmospheric Imaging Assembly—Kink Mode with Cross-sectional and Density Oscillations. *Astrophys. J.*, 736(2):102, August 2011. doi: 10.1088/0004-637X/736/2/102.

Markus J. Aschwanden, Lyndsay Fletcher, Carolus J. Schrijver, and David Alexander. Coronal Loop Oscillations Observed with the Transition Region and Coronal Explorer. *Astrophys. J.*, 520(2):880–894, August 1999. doi: 10.1086/307502.

Markus J. Aschwanden, Bart de Pontieu, Carolus J. Schrijver, and Alan M. Title. Transverse Oscillations in Coronal Loops Observed with TRACE II. Measurements of Geometric and Physical Parameters. *Solar Phys.*, 206(1): 99–132, March 2002. doi: 10.1023/A:1014916701283.

Markus J. Aschwanden, Amy Winebarger, David Tsiklauri, and Hardi Peter. The Coronal Heating Paradox. *Astrophys. J.*, 659(2):1673–1681, April 2007. doi: 10.1086/513070.

R. G. Athay. The chromosphere and transition region., volume 450, pages 85–133. 1981.

R. G. Athay and T. E. Holzer. The role of spicules in heating the solar atmosphere. *Astrophys. J.*, 255:743–752, April 1982. doi: 10.1086/159873.

E. H. Avrett and R. Loeser. Models of the Solar Chromosphere and Transition Region from SUMER and HRTS Observations: Formation of the Extreme-Ultraviolet Spectrum of Hydrogen, Carbon, and Oxygen. *Astrophys. J. Suppl.*, 175:229–276, March 2008. doi: 10.1086/523671.

T. Ayres, H. Uitenbroek, G. Cauzzi, K. Reardon, T. Berger, C. Schrijver, B. de Pontieu, P. Judge, S. McIntosh, S. White, and S. Solanki. The Solar Chromosphere: Old Challenges, New Frontiers. In astro2010: The Astronomy and Astrophysics Decadal Survey, volume 2010, page 9, January 2009.

Thomas R. Ayres. Chapter 2 - Stellar and Solar Chromospheres and Attendant Phenomena, pages 27–57. 2019. doi: 10.1016/B978-0-12-814334-6.00002-9.

S. D. Bale, S. T. Badman, J. W. Bonnell, T. A. Bowen, D. Burgess, A. W. Case, C. A. Cattell, B. D. G. Chandran, C. C. Chaston, C. H. K. Chen, J. F. Drake, T. Dudok de Wit, J. P. Eastwood, R. E. Ergun, W. M. Farrell, C. Fong, K. Goetz, M. Goldstein, K. A. Goodrich, P. R. Harvey, T. S. Horbury,

G. G. Howes, J. C. Kasper, P. J. Kellogg, J. A. Klimchuk, K. E. Korreck, V. V. Krasnoselskikh, S. Krucker, R. Laker, D. E. Larson, R. J. MacDowall, M. Maksimovic, D. M. Malaspina, J. Martinez-Oliveros, D. J. McComas, N. Meyer-Vernet, M. Moncuquet, F. S. Mozer, T. D. Phan, M. Pulupa, N. E. Raouafi, C. Salem, D. Stansby, M. Stevens, A. Szabo, M. Velli, T. Woolley, and J. R. Wygant. Highly structured slow solar wind emerging from an equatorial coronal hole. *Nature*, 576(7786):237–242, December 2019. doi: 10.1038/s41586-019-1818-7.

M. Barbulescu and R. Erdélyi. Magnetoacoustic Waves and the Kelvin-Helmholtz Instability in a Steady Asymmetric Slab. I: The Effects of Varying Density Ratios. *Solar Phys.*, 293(6):86, June 2018. doi: 10.1007/s11207-018-1305-6.

Mihai Barbulescu, Michael S. Ruderman, Tom Van Doorsselaere, and Robert Erdélyi. An Analytical Model of the Kelvin-Helmholtz Instability of Transverse Coronal Loop Oscillations. *Astrophys. J.*, 870(2):108, January 2019. doi: 10.3847/1538-4357/aaf506.

J. M. Beckers. Solar spicules. Solar Physic, 3(3):367–433, 1968. ISSN 1573-093X. doi: 10.1007/BF00171614.

J. M. Beckers. Solar Spicules. *Annual Review of Astron and Astrophys.*, 10: 73, 1972. doi: 10.1146/annurev.aa.10.090172.000445.

Jacques M. Beckers. Study of the Undisturbed Chromosphere from Ha-DISK Filtergrams, with Particular Reference to the Indentification of Spicules. *Astrophys. J.*, 138:648, October 1963. doi: 10.1086/147676.

S. M. Bennett and R. Erdélyi. On the Statistics of Macrospicules. *Astrophys. J.*, 808(2):135, August 2015. doi: 10.1088/0004-637X/808/2/135.

T. E. Berger and S. V. Berdyugina. The Observation of Sunspot Light-Bridge Structure and Dynamics. *Astrophys. J. Lett.*, 589(2):L117–L121, June 2003. doi: 10.1086/376494.

Thomas Berger, Andrew Hillier, and Wei Liu. Quiescent Prominence Dynamics Observed with the Hinode Solar Optical Telescope. II. Prominence Bubble Boundary Layer Characteristics and the Onset of a Coupled Kelvin-Helmholtz Rayleigh-Taylor Instability. *Astrophys. J.*, 850(1):60, November 2017. doi: 10.3847/1538-4357/aa95b6.

Thomas E. Berger, Richard A. Shine, Gregory L. Slater, Theodore D. Tarbell, Alan M. Title, Takenori J. Okamoto, Kiyoshi Ichimoto, Yukio Katsukawa, Yoshinori Suematsu, Saku Tsuneta, Bruce W. Lites, and Toshifumi Shimizu. Hinode SOT Observations of Solar Quiescent Prominence Dynamics. *Astrophys. J. Lett.*, 676(1):L89, March 2008. doi: 10.1086/587171.

Thomas E. Berger, Gregory Slater, Neal Hurlburt, Richard Shine, Theodore Tarbell, Alan Title, Bruce W. Lites, Takenori J. Okamoto, Kiyoshi Ichimoto, Yukio Katsukawa, Tetsuya Magara, Yoshinori Suematsu, and Toshifumi Shimizu. Quiescent Prominence Dynamics Observed with the Hinode Solar Optical Telescope. I. Turbulent Upflow Plumes. *Astrophys. J.*, 716 (2):1288–1307, June 2010. doi: 10.1088/0004-637X/716/2/1288.

T. J. Bogdan, M. Carlsson, V. H. Hansteen, A. McMurry, C. S. Rosenthal, M. Johnson, S. Petty-Powell, E. J. Zita, R. F. Stein, S. W. McIntosh, and Å. Nordlund. Waves in the Magnetized Solar Atmosphere. II. Waves from Localized Sources in Magnetic Flux Concentrations. *Astrophys. J.*, 599(1): 626–660, December 2003. doi: 10.1086/378512.

J. D. Bohlin, S. N. Vogel, J. D. Purcell, Jr. Sheeley, N. R., R. Tousey, and M. E. Vanhoosier. A newly observed solar feature: macrospicules in He II 304 Å. *Astrophys. J. Lett.*, 197:L133–L135, May 1975. doi: 10.1086/181794.

G. E. Brueckner. A high-resolution view of the solar chromosphere and corona. Highlights of Astronomy, 5:557–569, January 1980.

P. S. Cally. Magnetohydrodynamic tube waves - Waves in fibrils. Australian Journal of Physics, 38:825–837, January 1985. doi: 10.1071/PH850825.

P. S. Cally and M. Goossens. Three-Dimensional MHD Wave Propagation and Conversion to Alfvén Waves near the Solar Surface. I. Direct Numerical Solution. *Solar Phys.*, 251(1-2):251–265, September 2008. doi: 10.1007/s11207-007-9086-3.

Richard C. Canfield, Kevin P. Reardon, K. D. Leka, K. Shibata, T. Yokoyama, and M. Shimojo. H alpha Surges and X-Ray Jets in AR 7260. *Astrophys. J.*, 464:1016, June 1996. doi: 10.1086/177389.

Peter J. Cargill. The Fine Structure of a Nanoflare-Heated Corona. *Solar Phys.*, 147(2):263–268, October 1993. doi: 10.1007/BF00690717.

Peter J. Cargill and James A. Klimchuk. Nanoflare Heating of the Corona Revisited. *Astrophys. J.*, 605(2):911–920, April 2004. doi: 10.1086/382526.

Rebecca Centeno, Javier Trujillo Bueno, and Andrés Asensio Ramos. On the Magnetic Field of Off-limb Spicules. *Astrophys. J.*, 708(2):1579–1584, January 2010. doi: 10.1088/0004-637X/708/2/1579.

Subrahmanyan Chandrasekhar. Hydrodynamic and hydromagnetic stability. 1961.

Jie Chen, Jiangtao Su, Zhiqiang Yin, T. G. Priya, Hongqi Zhang, Jihong Liu, Haiqing Xu, and Sijie Yu. Recurrent Solar Jets Induced by a Satellite Spot and Moving Magnetic Features. *Astrophys. J.*, 815(1):71, December 2015. doi: 10.1088/0004-637X/815/1/71.

Jie Chen, Jiangtao Su, Yuanyong Deng, and E. R. Priest. A Complex Solar Coronal Jet with Two Phases. *Astrophys. J.*, 840(1):54, May 2017. doi: 10.3847/1538-4357/aa6c59.

Jie Chen, Robertus Erdélyi, Jiajia Liu, Yuanyong Deng, Fionnlagh Mackenzie Dover, Qingmin Zhang, Mei Zhang, Leping Li, and Jiangtao Su. Blobs in a solar euv jet. Frontiers in Astronomy and Space Sciences, 8, 2022. ISSN 2296-987X. doi: 10.3389/fspas.2021.786856. URL https://www.frontiersin.org/article/10.3389/fspas.2021.786856.

Q. Q. Cheng. Fluid Motions in the Solar Atmosphere - Part Two - a Spicule Model with Emission Lines. *Astron. Astrophys.*, 266:549, December 1992a.

Qing-Qi Cheng. Fluid motions in the solar atmosphere. III - A possible explanation of the downflows. *Astron. Astrophys.*, 262(2):581–586, September 1992b.

Qing-Qi Cheng. Fluid motions in the solar atmosphere. I - On the origin and decay of spicules. II - A spicule model with emission lines. *Astron. Astrophys.*, 266(1):537–559, December 1992c.

Georgios Chintzoglou, Bart De Pontieu, Juan Martínez-Sykora, Tiago M. D. Pereira, Angelos Vourlidas, and Samuel Tun Beltran. Bridging the Gap: Capturing the Lyα Counterpart of a Type-II Spicule and Its Heating Evolution with VAULT2.0 and IRIS Observations. *Astrophys. J.*, 857(1):73, April 2018. doi: 10.3847/1538-4357/aab607.

Georgios Chintzoglou, Bart De Pontieu, Juan Martínez-Sykora, Viggo Hansteen, Jaime de la Cruz Rodríguez, Mikolaj Szydlarski, Shahin Jafarzadeh, Sven Wedemeyer, Timothy S. Bastian, and Alberto Sainz Dalda. ALMA and IRIS Observations of the Solar Chromosphere. I. An On-disk Type II Spicule. *Astrophys. J.*, 906(2):82, January 2021. doi: 10.3847/1538-4357/abc9b1.

Il-Hyun Cho, Yong-Jae Moon, Kyung-Suk Cho, Valery M. Nakariakov, Jin-Yi Lee, and Yeon-Han Kim. A New Type of Jet in a Polar Limb of the Solar Coronal Hole. *Astrophys. J. Lett.*, 884(2):L38, October 2019. doi: 10.3847/2041-8213/ab4799.

E. B. Christopoulou, A. A. Georgakilas, and S. Koutchmy. Fine Structure of the Magnetic Chromosphere: Near-Limb Imaging, Data Processing and Analysis of Spicules and Mottles. *Solar Phys.*, 199(1):61–80, March 2001. doi: 10.1023/A:1010338927151.

M. H. Cohen, D. L. Meier, T. G. Arshakian, D. C. Homan, T. Hovatta, Y. Y. Kovalev, M. L. Lister, A. B. Pushkarev, J. L. Richards, and T. Savolainen. Studies of the Jet in Bl Lacertae. I. Recollimation Shock and Moving Emission Features. *Astrophys. J.*, 787(2):151, June 2014. doi: 10.1088/0004-637X/787/2/151.

J. W. Cook, G. E. Brueckner, J. D. F. Bartoe, and D. G. Socker. HRTS observations of spicular emission at transition region temperatures above the solar limb. Advances in Space Research, 4(8):59–62, January 1984. doi: 10.1016/0273-1177(84)90366-1.

T. Cragg, R. Howard, and H. Zirin. Vertical Structures in the Chromosphere. *Astrophys. J.*, 138:303, July 1963. doi: 10.1086/147643.

Elisabete M. de Gouveia Dal Pino. Astrophysical jets and outflows. Advances in Space Research, 35(5):908–924, January 2005. doi: 10.1016/j.asr.2005.03.145.

J. de la Cruz Rodríguez and H. Socas-Navarro. Are solar chromospheric fibrils tracing the magnetic field? *Astron. Astrophys.*, 527:L8, March 2011. doi: 10.1051/0004-6361/201016018.

J. de la Cruz Rodríguez, M. G. Löfdahl, P. Sütterlin, T. Hillberg, and L. Rouppe van der Voort. CRISPRED: A data pipeline for the CRISP

imaging spectropolarimeter. *Astron. Astrophys.*, 573:A40, January 2015. doi: 10.1051/0004-6361/201424319.

I. De Moortel, C. E. Parnell, and A. W. Hood. Determination of coronal loop properties from trace observations. *Solar Phys.*, 215:69–86, July 2003. doi: 10.1023/A:1024856300248.

B. De Pontieu. Chromospheric Dynamics: Spicules and Waves, volume 369 of Astronomical Society of the Pacific Conference Series, page 231. 2007.

B. De Pontieu, R. Erdélyi, and S. P. James. Solar chromospheric spicules from the leakage of photospheric oscillations and flows. *Nature*, 430:536–539, July 2004. doi: 10.1038/nature02749.

B. De Pontieu, R. Erdélyi, and I. De Moortel. How to Channel Photospheric Oscillations into the Corona. *Astrophys. J. Lett.*, 624(1):L61–L64, May 2005. doi: 10.1086/430345.

B. De Pontieu, V. H. Hansteen, L. Rouppe van der Voort, M. van Noort, and M. Carlsson. High-Resolution Observations and Modeling of Dynamic Fibrils. *Astrophys. J.*, 655(1):624–641, January 2007a. doi: 10.1086/509070.

B. De Pontieu, S. McIntosh, V. H. Hansteen, M. Carlsson, C. J. Schrijver, T. D. Tarbell, A. M. Title, R. A. Shine, Y. Suematsu, S. Tsuneta, Y. Katsukawa, K. Ichimoto, T. Shimizu, and S. Nagata. A Tale of Two Spicules: The Impact of Spicules on the Magnetic Chromosphere. *Pub. Astron. Soc. Japan*, 59: S655–S662, November 2007b. doi: 10.1093/pasj/59.sp3.S655.

B. De Pontieu, S. W. McIntosh, M. Carlsson, V. H. Hansteen, T. D. Tarbell, C. J. Schrijver, A. M. Title, R. A. Shine, S. Tsuneta, Y. Katsukawa, K. Ichimoto, Y. Suematsu, T. Shimizu, and S. Nagata. Chromospheric Alfvénic Waves Strong Enough to Power the Solar Wind. Science, 318:1574, December 2007c. doi: 10.1126/science.1151747.

B. De Pontieu, S. W. McIntosh, M. Carlsson, V. H. Hansteen, T. D. Tarbell, P. Boerner, J. Martinez-Sykora, C. J. Schrijver, and A. M. Title. The Origins of Hot Plasma in the Solar Corona. Science, 331(6013):55, January 2011. doi: 10.1126/science.1197738.

B. De Pontieu, M. Carlsson, L. H. M. Rouppe van der Voort, R. J. Rutten, V. H. Hansteen, and H. Watanabe. Ubiquitous Torsional Motions

in Type II Spicules. *Astrophys. J. Lett.*, 752(1):L12, June 2012. doi: 10.1088/2041-8205/752/1/L12.

B. De Pontieu, I. De Moortel, J. Martinez-Sykora, and S. W. McIntosh. Observations and Numerical Models of Solar Coronal Heating Associated with Spicules. *Astrophys. J. Lett.*, 845(2):L18, August 2017a. doi: 10.3847/2041-8213/aa7fb4.

Bart De Pontieu, Viggo H. Hansteen, Luc Rouppe van der Voort, Michiel van Noort, and Mats Carlsson. Observations and Simulations of Fibrils and Mottles. ArXiv e-prints, art. astro-ph/0702081, February 2007d.

Bart De Pontieu, A. M. Title, J. Lemen, J. Wuelser, T. D. Tarbell, C. J. Schrijver, L. Golub, C. Kankelborg, M. Carlsson, V. H. Hansteen, S. Worden, and IRIS Team. The Interface Region Imaging Spectrograph (IRIS). In AAS/Solar Physics Division Abstracts #44, volume 44 of AAS/Solar Physics Division Meeting, page 100.03, July 2013.

Bart De Pontieu, Juan Martínez-Sykora, and Georgios Chintzoglou. What Causes the High Apparent Speeds in Chromospheric and Transition Region Spicules on the Sun? *Astrophys. J. Lett.*, 849(1):L7, November 2017b. doi: 10.3847/2041-8213/aa9272.

A. Dedner, F. Kemm, D. Kröner, C. D. Munz, T. Schnitzer, and M. Wesenberg. Hyperbolic Divergence Cleaning for the MHD Equations. Journal of Computational Physics, 175(2):645–673, January 2002. doi: 10.1006/jcph.2001.6961.

P. Demarque and D. B. Guenther. Helioseismology: Probing the Interior of a Star. Proceedings of the National Academy of Science, 96(10):5356–5359, May 1999. doi: 10.1073/pnas.96.10.5356.

H. L. Demastus, W. J. Wagner, and R. D. Robinson. Coronal Disturbances. I: Fast Transient Events Observed in the Green Coronal Emission Line During the Last Solar Cycle. *Solar Phys.*, 31(2):449–459, August 1973. doi: 10.1007/BF00152820.

V. Domingo, B. Fleck, and A. I. Poland. SOHO: The Solar and Heliospheric Observatory. *Space Sci. Rev.*, 72(1-2):81–84, April 1995. doi: 10.1007/BF00768758.

Fionnlagh Mackenzie Dover, Rahul Sharma, Marianna B. Korsós, and Robertus Erdélyi. Signatures of Cross-sectional Width Modulation in Solar Spicules due to Field-aligned Flows. *Astrophys. J.*, 905(1):72, December 2020. doi: 10.3847/1538-4357/abc349.

J. F. Drake, M. Swisdak, H. Che, and M. A. Shay. Electron acceleration from contracting magnetic islands during reconnection. *Nature*, 443(7111): 553–556, October 2006. doi: 10.1038/nature05116.

P. G. Drazin. Introduction to Hydrodynamic Stability. 2002.

T. J. Duckenfield, C. R. Goddard, D. J. Pascoe, and V. M. Nakariakov. Observational signatures of the third harmonic in a decaying kink oscillation of a coronal loop. *Astron. Astrophys.*, 632:A64, December 2019. doi: 10.1051/0004-6361/201936822.

R. B. Dunn, J. T. Jefferies, and F. Q. Orrall. The line and continuous emission observed in two limb flares. The Observatory, 80:31–33, February 1960.

H. Ebadi and M. Ghiassi. Observation of kink waves and their reconnection-like origin in solar spicules. *Astrophys. Space Sci.*, 353(1):31–36, September 2014. doi: 10.1007/s10509-014-2020-x.

Daniel Edgington-Mitchell, Damon R. Honnery, and Julio Soria. The underexpanded jet Mach disk and its associated shear layer. Physics of Fluids, 26 (9):096101, September 2014. doi: 10.1063/1.4894741.

Bengt Edlén. Die Deutung der Emissionslinien im Spektrum der Sonnenkorona. Mit 6 Abbildungen. *Zeitschrift fuer Astrophysik*, 22:30, January 1943.

P. M. Edwin and B. Roberts. Wave Propagation in a Magnetically Structured Atmosphere - Part Three - the Slab in a Magnetic Environment. *Solar Phys.*, 76(2):239–259, March 1982. doi: 10.1007/BF00170986.

R. Erdélyi and S. P. James. Can ion-neutral damping help to form spicules?. II. Random driver. *Astron. Astrophys.*, 427:1055–1064, December 2004. doi: 10.1051/0004-6361:20040345.

Robert Erdélyi. Coronal heating: Heating in the solar atmosphere. Astronomy and Geophysics, 45(4):4.34–4.37, August 2004. doi: 10.1046/j.1468-4004.2003.45434.x.

D. F. Escande, V. Gondret, and F. Sattin. Relevant heating of the quiet solar corona by Alfvén waves: a result of adiabaticity breakdown. Scientific Reports, 9:14274, October 2019. doi: 10.1038/s41598-019-50820-x.

B. Filippov, A. K. Srivastava, B. N. Dwivedi, S. Masson, G. Aulanier, N. C. Joshi, and W. Uddin. Formation of a rotating jet during the filament eruption on 2013 April 10-11. *Mon. Not. Roy. Astron. Soc.*, 451(1):1117–1129, July 2015. doi: 10.1093/mnras/stv1039.

E. Fossat and F. X. Schmider. More about solar g modes. *Astron. Astrophys.*, 612:L1, April 2018. doi: 10.1051/0004-6361/201832626.

E. Fossat, P. Boumier, T. Corbard, J. Provost, D. Salabert, F. X. Schmider, A. H. Gabriel, G. Grec, C. Renaud, J. M. Robillot, T. Roca-Cortés, S. Turck-Chièze, R. K. Ulrich, and M. Lazrek. Asymptotic g modes: Evidence for a rapid rotation of the solar core. *Astron. Astrophys.*, 604:A40, August 2017. doi: 10.1051/0004-6361/201730460.

Peter Foukal. Morphological Relationships in the Chromospheric Hα Fine Structure. *Solar Phys.*, 19(1):59–71, August 1971a. doi: 10.1007/BF00148824.

Peter Foukal. Hα Fine Structure and the Chromospheric Field. *Solar Phys.*, 20(2):298–309, November 1971b. doi: 10.1007/BF00159759.

Claire Foullon, Erwin Verwichte, Valery M. Nakariakov, Katariina Nykyri, and Charles J. Farrugia. Magnetic Kelvin-Helmholtz Instability at the Sun. *Astrophys. J. Lett.*, 729(1):L8, March 2011. doi: 10.1088/2041-8205/729/1/L8.

Claire Foullon, Erwin Verwichte, Katariina Nykyri, Markus J. Aschwanden, and Iain G. Hannah. Kelvin-Helmholtz Instability of the CME Reconnection Outflow Layer in the Low Corona. *Astrophys. J.*, 767(2):170, April 2013. doi: 10.1088/0004-637X/767/2/170.

D. Fujimura and S. Tsuneta. Properties of Magnetohydrodynamic Waves in the Solar Photosphere Obtained with Hinode. *Astrophys. J.*, 702(2):1443–1457, September 2009. doi: 10.1088/0004-637X/702/2/1443.

Harold P. Furth, John Killeen, and Marshall N. Rosenbluth. Finite-Resistivity Instabilities of a Sheet Pinch. Physics of Fluids, 6(4):459–484, April 1963. doi: 10.1063/1.1706761.

R. Gafeira, S. Jafarzadeh, S. K. Solanki, A. Lagg, M. van Noort, P. Barthol, J. Blanco Rodríguez, J. C. del Toro Iniesta, A. Gandorfer, L. Gizon, J. Hirzberger, M. Knölker, D. Orozco Suárez, T. L. Riethmüller, and W. Schmidt. Oscillations on Width and Intensity of Slender Ca II H Fibrils from Sunrise/SuFI. *Astrophys. J. Suppl.*, 229(1):7, March 2017a. doi: 10.3847/1538-4365/229/1/7.

R. Gafeira, A. Lagg, S. K. Solanki, S. Jafarzadeh, M. van Noort, P. Barthol, J. Blanco Rodríguez, J. C. del Toro Iniesta, A. Gandorfer, L. Gizon, J. Hirzberger, M. Knölker, D. Orozco Suárez, T. L. Riethmüller, and W. Schmidt. Morphological Properties of Slender Ca II H Fibrils Observed by SUNRISE II. *Astrophys. J. Suppl.*, 229(1):6, March 2017b. doi: 10.3847/1538-4365/229/1/6.

Rafael A. García, Sylvaine Turck-Chièze, Sebastian J. Jiménez-Reyes, Jérôme Ballot, Pere L. Pallé, Antonio Eff-Darwich, Savita Mathur, and Janine Provost. Tracking Solar Gravity Modes: The Dynamics of the Solar Core. Science, 316(5831):1591, June 2007. doi: 10.1126/science.1140598.

G. Allen Gary. Plasma Beta above a Solar Active Region: Rethinking the Paradigm. *Solar Phys.*, 203(1):71–86, October 2001. doi: 10.1023/A:1012722021820.

A. A. Georgakilas, S. Koutchmy, and C. E. Alissandrakis. Polar surges and macrospicules: simultaneous Hα and He BT II 304 Angstroms observations. *Astron. Astrophys.*, 341:610–616, January 1999.

Johan Peter Goedbloed and Stefaan Poedts. Principles of magnetohydrodynamics: with applications to laboratory and astrophysical plasmas. Cambridge university press, 2004.

J. J. González-Avilés, F. S. Guzmán, and V. Fedun. Jet Formation in Solar Atmosphere due to Magnetic Reconnection. *Astrophys. J.*, 836:24, February 2017. doi: 10.3847/1538-4357/836/1/24.

J. J. González-Avilés, F. S. Guzmán, V. Fedun, G. Verth, S. Shelyag, and S. Regnier. I. Jet Formation and Evolution Due to 3D Magnetic Reconnection. *Astrophys. J.*, 856(2):176, April 2018. doi: 10.3847/1538-4357/aab36f.

J. J. González-Avilés, F. S. Guzmán, V. Fedun, G. Verth, R. Sharma, S. Shelyag, and S. Regnier. In situ generation of coronal Alfvén waves

by jets. *Mon. Not. Roy. Astron. Soc.*, 484(2):1936–1945, April 2019. doi: 10.1093/mnras/stz087.

J. J. González-Avilés, K. Murawski, A. K. Srivastava, T. V. Zaqarashvili, and J. A. González-Esparza. Numerical simulations of macrospicule jets under energy imbalance conditions in the solar atmosphere. *Mon. Not. Roy. Astron. Soc.*, 505(1):50–64, July 2021. doi: 10.1093/mnras/stab1261.

M. Goossens, J. Terradas, J. Andries, I. Arregui, and J. L. Ballester. On the nature of kink MHD waves in magnetic flux tubes. *Astron. Astrophys.*, 503 (1):213–223, August 2009. doi: 10.1051/0004-6361/200912399.

Marcel Goossens, Joseph V. Hollweg, and Takashi Sakurai. Resonant Behaviour of Magnetohydrodynamic Waves on Magnetic Flux Tubes - Part Three. *Solar Phys.*, 138(2):233–255, April 1992. doi: 10.1007/BF00151914.

B. E. Gordon and J. V. Hollweg. Collisional damping of surface waves in the solar corona. *Astrophys. J.*, 266:373–382, March 1983. doi: 10.1086/160785.

U. Grossmann-Doerth and W. Schmidt. Chromospheric fine structure revisited. *Astron. Astrophys.*, 264(1):236–242, October 1992.

Ulrich Grossmann-Doerth and Marina von Uexküll. Spectral Investigation of the Chromosphere. II. The Nature of the Mottles and a Model of the Overall Structure. *Solar Phys.*, 28(2):319–332, February 1973. doi: 10.1007/BF00152301.

W. Grotrian. Zur Frage der Deutung der Linien im Spektrum der Sonnenkorona. Naturwissenschaften, 27(13):214–214, March 1939. doi: 10.1007/BF01488890.

Y. Guo, R. Erdélyi, A. K. Srivastava, Q. Hao, X. Cheng, P. F. Chen, M. D. Ding, and B. N. Dwivedi. Magnetohydrodynamic Seismology of a Coronal Loop System by the First Two Modes of Standing Kink Waves. *Astrophys. J.*, 799(2):151, February 2015. doi: 10.1088/0004-637X/799/2/151.

Kazuhiro Hada, Motoki Kino, Akihiro Doi, Hiroshi Nagai, Mareki Honma, Yoshiaki Hagiwara, Marcello Giroletti, Gabriele Giovannini, and Noriyuki Kawaguchi. The Innermost Collimation Structure of the M87 Jet Down to

~10 Schwarzschild Radii. *Astrophys. J.*, 775(1):70, September 2013. doi: 10.1088/0004-637X/775/1/70.

Gerhard Haerendel. Weakly damped Alfvén waves as drivers of solar chromospheric spicules. *Nature*, 360(6401):241–243, November 1992. doi: 10.1038/360241a0.

V. H. Hansteen. Waves and Shocks in the Solar Atmosphere. In K. Shibata, S. Nagata, and T. Sakurai, editors, New Solar Physics with Solar-B Mission, volume 369 of Astronomical Society of the Pacific Conference Series, page 193, October 2007.

V. H. Hansteen, B. De Pontieu, L. Rouppe van der Voort, M. van Noort, and M. Carlsson. Dynamic Fibrils Are Driven by Magnetoacoustic Shocks. *Astrophys. J. Lett.*, 647(1):L73–L76, August 2006. doi: 10.1086/507452.

Amiram. Harten, Peter D Lax, and Bram van. Leer. On Upstream Differencing and Godunov-Type Schemes for Hyperbolic Conservation Laws. SIAM Review, 25(1):35–61, 1983. doi: 10.1137/1025002. URL https://doi.org/10.1137/1025002.

J. S. He, C. Y. Tu, E. Marsch, L. J. Guo, S. Yao, and H. Tian. Upward propagating high-frequency Alfvén waves as identified from dynamic wave-like spicules observed by SOT on Hinode. *Astron. Astrophys.*, 497(2):525–535, April 2009a. doi: 10.1051/0004-6361/200810777.

Jiansen He, Eckart Marsch, Chuanyi Tu, and Hui Tian. Excitation of Kink Waves Due to Small-Scale Magnetic Reconnection in the Chromosphere? *Astrophys. J. Lett.*, 705(2):L217–L222, November 2009b. doi: 10.1088/0004-637X/705/2/L217.

L. Heggland, B. De Pontieu, and V. H. Hansteen. Numerical Simulations of Shock Wave-driven Chromospheric Jets. *Astrophys. J.*, 666(2):1277–1283, September 2007. doi: 10.1086/518828.

V. M. J. Henriques, D. Kuridze, M. Mathioudakis, and F. P. Keenan. Quiet-Sun Hα Transients and Corresponding Small-scale Transition Region and Coronal Heating. *Astrophys. J.*, 820:124, April 2016. doi: 10.3847/0004-637X/820/2/124.

D. Heristchi and Z. Mouradian. On the Inclination and the Axial Velocity of Spicules. *Solar Phys.*, 142(1):21–34, November 1992. doi: 10.1007/BF00156631.

O. Hervet, Z. Meliani, A. Zech, C. Boisson, V. Cayatte, C. Sauty, and H. Sol. Shocks in relativistic transverse stratified jets. A new paradigm for radio-loud AGN. *Astron. Astrophys.*, 606:A103, October 2017. doi: 10.1051/0004-6361/201730745.

Andrew Hillier, Thomas Berger, Hiroaki Isobe, and Kazunari Shibata. Numerical Simulations of the Magnetic Rayleigh-Taylor Instability in the Kippenhahn-Schlüter Prominence Model. I. Formation of Upflows. *Astrophys. J.*, 746(2):120, February 2012. doi: 10.1088/0004-637X/746/2/120.

J. V. Hollweg. Heating of the corona and solar wind by switch-on shocks. *Astrophys. J.*, 254:806–813, March 1982a. doi: 10.1086/159791.

J. V. Hollweg. On the origin of solar spicules. *Astrophys. J.*, 257:345–353, June 1982b. doi: 10.1086/159993.

J. V. Hollweg, S. Jackson, and D. Galloway. Alfven Waves in the Solar Atmospheres - Part Three - Nonlinear Waves on Open Flux Tubes. *Solar Phys.*, 75(1-2):35–61, January 1982. doi: 10.1007/BF00153458.

Joseph V. Hollweg. Alfvenically Driven Slow Shocks in the Solar Chromosphere and Corona. *Astrophys. J.*, 389:731, April 1992. doi: 10.1086/171246.

Zhenyong Hou, Zhenghua Huang, Lidong Xia, Bo Li, and Hui Fu. Observations of Upward Propagating Waves in the Transition Region and Corona above Sunspots. *Astrophys. J.*, 855(1):65, March 2018. doi: 10.3847/1538-4357/aaab5a.

R. A. Howard, J. D. Moses, A. Vourlidas, J. S. Newmark, D. G. Socker, S. P. Plunkett, C. M. Korendyke, J. W. Cook, A. Hurley, J. M. Davila, W. T. Thompson, O. C. St Cyr, E. Mentzell, K. Mehalick, J. R. Lemen, J. P. Wuelser, D. W. Duncan, T. D. Tarbell, C. J. Wolfson, A. Moore, R. A. Harrison, N. R. Waltham, J. Lang, C. J. Davis, C. J. Eyles, H. Mapson-Menard, G. M. Simnett, J. P. Halain, J. M. Defise, E. Mazy, P. Rochus, R. Mercier, M. F. Ravet, F. Delmotte, F. Auchere, J. P. Delaboudiniere, V. Bothmer, W. Deutsch, D. Wang, N. Rich, S. Cooper, V. Stephens,

G. Maahs, R. Baugh, D. McMullin, and T. Carter. Sun Earth Connection Coronal and Heliospheric Investigation (SECCHI). *Space Sci. Rev.*, 136(1-4):67–115, April 2008. doi: 10.1007/s11214-008-9341-4.

H. S. Hudson. Solar flares, microflares, nanoflares, and coronal heating. *Solar Phys.*, 133(2):357–369, June 1991. doi: 10.1007/BF00149894.

J. D. Hurka, J. Schmid-Burgk, and P. E. Hardee. Deflection of stellar jets by ambient magnetic fields. *Astron. Astrophys.*, 343:558–570, March 1999.

K. Ichimoto, B. Lites, D. Elmore, Y. Suematsu, S. Tsuneta, Y. Katsukawa, T. Shimizu, R. Shine, T. Tarbell, A. Title, J. Kiyohara, K. Shinoda, G. Card, A. Lecinski, K. Streander, M. Nakagiri, M. Miyashita, M. Noguchi, C. Hoffmann, and T. Cruz. Polarization Calibration of the Solar Optical Telescope onboard Hinode. *Solar Phys.*, 249(2):233–261, June 2008. doi: 10.1007/s11207-008-9169-9.

H. Iijima and T. Yokoyama. A Three-dimensional Magnetohydrodynamic Simulation of the Formation of Solar Chromospheric Jets with Twisted Magnetic Field Lines. *Astrophys. J.*, 848(1):38, October 2017. doi: 10.3847/1538-4357/aa8ad1.

H. Isobe, M. R. E. Proctor, and N. O. Weiss. Convection-driven Emergence of Small-Scale Magnetic Fields and their Role in Coronal Heating and Solar Wind Acceleration. *Astrophys. J. Lett.*, 679(1):L57, May 2008. doi: 10.1086/589150.

S. Jafarzadeh, S. K. Solanki, R. Gafeira, M. van Noort, P. Barthol, J. Blanco Rodríguez, J. C. del Toro Iniesta, A. Gandorfer, L. Gizon, J. Hirzberger, M. Knölker, D. Orozco Suárez, T. L. Riethmüller, and W. Schmidt. Transverse Oscillations in Slender Ca II H Fibrils Observed with Sunrise/SuFI. *Astrophys. J. Suppl.*, 229(1):9, March 2017. doi: 10.3847/1538-4365/229/1/9.

S. P. James and R. Erdélyi. Spicule formaion by ion-neutral damping. *Astron. Astrophys.*, 393:L11–L14, October 2002. doi: 10.1051/0004-6361:20021126.

S. P. James, R. Erdélyi, and B. De Pontieu. Can ion-neutral damping help to form spicules? *Astron. Astrophys.*, 406:715–724, August 2003. doi: 10.1051/0004-6361:20030685.

D. B. Jess, D. J. Pascoe, D. J. Christian, M. Mathioudakis, P. H. Keys, and F. P. Keenan. The Origin of Type I Spicule Oscillations. *Astrophys. J. Lett.*, 744(1):L5, January 2012. doi: 10.1088/2041-8205/744/1/L5.

D. B. Jess, R. J. Morton, G. Verth, V. Fedun, S. D. T. Grant, and I. Giagkiozis. Multiwavelength Studies of MHD Waves in the Solar Chromosphere. An Overview of Recent Results. *Space Sci. Rev.*, 190(1-4):103–161, July 2015. doi: 10.1007/s11214-015-0141-3.

David B. Jess, Mihalis Mathioudakis, Robert Erdélyi, Philip J. Crockett, Francis P. Keenan, and Damian J. Christian. Alfvén Waves in the Lower Solar Atmosphere. Science, 323(5921):1582, March 2009. doi: 10.1126/science.1168680.

P. Judge. Observations of the Solar Chromosphere. In John Leibacher, Robert F. Stein, and Han Uitenbroek, editors, Solar MHD Theory and Observations: A High Spatial Resolution Perspective, volume 354 of Astronomical Society of the Pacific Conference Series, page 259, December 2006.

P. G. Judge and M. Carlsson. On the Solar Chromosphere Observed at the LIMB with Hinode. *Astrophys. J.*, 719:469–473, August 2010. doi: 10.1088/0004-637X/719/1/469.

M. L. Kaiser. The STEREO mission: an overview. Advances in Space Research, 36(8):1483–1488, January 2005. doi: 10.1016/j.asr.2004.12.066.

Margarita Karovska and Shadia Rifai Habbal. Dynamical Structure of Extreme Ultraviolet Macrospicules. *Astrophys. J. Lett.*, 431:L59, August 1994. doi: 10.1086/187472.

R. Keppens, Z. Meliani, A. J. van Marle, P. Delmont, A. Vlasis, and B. van der Holst. Parallel, grid-adaptive approaches for relativistic hydro and magnetohydrodynamics. Journal of Computational Physics, 231:718–744, February 2012. doi: 10.1016/j.jcp.2011.01.020.

T. S. Kiss, N. Gyenge, and R. Erdélyi. Systematic Variations of Macrospicule Properties Observed by SDO/AIA over Half a Decade. *Astrophys. J.*, 835 (1):47, January 2017. doi: 10.3847/1538-4357/aa5272.

O. Kjeldseth Moe, Olav Oddbjorn Engvold, and Jacques Maurice Beckers. A Comparison of Spicules in the Hα and He II (304 Å) Lines. *Solar Phys.*, 40 (1):65–68, January 1975. doi: 10.1007/BF00183152.

J. A. Klimchuk and P. J. Cargill. Spectroscopic Diagnostics of Nanoflare-heated Loops. *Astrophys. J.*, 553(1):440–448, May 2001. doi: 10.1086/320666.

Shinji Koide, Jun-Ichi Sakai, Ken-Ichi Nishikawa, and Robert L. Mutel. Numerical Simulation of Bent Jets: Propogation into an Oblique Magnetic Field. *Astrophys. J.*, 464:724, June 1996. doi: 10.1086/177359.

Yuji Kotani and Kazunari Shibata. Numerical simulation of solar photospheric jet-like phenomena caused by magnetic reconnection. *Pub. Astron. Soc. Japan*, 72(5):75, October 2020. doi: 10.1093/pasj/psaa064.

Takahiro Kudoh. Nonlinear Alfvén wave model of spicules and coronal heating. In Robert Erdélyi and César A. Mendoza-Briceno, editors, Waves & Oscillations in the Solar Atmosphere: Heating and Magneto-Seismology, volume 247, pages 195–200, May 2008. doi: 10.1017/S1743921308014877.

Takahiro Kudoh and Kazunari Shibata. Alfvén Wave Model of Spicules and Coronal Heating. *Astrophys. J.*, 514(1):493–505, March 1999. doi: 10.1086/306930.

V. Kukhianidze, T. V. Zaqarashvili, and E. Khutsishvili. Observation of kink waves in solar spicules. *Astron. Astrophys.*, 449(2):L35–L38, April 2006. doi: 10.1051/0004-6361:200600018.

D. Kuridze, R. J. Morton, R. Erdélyi, G. D. Dorrian, M. Mathioudakis, D. B. Jess, and F. P. Keenan. Transverse Oscillations in Chromospheric Mottles. ApJ, 750:51, May 2012. doi: 10.1088/0004-637X/750/1/51.

D. Kuridze, V. Henriques, M. Mathioudakis, R. Erdélyi, T. V. Zaqarashvili, S. Shelyag, P. H. Keys, and F. P. Keenan. The Dynamics of Rapid Redshifted and Blueshifted Excursions in the Solar Hα Line. *Astrophys. J.*, 802(1):26, March 2015. doi: 10.1088/0004-637X/802/1/26.

D. Kuridze, T. V. Zaqarashvili, V. Henriques, M. Mathioudakis, F. P. Keenan, and A. Hanslmeier. Kelvin-Helmholtz Instability in Solar Chromospheric

Jets: Theory and Observation. *Astrophys. J.*, 830(2):133, October 2016. doi: 10.3847/0004-637X/830/2/133.

B. Kuźma, K. Murawski, P. Kayshap, D. Wójcik, A. K. Srivastava, and B. N. Dwivedi. Two-fluid Numerical Simulations of Solar Spicules. *Astrophys. J.*, 849:78, November 2017a. doi: 10.3847/1538-4357/aa8ea1.

B. Kuźma, K. Murawski, T. V. Zaqarashvili, P. Konkol, and A. Mignone. Numerical simulations of solar spicules: Adiabatic and non-adiabatic studies. *Astron. Astrophys.*, 597:A133, January 2017b. doi: 10.1051/0004-6361/201628747.

B. J. Labonte. Activity in the quiet sun. I. Observations of macrospicules in Halpha and D_3. *Solar Phys.*, 61(2):283–296, March 1979. doi: 10.1007/BF00150413.

K. R. Lang. Sun, Earth and Sky. 2006.

Ø. Langangen, B. De Pontieu, M. Carlsson, V. H. Hansteen, G. Cauzzi, and K. Reardon. Search for High Velocities in the Disk Counterpart of Type II Spicules. *Astrophys. J. Lett.*, 679(2):L167, June 2008a. doi: 10.1086/589442.

Øystein Langangen, Mats Carlsson, Luc Rouppe van der Voort, Viggo Hansteen, and Bart De Pontieu. Spectroscopic Measurements of Dynamic Fibrils in the Ca II λ8662 Line. *Astrophys. J.*, 673(2):1194–1200, February 2008b. doi: 10.1086/524377.

J. Leenaarts, M. Carlsson, V. Hansteen, and R. J. Rutten. Non-equilibrium hydrogen ionization in 2D simulations of the solar atmosphere. *Astron. Astrophys.*, 473(2):625–632, October 2007. doi: 10.1051/0004-6361:20078161.

I. Lehmann. P'. Bur. Centr. Seismol. Int. A, 14:87–115, 1936.

Robert B. Leighton, Robert W. Noyes, and George W. Simon. Velocity Fields in the Solar Atmosphere. I. Preliminary Report. *Astrophys. J.*, 135:474, March 1962. doi: 10.1086/147285.

James R. Lemen, Alan M. Title, David J. Akin, Paul F. Boerner, Catherine Chou, Jerry F. Drake, Dexter W. Duncan, Christopher G. Edwards, Frank M. Friedlaender, Gary F. Heyman, Neal E. Hurlburt, Noah L.

Katz, Gary D. Kushner, Michael Levay, Russell W. Lindgren, Dnyanesh P. Mathur, Edward L. McFeaters, Sarah Mitchell, Roger A. Rehse, Carolus J. Schrijver, Larry A. Springer, Robert A. Stern, Theodore D. Tarbell, Jean-Pierre Wuelser, C. Jacob Wolfson, Carl Yanari, Jay A. Bookbinder, Peter N. Cheimets, David Caldwell, Edward E. Deluca, Richard Gates, Leon Golub, Sang Park, William A. Podgorski, Rock I. Bush, Philip H. Scherrer, Mark A. Gummin, Peter Smith, Gary Auker, Paul Jerram, Peter Pool, Regina Soufli, David L. Windt, Sarah Beardsley, Matthew Clapp, James Lang, and Nicholas Waltham. The Atmospheric Imaging Assembly (AIA) on the Solar Dynamics Observatory (SDO). *Solar Phys.*, 275(1-2):17–40, January 2012. doi: 10.1007/s11207-011-9776-8.

Xiaohong Li, Jun Zhang, Shuhong Yang, Yijun Hou, and Robert Erdélyi. Observing Kelvin-Helmholtz instability in solar blowout jet. Scientific Reports, 8:8136, May 2018. doi: 10.1038/s41598-018-26581-4.

Hong Liang, Xiaoliang Hu, Xuefeng Huang, and Jiangrong Xu. Direct numerical simulations of multi-mode immiscible Rayleigh-Taylor instability with high Reynolds numbers. Physics of Fluids, 31(11):112104, November 2019. doi: 10.1063/1.5127888.

Sarah Lee Lippincott. Chromospheric Spicules. Smithsonian Contributions to Astrophysics, 2:15, January 1957.

Wei Liu, Thomas E. Berger, Alan M. Title, and Theodore D. Tarbell. An Intriguing Chromospheric Jet Observed by Hinode: Fine Structure Kinematics and Evidence of Unwinding Twists. *Astrophys. J. Lett.*, 707(1):L37–L41, December 2009. doi: 10.1088/0004-637X/707/1/L37.

Ivan P. Loboda and Sergej A. Bogachev. What is a Macrospicule? *Astrophys. J.*, 871(2):230, February 2019. doi: 10.3847/1538-4357/aafa7a.

D. W. Longcope. A Model for Current Sheets and Reconnection in X-Ray Bright Points. *Astrophys. J.*, 507(1):433–442, November 1998. doi: 10.1086/306319.

D. K. Lynch, J. M. Beckers, and R. B. Dunn. A Morphological Study of Solar Spicules. *Solar Phys.*, 30(1):63–70, May 1973. doi: 10.1007/BF00156173.

C. H. Mandrini, P. Démoulin, L. van Driel-Gesztelyi, B. Schmieder, G. Cauzzi, and A. Hofmann. 3D Magnetic Reconnection at an X-Ray Bright Point. *Solar Phys.*, 168(1):115–133, September 1996. doi: 10.1007/BF00145829.

John T. Mariska. The Solar Transition Region. 1992.

J. Martínez-Sykora, B. De Pontieu, V. H. Hansteen, L. Rouppe van der Voort, M. Carlsson, and T. M. D. Pereira. On the generation of solar spicules and Alfvénic waves. Science, 356(6344):1269–1272, June 2017. doi: 10.1126/science.aah5412.

J Martínez-Sykora, B De Pontieu, V H Hansteen, L Rouppe van der Voort, M Carlsson, and T M D Pereira. On the generation of solar spicules and Alfvénic waves. Science (New York, N.Y.), 356(6344):1269–1272, jun 2017. ISSN 1095-9203. doi: 10.1126/science.aah5412. URL http://www.ncbi.nlm.nih.gov/pubmed/28642434.

Juan Martínez-Sykora, Viggo Hansteen, Bart De Pontieu, and Mats Carlsson. Spicule-Like Structures Observed in Three-Dimensional Realistic Magneto-hydrodynamic Simulations. *Astrophys. J.*, 701(2):1569–1581, August 2009. doi: 10.1088/0004-637X/701/2/1569.

Juan Martínez-Sykora, Bart De Pontieu, Mats Carlsson, and Viggo Hansteen. On the Misalignment between Chromospheric Features and the Magnetic Field on the Sun. *Astrophys. J. Lett.*, 831(1):L1, November 2016. doi: 10.3847/2041-8205/831/1/L1.

Jin Matsumoto and Youhei Masada. Two-dimensional Numerical Study for Rayleigh-Taylor and Richtmyer-Meshkov Instabilities in Relativistic Jets. *Astrophys. J. Lett.*, 772(1):L1, July 2013. doi: 10.1088/2041-8205/772/1/L1.

Jin Matsumoto, Miguel A. Aloy, and Manel Perucho. Linear theory of the Rayleigh-Taylor instability at a discontinuous surface of a relativistic flow. *Mon. Not. Roy. Astron. Soc.*, 472(2):1421–1431, December 2017. doi: 10.1093/mnras/stx2012.

Takuma Matsumoto and Kazunari Shibata. Nonlinear Propagation of Alfvén Waves Driven by Observed Photospheric Motions: Application to the Coronal Heating and Spicule Formation. *Astrophys. J.*, 710(2):1857–1867, February 2010. doi: 10.1088/0004-637X/710/2/1857.

Nandkishore Menon and Beric William Skews. Shock wave configurations and flow structures in non-axisymmetric underexpanded sonic jets. Shock Waves, 20(3):175–190, June 2010. doi: 10.1007/s00193-010-0257-z.

Ronald L. Moore, Alphonse C. Sterling, Jonathan W. Cirtain, and David A. Falconer. Solar X-ray Jets, Type-II Spicules, Granule-size Emerging Bipoles, and the Genesis of the Heliosphere. *Astrophys. J. Lett.*, 731(1):L18, April 2011. doi: 10.1088/2041-8205/731/1/L18.

K. Mooroogen, R. J. Morton, and V. Henriques. Dynamics of internetwork chromospheric fibrils: Basic properties and magnetohydrodynamic kink waves. *Astron. Astrophys.*, 607:A46, November 2017. doi: 10.1051/0004-6361/201730926.

F. Moreno-Insertis, K. Galsgaard, and I. Ugarte-Urra. Jets in Coronal Holes: Hinode Observations and Three-dimensional Computer Modeling. *Astrophys. J. Lett.*, 673(2):L211, February 2008. doi: 10.1086/527560.

R. J. Morton, G. Verth, D. B. Jess, D. Kuridze, M. S. Ruderman, M. Mathioudakis, and R. Erdélyi. Observations of ubiquitous compressive waves in the Sun's chromosphere. Nature Communications, 3:1315, December 2012a. doi: 10.1038/ncomms2324.

Richard J. Morton, Gary Verth, David B. Jess, David Kuridze, Michael S. Ruderman, Mihalis Mathioudakis, and Robertus Erdélyi. Observations of ubiquitous compressive waves in the Sun's chromosphere. Nature Communications, 3:1315, December 2012b. doi: 10.1038/ncomms2324.

J. M. Mosher and T. P. Pope. A statistical study of spicule inclinations. *Solar Phys.*, 53(2):375–384, August 1977. doi: 10.1007/BF00160281.

Daniel Müller and O. Chris St. Cyr. The Solar Orbiter mission. In Silvano Fineschi and Judy Fennelly, editors, Solar Physics and Space Weather Instrumentation V, volume 8862 of Society of Photo-Optical Instrumentation Engineers (SPIE) Conference Series, page 88620E, September 2013. doi: 10.1117/12.2027585.

K. Murawski and T. V. Zaqarashvili. Numerical simulations of spicule formation in the solar atmosphere. *Astron. Astrophys.*, 519:A8, September 2010. doi: 10.1051/0004-6361/201014128.

K. Murawski, A. Solov'ev, Z. E. Musielak, A. K. Srivastava, and J. Kraśkiewicz. Torsional Alfvén waves in solar magnetic flux tubes of axial symmetry. *Astron. Astrophys.*, 577:A126, May 2015. doi: 10.1051/0004-6361/201424545.

V. M. Nakariakov and L. Ofman. Determination of the coronal magnetic field by coronal loop oscillations. *Astron. Astrophys.*, 372:L53–L56, June 2001. doi: 10.1051/0004-6361:20010607.

V. M. Nakariakov and B. Roberts. Magnetosonic Waves in Structured Atmospheres with Steady Flows, I. *Solar Phys.*, 159(2):213–228, July 1995. doi: 10.1007/BF00686530.

V. M. Nakariakov, L. Ofman, E. E. Deluca, B. Roberts, and J. M. Davila. TRACE observation of damped coronal loop oscillations: Implications for coronal heating. Science, 285:862–864, August 1999. doi: 10.1126/science.285.5429.862.

U. Narain and P. Ulmschneider. Chromospheric and Coronal Heating Mechanisms. *Space Sci. Rev.*, 54(3-4):377–445, December 1990. doi: 10.1007/BF00177801.

A S Narayanan. Hydromagnetic surface waves in compressible moving cylindrical flux tubes. Plasma Physics and Controlled Fusion, 33(4):333–338, apr 1991. doi: 10.1088/0741-3335/33/4/005.

Takara Nishikawa. Spicule observations with high spatial resolution. *Pub. Astron. Soc. Japan*, 40(5):613–625, January 1988.

N. Nishizuka, M. Shimizu, T. Nakamura, K. Otsuji, T. J. Okamoto, Y. Katsukawa, and K. Shibata. Giant Chromospheric Anemone Jet Observed with Hinode and Comparison with Magnetohydrodynamic Simulations: Evidence of Propagating Alfvén Waves and Magnetic Reconnection. *Astrophys. J. Lett.*, 683(1):L83, August 2008. doi: 10.1086/591445.

M. L. Norman, K. H. A. Winkler, L. Smarr, and M. D. Smith. Structure and dynamics of supersonic jets. *Astron. Astrophys.*, 113:285–302, Sep 1982.

Takenori J. Okamoto and Bart De Pontieu. Propagating Waves Along Spicules. *Astrophys. J. Lett.*, 736(2):L24, August 2011. doi: 10.1088/2041-8205/736/2/L24.

Norifumi Ono, Masami Yamamoto, and Kazuo Koike. Detection of shock structure around Mach disk in axisymmetric plasma jet. Vacuum, 110:149–153, December 2014. doi: 10.1016/j.vacuum.2014.05.010.

William Oxley, Joseph Scalisi, Michael S. Ruderman, and Róbert Erdélyi. Formation of Chromospheric Spicules in Magnetic Bright Points: An Analytical Approach Using Cartesian Slab Geometry. *Astrophys. J.*, 905(2): 168, December 2020. doi: 10.3847/1538-4357/abcafe.

S. Parenti, B. J. I. Bromage, and G. E. Bromage. An erupting macrospicule. Characteristics derived from SOHO-CDS spectroscopic observations. *Astron. Astrophys.*, 384:303–316, March 2002. doi: 10.1051/0004-6361:20011819.

E. N. Parker. Nanoflares and the Solar X-Ray Corona. *Astrophys. J.*, 330: 474, July 1988. doi: 10.1086/166485.

B. C. Parmenter. Observations of Solar Chromospheric Spicules. *Pub. Astron. Soc. Pac.*, 78(463):250, June 1966. doi: 10.1086/128338.

C. E. Parnell and I. De Moortel. A contemporary view of coronal heating. Philosophical Transactions of the Royal Society of London Series A, 370 (1970):3217–3240, July 2012. doi: 10.1098/rsta.2012.0113.

C. E. Parnell and P. E. Jupp. Statistical Analysis of the Energy Distribution of Nanoflares in the Quiet Sun. *Astrophys. J.*, 529(1):554–569, January 2000. doi: 10.1086/308271.

Jay M. Pasachoff, Robert W. Noyes, and Jacques M. Beckers. Spectral Observations of Spicules at Two Heights in the Solar Chromosphere. *Solar Phys.*, 5(2):131–158, October 1968. doi: 10.1007/BF00147962.

Jay M. Pasachoff, William A. Jacobson, and Alphonse C. Sterling. Limb Spicules from the Ground and from Space. *Solar Phys.*, 260(1):59–82, November 2009. doi: 10.1007/s11207-009-9430-x.

D. J. Pascoe, C. R. Goddard, G. Nisticò, S. Anfinogentov, and V. M. Nakariakov. Damping profile of standing kink oscillations observed by SDO/AIA. *Astron. Astrophys.*, 585:L6, January 2016. doi: 10.1051/0004-6361/201527835.

T. M. D. Pereira, B. De Pontieu, M. Carlsson, V. Hansteen, T. D. Tarbell, J. Lemen, A. Title, P. Boerner, N. Hurlburt, J. P. Wülser, J. Martínez-Sykora, L. Kleint, L. Golub, S. McKillop, K. K. Reeves, S. Saar, P. Testa,

H. Tian, S. Jaeggli, and C. Kankelborg. An Interface Region Imaging Spectrograph First View on Solar Spicules. *Astrophys. J. Lett.*, 792(1):L15, September 2014. doi: 10.1088/2041-8205/792/1/L15.

Tiago M. D. Pereira, Bart De Pontieu, and Mats Carlsson. Quantifying Spicules. *Astrophys. J.*, 759(1):18, November 2012. doi: 10.1088/0004-637X/759/1/18.

Tiago M. D. Pereira, Bart De Pontieu, and Mats Carlsson. The Effects of Spatio-temporal Resolution on Deduced Spicule Properties. *Astrophys. J.*, 764(1):69, February 2013. doi: 10.1088/0004-637X/764/1/69.

Tiago M. D. Pereira, Luc Rouppe van der Voort, and Mats Carlsson. The Appearance of Spicules in High Resolution Observations of Ca II H and Hα. *Astrophys. J.*, 824(2):65, June 2016. doi: 10.3847/0004-637X/824/2/65.

A. Petralia, F. Reale, and P. Testa. Guided flows in coronal magnetic flux tubes. *Astron. Astrophys.*, 609:A18, January 2018. doi: 10.1051/0004-6361/201731827.

C. D. Pike and R. A. Harrison. EUV Observations of a Macrospicule: Evidence for Solar Wind Acceleration? *Solar Phys.*, 175(2):457–465, October 1997. doi: 10.1023/A:1004987505422.

C. D. Pike and H. E. Mason. Rotating Transition Region Features Observed with the SOHO Coronal Diagnostic Spectrometer. *Solar Phys.*, 182(2):333–348, October 1998. doi: 10.1023/A:1005065704108.

G. W. Pneuman and R. A. Kopp. Downflow of Spicular Material and Transition Region Models. *Astron. Astrophys.*, 55:305, March 1977.

G. W. Pneuman and R. A. Kopp. Downflow in the supergranulation network and its implications for transition region models. *Solar Phys.*, 57(1):49–64, March 1978. doi: 10.1007/BF00152043.

Stefan Poedts. MHD waves and heating of the solar corona. In Huguette Sawaya-Lacoste, editor, SOLMAG 2002. Proceedings of the Magnetic Coupling of the Solar Atmosphere Euroconference, volume 505 of ESA Special Publication, pages 273–280, October 2002.

G. A. Porfir'eva and G. V. Yakunina. Chromospheric spicules and solar corona. Astronomical and Astrophysical Transactions, 29(4):567–580, December 2016.

O. Porth, C. Xia, T. Hendrix, S. P. Moschou, and R. Keppens. MPI-AMRVAC for Solar and Astrophysics. *Astrophys. J. Suppl.*, 214:4, September 2014. doi: 10.1088/0067-0049/214/1/4.

E. Priest. Magnetohydrodynamics of the Sun. Cambridge University Press, 2014. ISBN 9780521854719. URL https://books.google.co.uk/books?id=BrbSAgAAQBAJ.

E. R. Priest, C. E. Parnell, and S. F. Martin. A Converging Flux Model of an X-Ray Bright Point and an Associated Canceling Magnetic Feature. *Astrophys. J.*, 427:459, May 1994. doi: 10.1086/174157.

E. R. Priest, C. R. Foley, J. Heyvaerts, T. D. Arber, J. L. Culhane, and L. W. Acton. Nature of the heating mechanism for the diffuse solar corona. *Nature*, 393(6685):545–547, June 1998. doi: 10.1038/31166.

N. E. Raouafi, S. Patsourakos, E. Pariat, P. R. Young, A. C. Sterling, A. Savcheva, M. Shimojo, F. Moreno-Insertis, C. R. DeVore, V. Archontis, T. Török, H. Mason, W. Curdt, K. Meyer, K. Dalmasse, and Y. Matsui. Solar Coronal Jets: Observations, Theory, and Modeling. *Space Sci. Rev.*, 201(1-4):1–53, November 2016. doi: 10.1007/s11214-016-0260-5.

Mark P. Rast, Nazaret Bello González, Luis Bellot Rubio, Wenda Cao, Gianna Cauzzi, Edward DeLuca, Bart De Pontieu, Lyndsay Fletcher, Sarah E. Gibson, Philip G. Judge, Yukio Katsukawa, Maria D. Kazachenko, Elena Khomenko, Enrico Landi, Valentin Martínez Pillet, Gordon J. D. Petrie, Jiong Qiu, Laurel A. Rachmeler, Matthias Rempel, Wolfgang Schmidt, Eamon Scullion, Xudong Sun, Brian T. Welsch, Vincenzo Andretta, Patrick Antolin, Thomas R. Ayres, K. S. Balasubramaniam, Istvan Ballai, Thomas E. Berger, Stephen J. Bradshaw, Mats Carlsson, Roberto Casini, Rebecca Centeno, Steven R. Cranmer, Craig DeForest, Yuanyong Deng, Robertus Erdélyi, Viktor Fedun, Catherine E. Fischer, Sergio J. González Manrique, Michael Hahn, Louise Harra, Vasco M. J. Henriques, Neal E. Hurlburt, Sarah Jaeggli, Shahin Jafarzadeh, Rekha Jain, Stuart M. Jefferies, Peter H. Keys, Adam F. Kowalski, Christoph Kuckein, Jeffrey R. Kuhn, Jiajia Liu, Wei Liu, Dana Longcope, R. T. James McAteer, Scott W. McIntosh, David E. McKenzie, Mari Paz Miralles, Richard J. Morton, Karin Muglach, Chris J. Nelson, Navdeep K. Panesar, Susanna Parenti, Clare E. Parnell, Bala Poduval, Kevin P. Reardon, Jeffrey W. Reep, Thomas A. Schad, Donald Schmit, Rahul Sharma, Hector Socas-Navarro, Abhishek K.

Srivastava, Alphonse C. Sterling, Yoshinori Suematsu, Lucas A. Tarr, Sanjiv Tiwari, Alexandra Tritschler, Gary Verth, Angelos Vourlidas, Haimin Wang, Yi-Ming Wang, NSO, DKIST project, DKIST instrument scientists, the DKIST Science Working Group, and the DKIST Critical Science Plan Community. Critical Science Plan for the Daniel K. Inouye Solar Telescope (DKIST). arXiv e-prints, art. arXiv:2008.08203, August 2020.

G. Revet, B. Khiar, E. Filippov, C. Argiroffi, J. Béard, R. Bonito, M. Cerchez, S. N. Chen, T. Gangolf, D. P. Higginson, A. Mignone, B. Olmi, M. Ouillé, S. N. Ryazantsev, I. Yu. Skobelev, M. I. Safronova, M. Starodubtsev, T. Vinci, O. Willi, S. Pikuz, S. Orlando, A. Ciardi, and J. Fuchs. Laboratory disruption of scaled astrophysical outflows by a misaligned magnetic field. Nature Communications, 12:762, January 2021. doi: 10.1038/s41467-021-20917-x.

Thomas R. Rimmele. Solar adaptive optics, volume 4007 of Society of Photo-Optical Instrumentation Engineers (SPIE) Conference Series, pages 218–231. 2000. doi: 10.1117/12.390301.

Thomas R. Rimmele, Mark Warner, Stephen L. Keil, Philip R. Goode, Michael Knölker, Jeffrey R. Kuhn, Robert R. Rosner, Joseph P. McMullin, Roberto Casini, Haosheng Lin, Friedrich Wöger, Oskar von der Lühe, Alexandra Tritschler, Alisdair Davey, Alfred de Wijn, David F. Elmore, André Fehlmann, David M. Harrington, Sarah A. Jaeggli, Mark P. Rast, Thomas A. Schad, Wolfgang Schmidt, Mihalis Mathioudakis, Donald L. Mickey, Tetsu Anan, Christian Beck, Heather K. Marshall, Paul F. Jeffers, Jacobus M. Oschmann, Andrew Beard, David C. Berst, Bruce A. Cowan, Simon C. Craig, Eric Cross, Bryan K. Cummings, Colleen Donnelly, Jean-Benoit de Vanssay, Arthur D. Eigenbrot, Andrew Ferayorni, Christopher Foster, Chriselle Ann Galapon, Christopher Gedrites, Kerry Gonzales, Bret D. Goodrich, Brian S. Gregory, Stephanie S. Guzman, Stephen Guzzo, Steve Hegwer, Robert P. Hubbard, John R. Hubbard, Erik M. Johansson, Luke C. Johnson, Chen Liang, Mary Liang, Isaac McQuillen, Christopher Mayer, Karl Newman, Brialyn Onodera, LeEllen Phelps, Myles M. Puentes, Christopher Richards, Lukas M. Rimmele, Predrag Sekulic, Stephan R. Shimko, Brett E. Simison, Brett Smith, Erik Starman, Stacey R. Sueoka, Richard T. Summers, Aimee Szabo, Louis Szabo, Stephen B. Wampler, Timothy R. Williams, and Charles White. The Daniel K. Inouye Solar Telescope -

Observatory Overview. *Solar Phys.*, 295(12):172, December 2020. doi: 10.1007/s11207-020-01736-7.

B. Roberts. Spicules: The resonant response to granular buffeting? *Solar Phys.*, 61(1):23–34, February 1979. doi: 10.1007/BF00155443.

B. Roberts. Wave Propagation in a Magnetically Structured Atmosphere - Part Two - Waves in a Magnetic Slab. *Solar Phys.*, 69(1):39–56, January 1981. doi: 10.1007/BF00151254.

B. Roberts. Waves in Magnetic Flux Tubes. In E. R. Priest and V. Krishan, editors, Basic Plasma Processes on the Sun, volume 142, page 159, January 1990.

Walter Orr Roberts. A Preliminary Report on Chromospheric Spicules of Extremely Short Lifetime. *Astrophys. J.*, 101:136, March 1945. doi: 10.1086/144699.

C. S. Rosenthal, T. J. Bogdan, M. Carlsson, S. B. F. Dorch, V. Hansteen, S. W. McIntosh, A. McMurry, Å. Nordlund, and R. F. Stein. Waves in the Magnetized Solar Atmosphere. I. Basic Processes and Internetwork Oscillations. *Astrophys. J.*, 564(1):508–524, January 2002. doi: 10.1086/324214.

L. Rouppe van der Voort and J. de la Cruz Rodríguez. Short Dynamic Fibrils in Sunspot Chromospheres. *Astrophys. J.*, 776(1):56, October 2013. doi: 10.1088/0004-637X/776/1/56.

L. Rouppe van der Voort, J. Leenaarts, B. De Pontieu, M. Carlsson, and G. Vissers. On-disk Counterparts of Type II Spicules in the Ca II 854.2 nm and Hα Lines. *Astrophys. J.*, 705(1):272–284, November 2009. doi: 10.1088/0004-637X/705/1/272.

L. Rouppe van der Voort, B. De Pontieu, T. M. D. Pereira, M. Carlsson, and V. Hansteen. Heating Signatures in the Disk Counterparts of Solar Spicules in Interface Region Imaging Spectrograph Observations. *Astrophys. J. Lett.*, 799(1):L3, January 2015. doi: 10.1088/2041-8205/799/1/L3.

L. H. M. Rouppe van der Voort, B. De Pontieu, V. H. Hansteen, M. Carlsson, and M. van Noort. Magnetoacoustic Shocks as a Driver of Quiet-Sun Mottles. *Astrophys. J. Lett.*, 660(2):L169–L172, May 2007. doi: 10.1086/518246.

M. S. Ruderman, M. Goossens, and J. Andries. Nonlinear propagating kink waves in thin magnetic tubes. Physics of Plasmas, 17(8):082108, August 2010. doi: 10.1063/1.3464464.

J. H. Rush and W. O. Roberts. Recent Studies of Chromospheric Spicules. Australian Journal of Physics, 7:230, June 1954. doi: 10.1071/PH540230.

R. J. Rutten. Hα as a Chromospheric Diagnostic. In S. A. Matthews, J. M. Davis, and L. K. Harra, editors, First Results From Hinode, volume 397 of Astronomical Society of the Pacific Conference Series, page 54, September 2008.

R. J. Rutten. Solar H-alpha features with hot onsets. III. Long fibrils in Lyman-alpha and with ALMA. *Astron. Astrophys.*, 598:A89, February 2017. doi: 10.1051/0004-6361/201629238.

Robert J. Rutten, Luc H. M. Rouppe van der Voort, and Bart De Pontieu. Solar Hα features with hot onsets. IV. Network fibrils. *Astron. Astrophys.*, 632:A96, December 2019. doi: 10.1051/0004-6361/201936113.

M. Ryutova, T. Berger, Z. Frank, T. Tarbell, and A. Title. Observation of Plasma Instabilities in Quiescent Prominences. *Solar Phys.*, 267(1):75–94, November 2010. doi: 10.1007/s11207-010-9638-9.

Takashi Sakurai. Heating mechanisms of the solar corona. Proceeding of the Japan Academy, Series B, 93:87–97, February 2017. doi: 10.2183/pjab.93.006.

Tanmoy Samanta, Vaibhav Pant, and Dipankar Banerjee. Propagating Disturbances in the Solar Corona and Spicular Connection. *Astrophys. J. Lett.*, 815(1):L16, December 2015. doi: 10.1088/2041-8205/815/1/L16.

Tanmoy Samanta, Hui Tian, Vasyl Yurchyshyn, Hardi Peter, Wenda Cao, Alphonse Sterling, Robertus Erdélyi, Kwangsu Ahn, Song Feng, Dominik Utz, Dipankar Banerjee, and Yajie Chen. Generation of solar spicules and subsequent atmospheric heating. Science, 366(6467):890–894, November 2019. doi: 10.1126/science.aaw2796.

J. C. Santos and J. Büchner. MHD simulation of electric currents in the solar atmosphere caused by photospheric plasma motion. Astrophysics and Space Sciences Transactions, 3(1):29–33, December 2007. doi: 10.5194/astra-3-29-2007.

Goran B. Scharmer, Klas Bjelksjo, Tapio K. Korhonen, Bo Lindberg, and Bertil Petterson. The 1-meter Swedish solar telescope, volume 4853 of Society of Photo-Optical Instrumentation Engineers (SPIE) Conference Series, pages 341–350. 2003a. doi: 10.1117/12.460377.

Goran B. Scharmer, Peter M. Dettori, Mats G. Lofdahl, and Mark Shand. Adaptive optics system for the new Swedish solar telescope, volume 4853 of Society of Photo-Optical Instrumentation Engineers (SPIE) Conference Series, pages 370–380. 2003b. doi: 10.1117/12.460387.

P. H. Scherrer and D. O. Gough. A Critical Evaluation of Recent Claims Concerning Solar Rotation. *Astrophys. J.*, 877(1):42, May 2019. doi: 10.3847/1538-4357/ab13ad.

Hannah Schunker, Jesper Schou, Patrick Gaulme, and Laurent Gizon. Fragile Detection of Solar g-Modes by Fossat et al. *Solar Phys.*, 293(6):95, June 2018. doi: 10.1007/s11207-018-1313-6.

E. Scullion, R. Erdélyi, V. Fedun, and J. G. Doyle. The Response of A Three-dimensional Solar Atmosphere to Wave-driven Jets. *Astrophys. J.*, 743:14, December 2011. doi: 10.1088/0004-637X/743/1/14.

Angelo. Secchi. volume 2 (Paris:Gauthier-Villas). 1877.

D. H. Sekse, L. Rouppe van der Voort, and B. De Pontieu. On the Temporal Evolution of the Disk Counterpart of Type II Spicules in the Quiet Sun. *Astrophys. J.*, 764(2):164, February 2013a. doi: 10.1088/0004-637X/764/2/164.

D. H. Sekse, L. Rouppe van der Voort, B. De Pontieu, and E. Scullion. Interplay of Three Kinds of Motion in the Disk Counterpart of Type II Spicules: Upflow, Transversal, and Torsional Motions. *Astrophys. J.*, 769(1):44, May 2013b. doi: 10.1088/0004-637X/769/1/44.

R. Sharma, G. Verth, and R. Erdélyi. Dynamic Behavior of Spicules Inferred from Perpendicular Velocity Components. ApJ, 840:96, May 2017. doi: 10.3847/1538-4357/aa6d57.

Rahul Sharma, Gary Verth, and Robertus Erdélyi. Evolution of Complex 3D Motions in Spicules. *Astrophys. J.*, 853(1):61, January 2018. doi: 10.3847/1538-4357/aaa07f.

J. Shetye, J. G. Doyle, E. Scullion, C. J. Nelson, D. Kuridze, V. Henriques, F. Woeger, and T. Ray. High-cadence observations of spicular-type events on the Sun. *Astron. Astrophys.*, 589:A3, May 2016. doi: 10.1051/0004-6361/201527505.

K. Shibata and Y. Suematsu. Why are spicules absent over plages and long under coronal holes? *Solar Phys.*, 78(2):333–345, June 1982. doi: 10.1007/BF00151612.

K. Shibata and Y. Uchida. A magnetodynamic mechanism for the formation of astrophysical jets. I - Dynamical effects of the relaxation of nonlinear magnetic twists. *Pub. Astron. Soc. Japan*, 37(1):31–46, January 1985.

K. Shibata and Y. Uchida. Sweeping Magnetic Twist Mechanism for the Acceleration of Jets in the Solar Atmosphere. *Solar Phys.*, 103(2):299–310, February 1986. doi: 10.1007/BF00147831.

K. Shibata, T. Nishikawa, R. Kitai, and Y. Suematsu. Numerical Hydrodynamics of the Jet Phenomena in the Solar Atmosphere - Part Two - Surges. *Solar Phys.*, 77(1-2):121–151, April 1982. doi: 10.1007/BF00156100.

Kazunari Shibata, Yoshinori Ishido, Loren W. Acton, Keith T. Strong, Tadashi Hirayama, Yutaka Uchida, Alan H. McAllister, Ryoji Matsumoto, Saku Tsuneta, Toshifumi Shimizu, Hirohisa Hara, Takashi Sakurai, Kiyoshi Ichimoto, Yohei Nishino, and Yoshiaki Ogawara. Observations of X-Ray Jets with the YOHKOH Soft X-Ray Telescope. *Pub. Astron. Soc. Japan*, 44: L173–L179, October 1992.

Balveer Singh, Kushagra Sharma, and Abhishek K. Srivastava. On modelling the kinematics and evolutionary properties of pressure-pulse-driven impulsive solar jets. Annales Geophysicae, 37(5):891–902, September 2019. doi: 10.5194/angeo-37-891-2019.

K. A. P. Singh, H. Isobe, N. Nishizuka, K. Nishida, and K. Shibata. Multiple Plasma Ejections and Intermittent Nature of Magnetic Reconnection in Solar Chromospheric Anemone Jets. *Astrophys. J.*, 759(1):33, November 2012. doi: 10.1088/0004-637X/759/1/33.

H. Skogsrud, L. Rouppe van der Voort, B. De Pontieu, and T. M. D. Pereira. On the Temporal Evolution of Spicules Observed with IRIS, SDO, and Hinode. *Astrophys. J.*, 806(2):170, June 2015. doi: 10.1088/0004-637X/806/2/170.

V. Smirnova, P. M. Konkol, A. A. Solov'ev, and K. Murawski. Numerical Simulations of Solar Spicule Jets at a Magnetic Null-Point. *Solar Phys.*, 291 (11):3207–3216, November 2016. doi: 10.1007/s11207-016-0976-0.

R. Soler, R. Oliver, and J. L. Ballester. Nonadiabatic Magnetohydrodynamic Waves in a Cylindrical Prominence Thread with Mass Flow. *Astrophys. J.*, 684(1):725–735, September 2008. doi: 10.1086/590244.

Abhishek Kumar Srivastava, Juie Shetye, Krzysztof Murawski, John Gerard Doyle, Marco Stangalini, Eamon Scullion, Tom Ray, Dariusz Patryk Wójcik, and Bhola N. Dwivedi. High-frequency torsional Alfvén waves as an energy source for coronal heating. Scientific Reports, 7:43147, March 2017. doi: 10.1038/srep43147.

Abhishek Kumar Srivastava, Krzysztof Murawski, BlaŻej Kuźma, Dariusz Patryk Wójcik, Teimuraz V. Zaqarashvili, Marco Stangalini, Zdzislaw E. Musielak, John Gerard Doyle, Pradeep Kayshap, and Bhola N. Dwivedi. Confined pseudo-shocks as an energy source for the active solar corona. Nature Astronomy, 2:951–956, October 2018. doi: 10.1038/s41550-018-0590-1.

A. C. Sterling. Solar Spicules: A Review of Recent Models and Targets for Future Observations - (Invited Review). *Solar Phys.*, 196:79–111, September 2000. doi: 10.1023/A:1005213923962.

Alphonse C. Sterling and Joseph V. Hollweg. The Rebound Shock Model for Solar Spicules: Dynamics at Long Times. *Astrophys. J.*, 327:950, April 1988. doi: 10.1086/166252.

Alphonse C. Sterling and John T. Mariska. Numerical Simulations of the Rebound Shock Model for Solar Spicules. *Astrophys. J.*, 349:647, February 1990. doi: 10.1086/168352.

Alphonse C. Sterling, Louise K. Harra, and Ronald L. Moore. Fibrillar Chromospheric Spicule-like Counterparts to an Extreme-ultraviolet and Soft X-ray Blowout Coronal Jet. *Astrophys. J.*, 722(2):1644–1653, October 2010a. doi: 10.1088/0004-637X/722/2/1644.

Alphonse C. Sterling, Ronald L. Moore, and Craig E. DeForest. Hinode Solar Optical Telescope Observations of the Source Regions and Evolution of "Type II" Spicules at the Solar Polar Limb. *Astrophys. J. Lett.*, 714(1): L1–L6, May 2010b. doi: 10.1088/2041-8205/714/1/L1.

Alphonse C. Sterling, Ronald L. Moore, Tanmoy Samanta, and Vasyl Yurchyshyn. Possible Production of Solar Spicules by Microfilament Eruptions. *Astrophys. J. Lett.*, 893(2):L45, April 2020. doi: 10.3847/2041-8213/ab86a5.

Keith T. Strong, Karen Harvey, Tadashi Hirayama, Nariaki Nitta, Toshifumi Shimizu, and Saku Tsuneta. Observations of the Variability of Coronal Bright Points by the Soft X-Ray Telescope on YOHKOH. *Pub. Astron. Soc. Japan*, 44:L161–L166, October 1992.

D. Orozco Suárez, A. Asensio Ramos, and J. Trujillo Bueno. HEIGHT VARIATION OF THE VECTOR MAGNETIC FIELD IN SOLAR SPICULES. The Astrophysical Journal, 803(2):L18, apr 2015. doi: 10.1088/2041-8205/803/2/l18.

Y. Suematsu, K. Shibata, T. Neshikawa, and R. Kitai. Numerical Hydrodynamics of the Jet Phenomena in the Solar Atmosphere - Part One - Spicules. *Solar Phys.*, 75(1-2):99–118, January 1982. doi: 10.1007/BF00153464.

Y. Suematsu, S. Tsuneta, K. Ichimoto, T. Shimizu, M. Otsubo, Y. Katsukawa, M. Nakagiri, M. Noguchi, T. Tamura, Y. Kato, H. Hara, M. Kubo, I. Mikami, H. Saito, T. Matsushita, N. Kawaguchi, T. Nakaoji, K. Nagae, S. Shimada, N. Takeyama, and T. Yamamuro. The Solar Optical Telescope of Solar-B (Hinode): The Optical Telescope Assembly. *Solar Phys.*, 249(2):197–220, June 2008. doi: 10.1007/s11207-008-9129-4.

Yoshinori Suematsu. Influence of Photospheric 5-Minute Oscillations on the Formation of Chro volume 367, page 211. 1990. doi: 10.1007/3-540-53091-6_83.

Yoshinori Suematsu, Haimin Wang, and Harold Zirin. High-Resolution Observation of Disk Spicules. I. Evolution and Kinematics of Spicules in the Enhanced Network. *Astrophys. J.*, 450:411, September 1995. doi: 10.1086/176151.

T. D. Tarbell, M. Bruner, B. Jurcevich, J. Lemen, K. Strong, A. Title, and J. Wolfson. The transition region and coronal explorer (TRACE). In J. J. Hunt, editor, Solar Dynamic Phenomena and Solar Wind Consequences, the Third SOHO Workshop, volume 373 of ESA Special Publication, page 375, December 1994.

E. Tavabi. Hough Transform to Study the Magnetic Confinement of Solar Spicules. Journal of Modern Physics, 3(11):1786–1791, January 2012. doi: 10.4236/jmp.2012.311223.

E. Tavabi, S. Koutchmy, A. Ajabshirizadeh, A. R. Ahangarzadeh Maralani, and S. Zeighami. Alfvénic waves in polar spicules. *Astron. Astrophys.*, 573: A4, January 2015. doi: 10.1051/0004-6361/201423385.

M. Terra-Homem, R. Erdélyi, and I. Ballai. Linear and non-linear MHD wave propagation in steady-state magnetic cylinders. *Solar Phys.*, 217(2):199–223, November 2003. doi: 10.1023/B:SOLA.0000006901.22169.59.

Richard N Thomas and R Grant Athay. Physics of the Solar Chromosphere, volume 29. 1961. doi: 10.1119/1.1937605. URL https://doi.org/10.1119/1.1937605.

H. Tian, E. E. DeLuca, S. R. Cranmer, B. De Pontieu, H. Peter, J. Martínez-Sykora, L. Golub, S. McKillop, K. K. Reeves, M. P. Miralles, P. McCauley, S. Saar, P. Testa, M. Weber, N. Murphy, J. Lemen, A. Title, P. Boerner, N. Hurlburt, T. D. Tarbell, J. P. Wuelser, L. Kleint, C. Kankelborg, S. Jaeggli, M. Carlsson, V. Hansteen, and S. W. McIntosh. Prevalence of small-scale jets from the networks of the solar transition region and chromosphere. Science, 346(6207):1255711, October 2014. doi: 10.1126/science.1255711.

Ajay K. Tiwari, Richard J. Morton, Stéphane Régnier, and James A. McLaughlin. Damping of Propagating Kink Waves in the Solar Corona. *Astrophys. J.*, 876(2):106, May 2019. doi: 10.3847/1538-4357/ab164b.

Kenji Toma, Serguei S. Komissarov, and Oliver Porth. Rayleigh-Taylor instability in two-component relativistic jets. *Mon. Not. Roy. Astron. Soc.*, 472 (1):1253–1258, November 2017. doi: 10.1093/mnras/stx1770.

S. Tomczyk, S. W. McIntosh, S. L. Keil, P. G. Judge, T. Schad, D. H. Seeley, and J. Edmondson. Alfvén Waves in the Solar Corona. Science, 317(5842): 1192, August 2007. doi: 10.1126/science.1143304.

Steven Tomczyk and Scott W. McIntosh. Time-Distance Seismology of the Solar Corona with CoMP. *Astrophys. J.*, 697(2):1384–1391, June 2009. doi: 10.1088/0004-637X/697/2/1384.

Christopher Torrence and Gilbert P. Compo. A Practical Guide to Wavelet Analysis. Bulletin of the American Meteorological Society, 79(1):61–78, January 1998. doi: 10.1175/1520-0477(1998)079⟨0061:APGTWA⟩2.0.CO;2.

G. Tóth. A General Code for Modeling MHD Flows on Parallel Computers: Versatile Advection Code. Astrophysical Letters and Communications, 34: 245, January 1996.

G. Tsiropoula, C. E. Alissandrakis, and B. Schmieder. The fine structure of a chromospheric rosette. *Astron. Astrophys.*, 271:574, April 1993.

G. Tsiropoula, K. Tziotziou, I. Kontogiannis, M. S. Madjarska, J. G. Doyle, and Y. Suematsu. Solar Fine-Scale Structures. I. Spicules and Other Small-Scale, Jet-Like Events at the Chromospheric Level: Observations and Physical Parameters. *Space Sci. Rev.*, 169:181–244, September 2012. doi: 10.1007/s11214-012-9920-2.

S. Tsuneta, K. Ichimoto, Y. Katsukawa, S. Nagata, M. Otsubo, T. Shimizu, Y. Suematsu, M. Nakagiri, M. Noguchi, T. Tarbell, A. Title, R. Shine, W. Rosenberg, C. Hoffmann, B. Jurcevich, G. Kushner, M. Levay, B. Lites, D. Elmore, T. Matsushita, N. Kawaguchi, H. Saito, I. Mikami, L. D. Hill, and J. K. Owens. The Solar Optical Telescope for the Hinode Mission: An Overview. *Solar Phys.*, 249(2):167–196, June 2008. doi: 10.1007/s11207-008-9174-z.

Yutaka Uchida and Osamu Kaburaki. Excess Heating of Corona and Chromosphere Above Magnetic Regions by Non-Linear Alfvén Waves. *Solar Phys.*, 35(2):451–466, April 1974. doi: 10.1007/BF00151968.

Tom Van Doorsselaere, Patrick Antolin, Ding Yuan, Veronika Reznikova, and Norbert Magyar. Forward modelling of optically thin coronal plasma with the FoMo tool. Frontiers in Astronomy and Space Sciences, 3:4, February 2016. doi: 10.3389/fspas.2016.00004.

Tom Van Doorsselaere, Abhishek K. Srivastava, Patrick Antolin, Norbert Magyar, Soheil Vasheghani Farahani, Hui Tian, Dmitrii Kolotkov, Leon Ofman, Mingzhe Guo, Iñigo Arregui, Ineke De Moortel, and David Pascoe. Coronal Heating by MHD Waves. *Space Sci. Rev.*, 216(8):140, December 2020. doi: 10.1007/s11214-020-00770-y.

Michiel van Noort, Luc Rouppe van der Voort, and Mats G. Löfdahl. Solar Image Restoration By Use Of Multi-frame Blind De-convolution With Multiple Objects And Phase Diversity. *Solar Phys.*, 228(1-2):191–215, May 2005. doi: 10.1007/s11207-005-5782-z.

Maurice H. P. M. van Putten. Knots in Simulations of Magnetized Relativistic Jets. *Astrophys. J. Lett.*, 467:L57, August 1996. doi: 10.1086/310196.

Miroslav Čada and Manuel Torrilhon. Compact third-order limiter functions for finite volume methods. Journal of Computational Physics, 228(11):4118–4145, June 2009. doi: 10.1016/j.jcp.2009.02.020.

J. E. Vernazza, E. H. Avrett, and R. Loeser. Structure of the solar chromosphere. III - Models of the EUV brightness components of the quiet-sun. *Astrophys. J. Suppl.*, 45:635–725, April 1981. doi: 10.1086/190731.

G. Verth and D. B. Jess. MHD Wave Modes Resolved in Fine-Scale Chromospheric Magnetic Structures. Washington DC American Geophysical Union Geophysical Monograph Series, 216:431–448, February 2016. doi: 10.1002/9781119055006.ch25.

E. Verwichte, V. M. Nakariakov, L. Ofman, and E. E. Deluca. Characteristics of transverse oscillations in a coronal loop arcade. *Solar Phys.*, 223(1-2): 77–94, September 2004. doi: 10.1007/s11207-004-0807-6.

E. Verwichte, T. Van Doorsselaere, R. S. White, and P. Antolin. Statistical seismology of transverse waves in the solar corona. *Astron. Astrophys.*, 552: A138, April 2013. doi: 10.1051/0004-6361/201220456.

O. von der Luehe. Speckle imaging of solar small scale structure. I - Methods. *Astron. Astrophys.*, 268(1):374–390, February 1993.

M. von Uexkuell, F. Kneer, W. Mattig, A. Nesis, and W. Schmidt. Oscillations of the sun's chromosphere. III - Simultaneous H-alpha observations from two sites. *Astron. Astrophys.*, 146(1):192–194, May 1985.

J. Vranjes, S. Poedts, B. P. Pandey, and B. de Pontieu. Energy flux of Alfvén waves in weakly ionized plasma. *Astron. Astrophys.*, 478(2):553–558, February 2008. doi: 10.1051/0004-6361:20078274.

Haimin Wang. Comparison of Hα and He II λ304 Macrospicules. *Astrophys. J.*, 509(1):461–470, December 1998. doi: 10.1086/306497.

Yikang Wang and Takaaki Yokoyama. Simulation of Alfvén Wave Propagation in the Magnetic Chromosphere with Radiative Loss: Effects of Nonlinear Mode Coupling on Chromospheric Heating. *Astrophys. J.*, 891(2):110, March 2020. doi: 10.3847/1538-4357/ab70b2.

S. Wedemeyer-Böhm, A. Lagg, and Å. Nordlund. Coupling from the Photosphere to the Chromosphere and the Corona. *Space Sci. Rev.*, 144(1-4): 317–350, April 2009. doi: 10.1007/s11214-008-9447-8.

D. G. Wentzel. Coronal Heating by Alfvén Waves. *Solar Phys.*, 39(1):129–140, November 1974. doi: 10.1007/BF00154975.

G. L. Withbroe. The role of spicules in heating the solar atmosphere Implications of EUV observations. *Astrophys. J.*, 267:825–836, April 1983. doi: 10.1086/160917.

G. L. Withbroe and R. W. Noyes. Mass and energy flow in the solar chromosphere and corona. *Annual Review of Astron and Astrophys.*, 15:363–387, January 1977. doi: 10.1146/annurev.aa.15.090177.002051.

G. L. Withbroe, D. T. Jaffe, P. V. Foukal, M. C. E. Huber, R. W. Noyes, E. M. Reeves, E. J. Schmahl, J. G. Timothy, and J. E. Vernazza. Extreme-ultraviolet transients observed at the solar pole. *Astrophys. J.*, 203:528–532, January 1976. doi: 10.1086/154108.

C. Xia, J. Teunissen, I. El Mellah, E. Chane, and R. Keppens. MPI-AMRVAC 2.0 for Solar and Astrophysical Applications. ArXiv e-prints, October 2017.

Y. Yamauchi, H. Wang, Y. Jiang, N. Schwadron, and R. L. Moore. Study of Hα Macrospicules in Coronal Holes: Magnetic Structure and Evolution in Relation to Photospheric Magnetic Setting. *Astrophys. J.*, 629(1):572–581, August 2005. doi: 10.1086/431664.

Takaaki Yokoyama and Kazunari Shibata. Magnetic reconnection as the origin of X-ray jets and Hα surges on the Sun. *Nature*, 375(6526):42–44, May 1995. doi: 10.1038/375042a0.

Takaaki Yokoyama and Kazunari Shibata. Numerical Simulation of Solar Coronal X-Ray Jets Based on the Magnetic Reconnection Model. *Pub. Astron. Soc. Japan*, 48:353–376, April 1996. doi: 10.1093/pasj/48.2.353.

Peter R. Young. Dark Jets in Solar Coronal Holes. *Astrophys. J.*, 801(2):124, March 2015. doi: 10.1088/0004-637X/801/2/124.

Ding Yuan, Jiangtao Su, Fangran Jiao, and Robert W. Walsh. Stochastic Transients as a Source of Quasi-periodic Processes in the Solar Atmosphere. The Astrophysical Journal Supplement Series, 224:30, June 2016. doi: 10.3847/0067-0049/224/2/30.

Vasyl Yurchyshyn, Wenda Cao, Valentina Abramenko, Xu Yang, and Kyung-Suk Cho. Rapid Evolution of Type II Spicules Observed in Goode Solar Telescope On-disk H_α Images. *Astrophys. J. Lett.*, 891(1):L21, March 2020. doi: 10.3847/2041-8213/ab7931.

T. V. Zaqarashvili and R. Erdélyi. Oscillations and Waves in Solar Spicules. *Space Sci. Rev.*, 149:355–388, December 2009. doi: 10.1007/s11214-009-9549-y.

T. V. Zaqarashvili, E. Khutsishvili, V. Kukhianidze, and G. Ramishvili. Doppler-shift oscillations in solar spicules. *Astron. Astrophys.*, 474(2):627–632, November 2007. doi: 10.1051/0004-6361:20077661.

Teimuraz V. Zaqarashvili. Dynamic Kink Instability and Transverse Motions of Solar Spicules. *Astrophys. J. Lett.*, 893(2):L46, April 2020. doi: 10.3847/2041-8213/ab881d.

Xiang Zhai and Paul M. Bellan. A hybrid Rayleigh-Taylor-current-driven coupled instability in a magnetohydrodynamically collimated cylindrical plasma with lateral gravity. Physics of Plasmas, 23(3):032121, March 2016. doi: 10.1063/1.4943896.

Q. M. Zhang and H. S. Ji. Blobs in recurring extreme-ultraviolet jets. *Astron. Astrophys.*, 567:A11, July 2014. doi: 10.1051/0004-6361/201423698.

Q. M. Zhang, H. S. Ji, and Y. N. Su. Observations of Multiple Blobs in Homologous Solar Coronal Jets in Closed Loop. *Solar Phys.*, 291(3):859–876, March 2016. doi: 10.1007/s11207-016-0878-1.

Y. Z. Zhang, K. Shibata, J. X. Wang, X. J. Mao, T. Matsumoto, Y. Liu, and J. T. Su. Revision of Solar Spicule Classification. *Astrophys. J.*, 750(1):16, May 2012. doi: 10.1088/0004-637X/750/1/16.

U. Ziegler and P. Ulmschneider. Dynamical response of magnetic tubes to transverse perturbations. II. Towards thin flux tubes. A&A, 327:854–862, November 1997a.

U. Ziegler and P. Ulmschneider. Dynamical response of magnetic tubes to transverse perturbations. I. Thick flux tubes. *Astron. Astrophys.*, 324:417–431, August 1997b.

J. B. Zirker. Coronal Heating. *Solar Phys.*, 148(1):43–60, November 1993. doi: 10.1007/BF00675534.

Noémi Kinga Zsámberger and Róbert Erdélyi. Magnetoacoustic Waves in a Magnetic Slab Embedded in an Asymmetric Magnetic Environment. III. Applications to the Solar Atmosphere. *Astrophys. J.*, 906(2):122, January 2021. doi: 10.3847/1538-4357/abca9d.

Z. H. Zuo, Y. Li, J. H. Sha, and T. H. Zhou. A Solar Jet Triggered by a Decaying Satellite Sunspot. Acta Astronomica Sinica, 60(6):56, November 2019.